Growth and Investigation of Group II-VI Semiconductor Nanoparticles for Luminescence Based Applications

Thesis

Submitted to

Delhi Technological University

in partial fulfilment for the requirements for the degree of

DOCTOR OF PHILOSOPHY

in

APPLIED PHYSICS

By

Vineet Sharma

(Reg. No. 2K18/PHDAP/13)

Under the Supervision of

Dr. Mohan Singh Mehata

DEPARTMENT OF APPLIED PHYSICS

DELHI TECHNOLOGICAL UNIVERSITY

DELHI-110 042, INDIA

OCTOBER-2021

Dedicated to…

My beloved parents…

DECLARATION

I hereby declare that the work presented in this thesis entitled ***"Growth and investigation of group II-VI semiconductor nanoparticles for luminescence based applications"*** submitted to the Delhi Technological University (DTU), Delhi for the award of degree of ***"Doctor of Philosophy"*** is based on the original research work carried out by me under the supervision of Dr. Mohan Singh Mehata, Assistant Professor, Department of Applied Physics, Delhi Technological University, Delhi and has fulfilled the requirements for the submission of this thesis. I further declare that it has not formed the basis for the award of any degree, diploma, fellowship or associateship or similar title of any University/Institution. The extent of information derived from the existing literature has been indicated in the body of the thesis at appropriate places giving the references.

Vineet Sharma
Research Scholar
(Reg. No. 2K18/PHDAP/13)

Date: **14/12/2021**
Place: **Delhi**

Delhi Technological University
Formerly Delhi College of Engineering
(Under Delhi Act 6 of 2009, Govt. of NCT of Delhi)
Shahbad Daulatpur, Bawana Road, Delhi-110042

CERTIFICATE

This is to certify that the thesis entitled ***"Growth and investigation of group II-VI semiconductor nanoparticles for luminescence based applications"*** submitted to the Delhi Technological University (DTU), Delhi for the award of degree of "***Doctor of Philosophy***" in Applied Physics is a record of bonafide original research work carried out by ***Mr. Vineet Sharma*** under my supervision at Laser-Spectroscopy Laboratory, Department of Applied Physics, Delhi Technological University, Delhi and has fulfilled the requirements for the submission of this thesis. It is further certified that the work embodied in this thesis has neither been partially nor fully submitted to any other university or institution for the award of any degree or diploma.

Dr. Mohan Singh Mehata
Supervisor
Assistant Professor
Department of Applied Physics
Delhi Technological University,
Delhi- 110 042

Submitted Through:

Prof. Rinku Sharma
Head
Department of Applied Physics
Delhi Technological University,
Delhi-110042

ACKNOWLEDGEMENTS

The journey of my research is accomplished with the valuable support of many people. It is a pleasant aspect that I have now the opportunity to express my gratitude for all of them.

At the outset, I would like to my profound sense of gratitude, indebtedness and reverence to my supervisor, ***Dr. Mohan Singh Mehata****, Department of Applied Physics, Delhi Technological University, Delhi, who nurtured my research capabilities for a successful scientific research career. It has been an honor to work under excellent, enthusiastic and distinguished supervisors. Their unremitting encouragement, constant help, meticulous supervision and constructive criticism throughout the course of my study for carving another milestone in my academic journey.*

I feel privileged to have worked under such a great supervision. I further stand orated to ***Prof. Rinku Sharma****, Head, Department of Applied Physics, DTU, for her valuable help and suggestions. My heartfelt recognitions for* ***Prof. S. C. Sharma****, DRC Chairman, former Head, Department of Applied Physics, DTU, my SRC & DRC committee members* ***Prof. Ravi Kant Soni, IIT Delhi, Dr. Bipin Gupta, NPL, Delhi*** *for their enduring support and appropriate propositions. I express my sincere gratitude especially to* ***Dr. Yogita Kalra,*** *Assistant Professor, Department of Applied Physics, DTU, and* ***Dr. Anil Haritash,*** *Associate Professor, Department of Environmental Engineering, DTU for their timely advice and support as SRC members.*

It is my pleasure to express my sincere thanks to all the faculty members of Department of Applied Physics, DTU for their continuous encouragement and help during my research work. I am also grateful technical and non-technical staff for their timely support and cooperation whenever required.

I sincerely thank my dear former and present lab-mates whose support helped in accomplishing my work. It is my pleasure to thank my seniors ***Dr. Ratneshwar Kr. Ratnesh****, D****r. Mrityunjay Kumar Singh, Mr. Vijay Singh Meena, Dr. Prateek Sharma*** *and the present lab-mates* ***Ms. Aneesha, Mr. Deepak Kumar, Mr. Aryan, Ms. Namrata Sharma*** *for their support and timely help. I would like to thank my friends* ***Rashi Mann, Meenu Chahar, Parnika Arora, Asifa, Anuj Sharma*** *and* ***Anurag Sharma*** *for their timely help, encouragement and unwavering support during my difficult time. Their friendship has provided a wonderful time along the way. I would also like to thank all the other research scholars of Department of Applied Physics, Delhi Technological University, Delhi for their help and advice.*

Finally, I thank my family for their support and motivation, every moment of my research period. With heartfelt gratitude and love, I express my gratefulness to my father ***Mr. Vinod Sharma****, mother* ***Mrs. Munni Devi*** *for their continual love and encouragement over the entire course of my life. I am thankful to my brother* ***Gaurav Sharma*** *and sister* ***Preeti Sharma*** *for their constant encouragement, care, love, blessings and have helped me to achieve what I am today. I am thankful to my extended maternal and paternal family for helping me maintain a positive attitude throughout my studies. I always thankful to all my beloved friends across the globe for sharing my happiness and sorrow.*

I gratefully acknowledge the financial assistance provided by ***Science and Engineering Research Board (SERB), Department of Science and Technology (DST), Govt. of India*** *in the form of Junior Research Fellowship during the period of my research. I extend my gratitude to Delhi Technological University and staff in Administration, Accounts, Store & Purchase, Library and Computer Centre for their help and services.*

I express my sincere gratitude to our international research collaborators; ***Prof****.* ***Victor Nadtochenko, Arseniy Aybush*** *and* ***Fedor Gostev,*** *Federal Research Centre of Chemical Physics, Russian Academy of Sciences, Russian Federation for providing Ultrafast transient absorption spectroscopy facility, their help and co-operation.*

I thank one and all for helping me accomplish the successful realization of the thesis.

Thank you all!!!

Vineet Sharma

LIST OF PUBLICATIONS

Publications in the thesis

1. **Vineet Sharma** and Mohan Singh Mehata, Synthesis of photoactivated highly fluorescent Mn^{2+}-doped ZnSe quantum dots as effective lead sensor in drinking water, **Materials Research Bulletin 134 (2021) 111121.**
2. **Vineet Sharma** and Mohan Singh Mehata, Rapid optical sensor for recognition of explosive 2,4,6-TNP traces in water through fluorescent ZnSe quantum dots, **Spectrochimica Acta Part A: Molecular and Biomolecular Spectroscopy 260 (2021) 119937.**
3. **Vineet Sharma** and Mohan Singh Mehata, A parallel investigation of un-doped and Mn^{2+} doped zinc selenide quantum dots at low temperature and application as an optical temperature sensor, ***Materials Chemistry and Physics 276 (2022) 125349.***
4. **Vineet Sharma** and Mohan Singh Mehata, Photoluminescence turn-off based dual analytes (Hg^{2+} and Pb^{2+}) sensor in water using 3-marcaptoproponic acid protected Mn^{2+} doped ZnSe quantum dots, ***Chemical Physics Letters 787 (2022) 139270.***
5. Mohan Singh Mehata, **Vineet Sharma**, Abhinav Tandon, Arseniy Aybush, Fedor Gostev and Victor Nadtochenko, Micro- to Femtosecond Exciton Dynamics of Light-Emitting Metal Incorporated Zinc-Selenide (ZnSe) Quantum Dots for Possible White QLEDs, ***(Communicated for publication).***
6. Mohan Singh Mehata, **Vineet Sharma** and Abhinav Tandon, Light-emitting metal and dual metal-doped zinc selenide quantum dots and method thereof, ***Patent application no. 201911052787A and Publication date: 27/12/2019 (Not included in thesis).***

Publications in conference/workshop proceeding

1. **Vineet Sharma** and Mohan Singh Mehata, “Synthesis of luminescent ZnSe and metal-doped ZnSe quantum dots via aqueous route: An optical property” presented at “International Conference on Recent Advances in Interdisciplinary Sciences” held on 11-12 January 2019, Jammu University, Jammu.
2. **Vineet Sharma** and Mohan Singh Mehata, “Synthesis of green light emitting copper doped ZnSe quantum dots for lighting application” presented at “International Conference on Atomic, molecular, optical and nano physics with applications” held on 18-20, December, 2019, DTU, Delhi.

CONTENTS

LIST OF FIGURES

LIST OF TABLES

Chapter 1

Introduction

The work presented in the thesis focused on zero-dimensional II-VI semiconductor-based luminescent materials, including zinc-based un-doped and transition metals doped/co-doped luminescent nanoparticles. The chapter mainly gives a brief introduction to the nanomaterials and classifications based on the confinement of the system. Also, it introduces 0-D II-VI semiconductor quantum dots, specifically zinc selenide quantum dots (ZnSe QDs) and their properties, as well as focused on important applications of these materials in various sensing areas purposes, like hazardous toxic heavy metals, explosive compounds and temperature sensors.

1.1 Nanomaterials

Physics and chemistry have experienced significant development in the nanometer size range, leading to a new interdisciplinary field of nanoscience in the last decade. The attention in nanoscale materials increases because many physical phenomena occur at a length scale between 1 and 100 nm in both organic and inorganic materials. Nanoparticles are microscopic particles having a dimension below 100 nm at least in one direction. A drastic change in the various properties of materials is observed as nanoscale size is achieved and a significantly high number of loosely bonded atoms present at the material surface. Numerous size-dependent properties are detected in nano regime such as super paramagnetism in magnetic substances, quantum confinement in semiconductor particles and surface plasmon resonance in some metal particles [1].

Typically, nanoparticles have possessed excellent and unpredictable optical properties due to the applicability of quantum effects which arises because of

sufficiently small confinement of their electrons. When one or more than one dimension of a material is reduced to the nanoscale, its physicochemical properties are remarkably changed from the bulk counterpart. With the size reduction, novel optical, magnetic, chemical, mechanical and electrical properties can be introduced. Then, the resulting size-reduced systems are called low-dimensional systems. In the low-dimensional structures, the confinement of particles, i.e., electrons or holes, leads to the manifestation of size effects and dramatic changes in the properties or behaviour of the materials, which generally comes into the quantum-size effects [2]. Nanostructures play the role of bridge between the molecules and bulk materials. Nanostructures can lead to new technologies and devices by suitable control of the properties and responses.

1.2 Classification of low-dimensional materials

There are numerous approaches for the classification of nanomaterials. The nanomaterials and structures are generally categorized based on the reduced dimension or order of confinement of particles in the system, which refers to the degrees of freedom for the momentum of particles [3]. Therefore, considering the dimensionality of the system, the following classification is achieved as represented in Figure 1.1 and discussed below, which shows different low dimensional systems with a density of states versus energy plots.

1.2.1 Three-dimensional (3D) structure:

In 3-D materials, no quantization of the particle motion occurs, i.e., 0-D confinement of particles and the particles are free to move in all three directions. Examples of such materials are bulk structures, dispersion of nanoparticles, etc.

1.2.2 Two-dimensional (2D) structure:

In 2-D nanomaterials, the quantization of the motion of the particles occurs only in one

direction, i.e., 1-D confinement of particles, while the particles can freely move in the other two directions. Example- thin films, quantum wells and superlattices.

1.2.3 One-dimensional (1D) structure:

In 1-D structures, the quantization occurs in two directions, i.e., 2-D confinement of particles, leading to free movement along only one direction; for example- quantum wire, nanowire, nanorods and nanotube. Nanowires electrically conduct extremely long wires in nano dimensions with improved transport properties because of the quantum effects. The conduction charge carriers (electrons) are confined in the transverse direction, which results in quantizing energy into discrete energy levels.

1.2.4 Zero-dimensional (0D) structure:

In 0-D nanomaterials, the quantization occurs in all three spatial directions, i.e., and the particles are restricted in all three directions or 3-D confinement of particles. For example- quantum dots, which are also called artificial atoms.

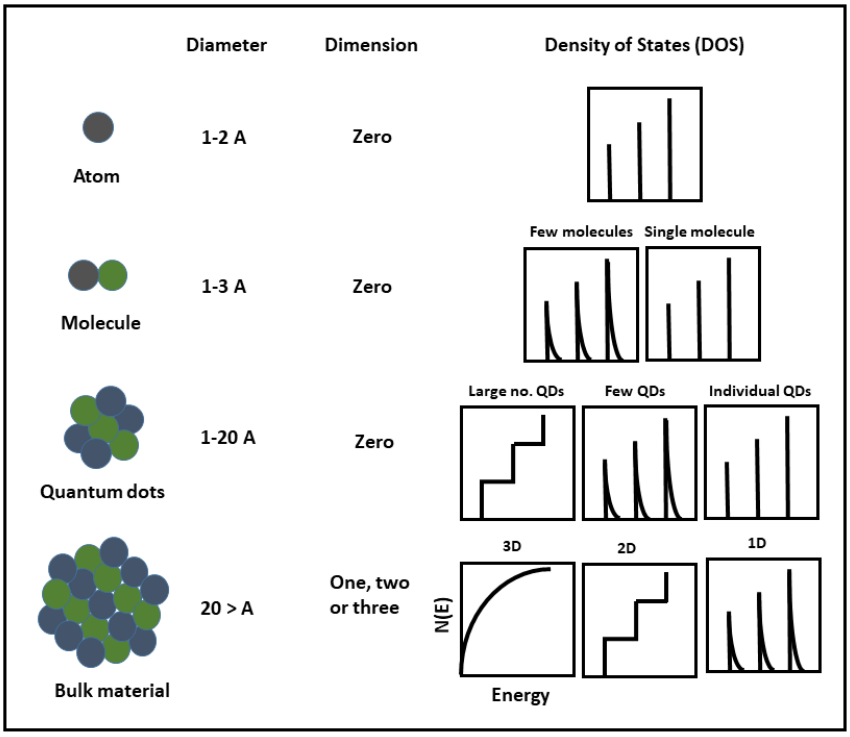

Figure 1.1. The classification of nanomaterials and corresponding density of state N(E) versus energy (E) plots for 0-D to 3-D materials.

1.3. Effects controlling the properties at the nanoscale

1.3.1 Quantum confinement effects

Quantum confinement or size effects arise with the decreasing particles size. The increase in the energy gap between the highest occupied molecular orbital (HOMO) and the lowest unoccupied molecular orbital (LUMO) is observed for nanomaterials as particle size decreases, leading to their implications in photo-physics and electronic structures. The loosely bound electronic excitation (electron-hole pair) through Columbic interactions are present in the semiconductor quantum dots, known as Mott-Wannier exciton [4]. These bound states have energy usually lower than the bandgap energy and dimension much larger than the lattice constant. As the size of quantum dots approaches the exciton Bohr diameter, the change in the optical properties of the material activates with the effects of quantum confinement. The exciton Bohr radius (r_b) is given by equation as follow [5]:

$$r_b = \frac{\hbar^2 \mathcal{E}}{e^2}\left[\frac{1}{m_e} + \frac{1}{m_h}\right]$$

where Ɛ is the dielectric constant, $\hbar$ represents the reduced Plank constant, e denotes the electronic charge, m_e and m_h are the electron and hole effective mass, respectively. When the diameter of semiconductor quantum dots reduces up to the dimension of excitonic Bohr radius, the moment of electrons and holes is confined. The generated excitons must be confined into such a small dimension. Thus, additional energy is required to confine these localized excitons, which raises its excitonic transition energy.

1.3.2 High surface to volume ratio of quantum dots

In nanomaterials, a large number of atoms are presented on the surface compared to the bulk materials. The high surface-to-volume ratio of semiconductor quantum dots has significant effects on their optical and structural properties. Surface atoms mildly influence the optical absorption while the emission efficiency and time evolution are

strongly too affected. These surface atoms result in the form of the presence of surface states between the bandgap, which arises from unsaturated binds, surface non-stoichiometry, etc. The generated surface traps or states induce the nonradiative recombination of charge carriers (electrons and holes), resulting in reduced emission efficiency. Sometimes, these surface states can also have aided the radiative transitions.

1.4. Unique materials properties at the nanoscale

Low dimensional nanomaterials have structural features between bulk materials and individual atoms, as shown in Figure 1.1. The properties of nanomaterials are significantly different from those of bulk materials. This is mainly due to the nanometer size of the materials;

- a large fraction of surface atoms
- spatial confinement
- high surface energy
- reduced imperfections

Nanomaterials have a large surface area to volume ratio due to their small dimension, making a large number of surface or interfacial atoms resulting in more surface-dependent material properties. For example, nanoparticles and nanowires-based chemical sensors show enhanced selectivity and sensitivity; nanoparticles can be used as active catalysts, etc. [6,7]. The charge carrier density and energy band structure can be modified quite differently in the nanomaterials from their bulk counterparts and change the optical properties and electronics. For example, light-emitting diodes (LEDs) and lasers fabricated using quantum wires and quantum dots are promising in the future optoelectronics such as high-density information storage is a fast developing area using quantum dot devices. In determining the properties of the nanomaterials, reduced imperfections play an important role by altering several factors. Nanomaterials

and nanostructures favour the "self-purification" process, due to which the intrinsic material defects and impurities move with thermal annealing near to the surface. This improved material perfection and affects many properties of nanomaterials. For example, carbon nanotubes are well known for their superior mechanical properties. The chemical stability may enhance the mechanical properties of certain nanomaterials, etc. At present, nanomaterials are well known to have countless novel and improved properties compared to bulk materials [8-16].

1.5. Method of Preparation

The preparation of discrete nanoparticles can be done through the "bottom-up approach and top-down approach". Control of size and shape of particles and their re-productivity is a prime factor in the method for the synthesis of phase materials. In addition, chemical control of the phase and the chemical cleanliness of the interfaces must be controlled.

1.5.1 Top-down approach

This method involves starting with a bulk solid and obtaining a nanostructure by structural composition. In this, nano-objects are constructed from larger entities without atomic-level control. The main problem with the top-down approach is the imperfection of surface structure. This method involves physical reactions for the synthesis of nanomaterials. The top-down approach involves the:

- High energy milling.
- Sputtering
- Chemical mechanical milling
- Electro-explosion
- Vapour phase condensation
- Laser ablation

1.5.2 Bottom-up approach

The bottom-up technique should be able to make a lot of small structures simultaneously and should be cheaper than that of the top-down technique, but it may be challenging to design bigger and more complicated structures. This technique plays an important role in the fabrication of nanoparticles and nanomaterials. The material is built up from the bottom, atom by atom, molecule by molecule. This involves irreversible chemical reactions. In the chemical method, there is difficulty controlling the growth of particles and then stripping the newly formed particles from agglomeration.

1.6. Advantages and disadvantages of direct aqueous synthesis over organometallic approach:

There are numerous facile and novel synthesis techniques to prepare the high-quality ZnSe and doped ZnSe QDs. The growth mechanism of Cu:ZnSe nanocrystals in organic solution through organometallic approach as reported by Pradhan *et al.* [17] have developed. The successful synthesis of doped ZnSe nanocrystals is based on the adsorption of dopant impurity on the ZnSe core at the nucleation stage. After the successful incorporation of dopant into the host, the growth of ZnSe at the growth stage was carried out. Thus, the direct aqueous route provides better control over the reaction at each step in this direction.

Here, we discuss some general advantages of the direct aqueous route synthesis with the organometallic synthesis approach of quantum dots. The comparison with the organometallic approach will be based on the literature review and their published properties. Among the various advantages of the aqueous synthesis, firstly should mention its high reproducibility and simplicity. Thus, colloids of quantum dots without the hot-injection technique and the use of toxic TOPO-TOP mixture with a small

particle size distribution can be developed [18-21]. As a result, the effective large-scale production of thiol-capped quantum dots was achieved through aqueous synthesis. However, the scaling up of the organometallic synthesis is difficult due to the use of extremely dangerous reactants and their poor reproducibility [22,23]. Thiol-capped quantum dots prepared by the aqueous synthesis can be precipitated, dried and kept in the powder state under normal laboratory conditions for as long as few years without losing their solubility and stability in an aqueous medium. As a compression based on the luminescence efficiencies and photo-stabilities that have potential importance for large applications of highly luminescent quantum dots, both synthesis routes gave similar results. Thus, the aqueous synthesis is a more favourable and adaptable technique for the synthesis of quantum dots. However, the organometallically prepared quantum dots possess a high degree of crystallinity over the aqueous route synthesized quantum dots because high annealing temperatures (200-360 °C) are used in the organometallic approach during the synthesis. Also, in the organometallic synthesis by the hot-injection method, an effective difference in nucleation and growth stages is attained, which permits achieving the narrower size distributions compared to aqueous synthesis. When the water-soluble quantum dots are desired, e.g., for fluorescent-based sensing and bio-mapping applications, surface charge and other surface properties play an important role. The choice of stabilizing mercapto compound with appropriate free functional groups allows the control of such properties. MPA-capped direct aqueous route synthesized water-soluble ZnSe quantum dots having stable photoluminescence with a quantum yield up to 35% reported in the present study.

1.7. Literature review

1.7.1 Fundamentals of semiconductor quantum dots

Quantum dots have physical dimensions in between the bulk crystalline solids and the

atomic/molecular unit. Over the past decades, semiconductor quantum dots have gained the extreme interest of researchers due to their unique properties and promising applications. Quantum dots as a function of physical dimension exhibit significant variations in electrical, optical and physical properties.

Table 1.1 A comparison of the advantages and disadvantages of quantum dots and organic dyes.

Parameter	Quantum dots	Organic dye	References
Absorption spectra	A wide range of absorption enables free selection of excitation wavelength	Discrete bands with FWHM lies between 35 nm to 100 nm	[24, 25]
Fluorescence spectra	Narrow FWHM (30 – 90 nm) with symmetric Gaussian profile	Asymmetric profile generally towards higher wavelength side	[24, 25]
Stokes shift	Short, typically < 60 nm	High, usually < 60 nm to > 150 nm	[26]
Fluorescence quantum yield	10–80% for visible, 20–70% for NIR	50–100% for visible, 5–25% for NIR	[26, 27]
Fluorescence lifetime	multi-exponential decay with an order of 10-100 ns	Mono-exponential decay with 1–10 ns	[25, 28]
Size	1–60 nm (hydrodynamic diameter)	~ 0.5 nm	[29]
Photochemical stability	High (for all optical range). Can reveal photo-brightening	good for many optical range applications, problematic for high radiation flux applications and NIR wavelengths	[24-25]
Thermal stability	High and can be improved using different ligands	Dependent on dye class, critical for NIR wavelength dye	[29]
Toxicity	Slight toxic but can be prevented using shell formation	From very low to high, dependent on dye	[30]
Solubility and dispersibility	Control through surface chemistry (capping agents or ligands)	Control via substation pattern	[31]
Reproducibility (optical chemical properties)	Low, limited by surface chemistry and complex structure, few commercial systems available	Good, with defined molecular shape and structure, many commercial sources are available	[29]

The fundamental properties are manipulated or changed in an enormous range by size and single chemical composition in the material. Some basic properties or parameters of few II-VI semiconductor quantum dots are summarized in Table 1.1. These size-dependent properties are mainly depending upon two major effects. First, the density of electronic energy levels in semiconductors is known as quantum size or confinement effects. Second, the number of atoms present on the surface verse the atoms present interior of particles is relatively large friction in semiconductors nanomaterials. These two effects also play an essential role in the luminescent properties of semiconductor quantum dots.

1.7.2 ZnSe quantum dots (ZnSe QDs)

Among the several quantum dots, ZnSe is the current trend of safe handling nanotechnology and is to be recognized as an environmentally friendly material. It is a wide bandgap II-VI semiconductor with an energy gap at room temperature of 2.67 eV. The bulk ZnSe has an exciton binding energy of 18 meV with the Bohr exciton radius of 4.5 nm. In comparison with silicon carbide and gallium nitride, ZnSe is considered the leading candidate for the fabrication of laser diodes (LDs) and blue light-emitting diodes (LEDs) in the nano regime. ZnSe QDs can be prepared of different shapes and sizes through a variety of synthesis techniques [32-35].

1.7.3 Structure of Zinc selenide

The formation of different crystal structures of the ZnSe mainly depends on the growth conditions of the quantum dots, such as the molar ratios of the precursors, growth temperature, pH, reaction time and the concentration of precursors. Depending on the growth conditions, the synthesized quantum dots have a cubic zinc blende and wurtzite (hexagonal) structure. In the low-temperature conditions, the formation of the cubic zinc blende structure of ZnSe has high possibilities as the formation of the hexagonal

structure requires the high energy of formation. Also, reaction time plays an important role in slight changes in the crystal structure.

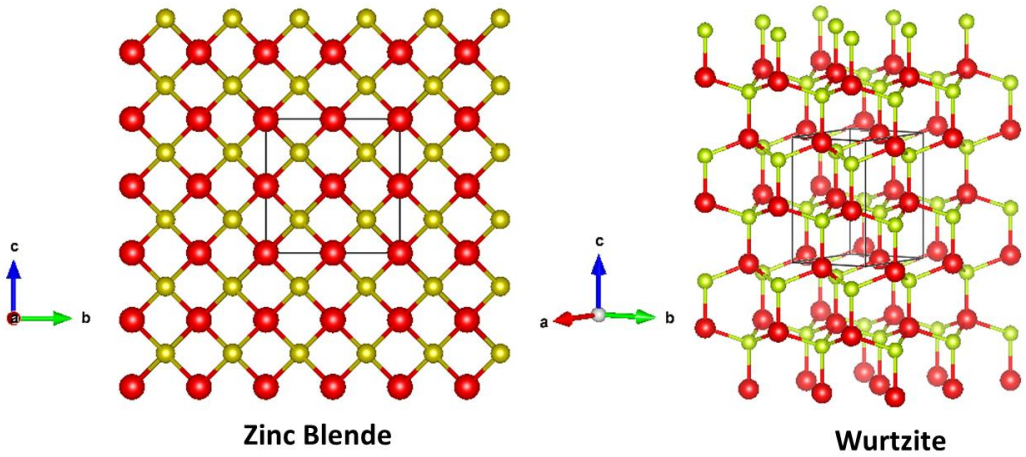

Figure 1.2. Cubic zinc blende and wurtzite (hexagonal) structure of ZnSe QDs.

1.7.4 Doped ZnSe quantum dots (QDs)

A new class of material is achieved by doping a quantum dots with transition metal ion, which is known as dilute magnetic semiconductors (DMSs). These doped semiconductor QDs can be utilized in broad diversity areas of different applications like potential luminescent materials (LEDs), spintronic and biomedical. For the successful incorporation of dopant ions into the host, there is a need for a simple and controllable synthesis technique. The main challenge in successful doping into the QDs is the "self-purification" nature of these materials in the nano regime, i.e., the host tends to expel out the dopant ions onto the surface because of the high surface energies. The transition metal ion-doped QDs are categorized by the exchange interaction involving the interactions between sp-d orbitals of host and dopant. The interaction of the d-orbital of the transition metal with the sp orbitals of the host is exhibited in terms of various fascinating physical phenomena. The Zeeman splitting of the electronic levels occurs due to doping, which results in enhancement and modification in the optical properties of the host. Further, doping helps against photo-oxidation during persistent illumination. The absorbed photons energy is transferred to the dopant impurities

through the localized excitation and controlling the unwanted surface reactions. The manganese (Mn^{2+}) doping in II-VI semiconductors shows fascinating optical and magnetic properties. First of all, in 1994, Bhargava *et al.* [36] have reported Mn^{2+} doped ZnS nanocrystals with a significant improvement in luminescence. Besides the enhanced photoluminescence intensity, the photoluminescence lifetime decreases dramatically from the ns to ms period [37]. This work has gained huge attention in doping numerous transition metal ions (Mn^{2+}, Cu^{2+}, $Co^{2+}$and Ni^{2+}) into various semiconductors hosts such as ZnS, ZnSe, CdS, CdSe, etc. [38]

Copper (Cu^{2+}) is another exciting and ideal transition metal ion being studied extensively. Cu^{2+} can act as a luminescence center and also enhance the magnetic saturation in the host lattice. Another significant behaviour of the Cu^{2+} ions, their emission wavelength changes with the variation of particle size. While the emission colour of Mn^{2+} dopant remains unchanged with the Mn^{2+} concentration changes and/or decreased particle size. The emission of Mn^{2+} dopant is generated through the localized wave function of the dopant cations and surrounding anions, which have no dependence on the particle size. But for the Cu^{2+} ions related emission, the recombination occurs between the delocalized charge carriers.

1.8. Applications

1.8.1 Quantum dot light-emitting diodes (QLEDs):

QLEDs are preferable to standard LEDs or OLEDs. Semiconductor QDs acquires unique optical properties. The tunability of semiconductor QDs allows them to emit nearly throughout the visible spectrum, while a conventional LED lacks this ability. QLEDs are an energy-efficient, reliable, tunable colour spectrum for lighting and display utilizations that reduce manufacturing costs [39].

QLEDs can provide a low-warmth, entire-spectrum source of light. At the identical colour point, it will provide 30 to 40% luminance efficiency over OLEDs, more than twice as compared with ordinary LEDs. With the capability to print vast-area on ultra-thin flexible substrates, QLEDs will reduce manufacturing costs. QLEDs will provide ultrathin, flexible and transparent form factors, which permit designers to develop new devices which are not possible through conventional LEDs. QDs are also deliberate for usage as white light-emitting diodes in liquid crystal display (LCD) televisions [40,41].

1.8.2 Quantum dot solar cell:

A quantum dot solar cell is similar to the conventional solar cell, but they use QDs instead of traditional materials as the absorbing photovoltaic material. The tunable bandgap property of QDs allows them to emit a broad range of energy levels by changing the QDs size, while in bulk materials, the bandgap is fixed according to preferred materials. This property makes QDs interesting for developing multi-junction solar cells, where different materials are used to boost efficiency by gathering multiple sites of the solar spectrum. The tunable bandgap of QDs allows the development of advanced solar cells. These QD cells would be capable of utilizing much higher of the sun's spectrum. QDs have been found to transmit up to 3 electrons per incident photon of sunlight compared to conventional photovoltaic cells. Theoretically, ZnSe QDs could raise solar power efficiency from 15-28% to as high as 64% [42].

1.8.3 Organic Dyes:

One of the most interesting advances in biotechnology is developing inorganic QDs with different chemical and optical properties but complex surface chemistry- as in vivo and in vitro fluorochrome (fluorophore). In medical diagnostics, QDs synthesized from II/VI & III/V semiconductors are the most repeatedly used nanocrystal labels. The QD's optical properties are restrained by the particle size, constituent material and surface

chemistry. QDs have been used for imaging and detection in various areas of the life sciences, grazing from in situ hybridization to in vivo imaging, microarray technology to fluorescence [43,44].

If the structure-property link is well-known for the given class of dyes, then only the optical properties of organic dyes can be fine-tuned by a detailed design approach [45,46]. In corresponding to organic dyes, QDs have the engaging property of absorption that gently rises toward lower wavelengths and a narrow emission band of mostly equal shape. The emission and absorption are tunable by particle size. The width of the emission peak is primarily driven by QD size allocation. The wide absorption grants a free selection of the wavelength for excitation and thus genuine separation of emission and excitation. QDs have relatively long lifetimes (usually five to hundreds of nanoseconds), allowing truthful material discrimination of the signal from scattered excitation light by time-gated evaluation, improving the sensitivity [47,48].

Given excellent optical properties of QDs such as long-term photostability, size-tunable emission and absorption, numerous colors with a single excitation source, excessively wide and intense absorption permissive unique adaptability in excitation, in this thesis, ZnSe and metal-doped ZnSe QDs of <5 nm were developed using an aqueous route synthesis. The prepared QDs were investigated using various tools and techniques. Photoexcitation dynamics of the QDs were explored in the microsecond to femtosecond time scale and at cryogenic temperature. Furthermore, the obtained well-defined QDs were used to monitor different metal ions and explosives in aqueous environments [49,50].

References

[1] N. Gaponik, D. V. Talapin, A. L. Rogach, K. Hoppe, E. V. Shevchenko, A. Kornowski, A. Eychmuller, H. Weller, Thiol-capping of CdTe nanocrystals: An alternative to organometallic synthetic routes, J. Phys. Chem. B 106 (2002) 7177-7185.

[2] S. V. Gaponenko, Optical properties of semiconductor nanocrystals, Cambridge University Press, Cambridge (1998).

[3] A. Hett, Nanotechnology: small matters, many unknown, (2004).

[4] G. C. La Rocca, Wannier–Mott excitons in semiconductors, thin films and nanostructures, Academic Press, 31 (2003) 97-128.

[5] P. N. Prasad, Nanophotonics. John Wiley & Sons, (2004).

[6] X. Wang, X. Kong, Y. Yu, Y. Sun, H. Zhang, Effect of annealing on upconversion luminescence of ZnO:Er3+ nanocrystals and high thermal sensitivity, J. Phys. Chem. C. 111 (2007) 15119–15124.

[7] R. Saleh, N. F. Djaja, Transition-metal-doped ZnO nanoparticles: Synthesis, characterization and photocatalytic activity under UV light, Spectrochim. Acta - Part A Mol. Biomol. Spectrosc. 130 (2014) 581–590.

[8] V. U. Huynh, J. J. Dittmer, A. P. Alivisatos, Hybrid nanorod-polymer solar cells, Science 295 (2002) 2425.

[9] R. D. Schaller and V. I. Klimov, High efficiency carrier multiplication in PbSe nanocrystals: Implications for solar energy conversion, Phys. Rev. Lett. 92 (2004) 186601.

[10] W. S. Coe, W. K. Woo, M. G. Bawendi, V. Bulovic, Electroluminescence from single monolayers of nanocrystals in molecular organic devices, Nature 420 (2002) 800-803.

[11] V. Tessler, V. Medvedev, M. Kazes, S. Kan, U. Banin, Efficient near-infrared

polymer nanocrystal light-emitting diodes, Science 295 (2002) 1506.

[12] A. Eychmuller, Structure and Photophysics of Semiconductor Nanocrystals, J. Phys. Chem. B, 104 (2000) 6514-6528.

[13] X. Wang, Y. Du, S. Ding, Q. Wang, G. Xiong. M. Xie, X. Shen, D. Pang, J. Phys.Chem. B, 110 (2006) 1566.

[14] G. Konstantatos, I. Howard, A. Fischer, S. Hoofland, J. Clifford, E. Klem, L. Levina, E. H. Sargent, Ultrasensitive solution-cast quantum dot photodetectors, Nature 442 (2006) 180.

[15] V. V. Nikesh, A. Dharmadhikari, H. Ono, S. Nozaki, G. R. Kumar, S. Mahamuni, Optical nonlinearity of monodispersed, capped ZnS quantum particles, Appl. Phys. Lett. 84 (2004) 4602.

[16] V. L Klimov. A. Mikhailovsky, S. Xu, A. Malko, J. Hollingsworth, C. A. Leatherdale, M. G. Bawendi, Optical Gain and Stimulated Emission in Nanocrystal Quantum Dots, Science 290 (2000) 314-317.

[17] N. Pradhan, D.M. Battaglia, Y. Liu, X. Peng, Efficient, stable, small, and water-soluble doped ZnSe nanocrystal emitters as non-cadmium biomedical labels, Nano Lett. 7 (2007) 312–317.

[18] M. Gao, S. Kirstein, H. Möhwald, A. L. Rogach, A. Kornowski, A. Eychmüller, H. Weller, Strongly photoluminescent CdTe nanocrystals by proper surface modification, J. Phys. Chem. B 102 (1998) 8360-8363.

[19] D. V. Talapin, A. L. Rogach, A. Kornowski, M. Haase, H. Weller, Highly Luminescent Monodisperse CdSe and CdSe/ZnS Nanocrystals Synthesized in a Hexadecylamine−Trioctylphosphine Oxide−Trioctylphospine Mixture, Nano Lett. 1 (2001) 207-211.

[20] F. V. Mikulec, M. G. Bawendi, S. Kim, Patent WO 01/07689.

[21] A. A. Guzelian, U. Banin, A. V. Kadavanich, X. Peng, A. P. Alivisatos, Colloidal chemical synthesis and characterization of InAs nanocrystal quantum dots, Appl. Phys. Lett. 69 (1996) 1432.

[22] Z. A. Peng, X. Peng, Formation of high-quality CdTe, CdSe, and CdS nanocrystals using CdO as precursor, J. Am. Chem. Soc. 123 (2001) 183-184.

[23] L. Qu, Z. A. Peng, X. Peng, Alternative routes toward high quality CdSe nanocrystals, Nano Lett. 1 (2001) 333-337.

[24] A. P. Alivisatos, W. Gu, C. Larabell, Quantum dots as cellular probes. Annu. Rev. Biomed. Eng. 7 (2005) 55-76.

[25] W.C. W. Chan, D. J. Maxwell, X. Gao, R. E. Bailey, M. Han, S. Nie, Luminescent quantum dots for multiplexed biological detection and imaging. Current opinion in biotechnology. 13 (2002) 40-46.

[26] A. Fu, W. Gu, C. Larabell, A. P. Alivisatos, Semiconductor nanoparticles for biological imaging. Current opinion in neural biology. 15 (2005) 568-575.

[27] X. Gao, L. Yang, J. A. Petros, F. F. Marshall, J. W. Simons, S. Nie, In vivo molecular and cellular imaging with quantum dots. Current opinion in biotechnology. 16 (2005) 63-72.

[28] X. Michalet, F. F. Pinaud, L. A. Bentolila, J. M. Tsay, S. Doose, J. J. Li, G. Sundaresan, A. M. Wu, S. S. Gambhir, S. Weiss, Quantum dots for live cells, in vivo imaging, and diagnostics. Science. 307 (2005) 538-544.

[29] U. R.-Genger, M. Grabolle, S. C. Jaricot, R. Nitschke, Thomas Nann Quantum dots versus organic dyes as fluorescent labels. Nature methods. 5 (2008) 763-75.

[30] R. Hardman, A toxicologic review of quantum dots: toxicity depends on physicochemical and environmental factors. Environmental Health Perspectives. 114 (2006) 165-172.

[31] J. Weng, J. Ren, Luminescent quantum dots: a very attractive and promising tool in biomedicine. Current medicinal chemistry. 13 (2006) 897-909.

[32] S. Xiong, S. Huang, A. Tang, F. Teng, Synthesis and luminescence properties of water-dispersible ZnSe nanocrystals, Mater. Lett. 61 (2007) 5091–5094.

[33] I.A. Mir, H. Alam, E. Priyadarshini, R. Meena, K. Rawat, P. Rajamani, M.S. Rizvi, H.B. Bohidar, Antimicrobial and biocompatibility of highly fluorescent ZnSe core and ZnSe@ZnS core-shell quantum dots, J. Nanoparticle Res. 20 (2018) 174-184.

[34] S. Shena, M. Jiaa, Z. Tanga, S. Changa, P. Shia, J. Yanga,b, Preparation and application of Mn-doped $Zn_{0.5}Cd0_{.5}S$@ZnS nanorods with high quantum yield as sensitive fluorescence probe for detection of glucose, Mater. Res. Bull 106 (2018) 471–477.

[35] A. Çelik, Ü. Çömelekoğlu, S. Yalin, A study on the investigation of cadmium chloride genotoxicity in rat bone marrow using micronucleus test and chromosome aberration analysis, Toxicol. Ind. Health. 21 (2005) 243–248.

[36] R. N. Bhargava, D. Gallagher, X. Hong, A. Nurmikko, Optical properties of manganese-doped nanocrystals of ZnS, Phys. Rev. Lett. 72 (1994) 416–419.

[37] C. Gan, Y. Zhang, D. Battaglia, X. Peng, M. Xiao, Fluorescence lifetime of Mn-doped ZnSe quantum dots with size dependence, Applied Physics Letters, 92 (2008) 241111.

[38] H. Li, Y. Li, Z. Zhang, X. Pang, X. Yu, Highly selective luminescent sensing of Cu^{2+} in aqueous solution based on a Eu(III)-centered periodic mesoporous organosilicas hybrid, Mater. Des. 172 (2019) 107712-107720.

[39] B. H. Kwon, K. G. Lee, T. J. Park, H. Kim, T. J. Lee, S. J. Lee, D. Y. Jeon, Continuous in situ synthesis of ZnSe/ZnS core/shell quantum dots in a

microfluidic reaction system and its application for light-emitting diodes, small, 8 (2012) 3257–3262.

[40] Quantum-dot LED may be screen of choice for future electronics, Massachusetts Institute of Technology News Office, (2002).

[41] H. Neidhardt, L. Wilhelm, V. A. Zagrebnov, A new model for quantum dot light emitting-absorbing devices: proofs and supplements, Nanosystems: Physics, Chemistry, Mathematics 6 (2015) 6–45.

[42] http://www.nanowerk.com/nanotechnology-news/newsid=39255.php.

[43] B. O. Dabbousi, J. Rodriguez-Viejo, F. V. Mikulec, J. R. Heine, H. Mattoussi, R. Ober, K. F. Jensen, M. G. Bawendi, (CdSe)ZnS core−shell quantum dots: Synthesis and characterization of a size series of highly luminescent nanocrystallites, J. Phys. Chem. B 101 (1997) 9463–9475.

[44] A. R. Shakoori, Fluorescence In Situ Hybridization (FISH) and Its Applications, Chromosome Structure and Aberrations (2017) 343–367.

[45] W. T. Mason, Fluorescent and luminescent probes for biological activity, Academic Press, (1999).

[46] S. Dähne, U. Resch-Genger, O. S. Wolfbeis, eds. NATO ASI Series, Hightechnology, Kluwer Academic Publishers, 52 (1998).

[47] M. Dahan, T. Laurence, F. Pinaud, D. S. Chemla, A. P. Alivisatos, M. Sauer, and S. Weiss, Time-gated biological imaging by use of colloidal quantum dots, Opt. Lett. 26 (2001) 825–827.

[48] H. E. Grecco, K. A. Lidke, R. Heintzmann, D. S. Lidke, C. Spagnuolo, O. E. Martinez, E. A. Jares-Erijman, T. M. Jovin, Ensemble and single particle photophysical properties (two-photon excitation, anisotropy, FRET, lifetime, spectral conversion) of commercial quantum dots in solution and in live cells,

Microsc. Res. Tech. 65 (2005) 169–179.

[49] V. Sharma, M.S. Mehata, Synthesis of photoactivated highly fluorescent Mn^{2+}-doped ZnSe quantum dots as effective lead sensor in drinking water, Mater. Res. Bull. 134 (2021) 111121.

[50] V. Sharma, M.S. Mehata, Rapid optical sensor for recognition of explosive 2,4,6-TNP traces in water through fluorescent ZnSe quantum dots, Spectrochim. Acta-Part A Mol. Biomol. Spectrosc. 260 (2021) 119937.

Chapter 2

Experimental and characterization techniques

After the successful synthesis of materials, an intensive and appropriate characterization of materials is necessary. Characterization of synthesized material provides a superior understanding as well as gives ideas on its potential applications. The characterization techniques give an observable and measurable insight of materials with a high atomic-level resolution of accuracy and sensitivity. To determine nanoparticle-specific properties, we apply different characterization and analytical methods depending on the physical or chemical quantity to be determined. Today, high-precision nanoscale measurement and testing technologies are available in laboratories to characterize and analyze nanomaterials. Scanning electron microscopy, scanning tunneling microscopy, X-ray spectroscopy, Mass spectrometry, Optical methods, Fourier transform infrared spectroscopy, x-ray diffraction and many more.

In this present work, we have analysed the pure and transition metals doped/co-doped zinc selenide quantum dots synthesized by direct aqueous route using different characterization techniques namely scanning electron microscopy(SEM), X-ray diffractometer(XRD), Fourier transform Infrared spectroscopy (FTIR), high-resolution transmission electron microscopy (HRTEM) and their optical performance were recorded by tools like UV/Vis/NIR absorption spectroscopy, photoluminescence spectroscopy, time-correlated single-photon counting system (TCSPC) and transient absorption spectroscopy, which are discussed as follows.

2.1 X-ray diffraction

X-ray diffraction (XRD) for powder is a fundamental and well-recognized characterization technique adopted for the phase determination of crystalline materials

and also gives information about the lattice parameters or unit cell dimensions. The investigated material should be homogenized, properly dried and finely grounded.

The fundamental principle of X-ray diffraction

In 1912, a discovery made by Max von Laue for crystalline materials stated that the spacing of planes in a crystal lattice acts as 3-D diffraction gratings for X-ray wavelengths. Nowadays, X-ray diffraction is one of the primary and powerful techniques for determining the crystal structures and atomic spacing in nanomaterials. The working principle of XRD is based on the constructive interference of monochromatic X-rays and crystalline materials. X-rays are generated when a highly accelerated electron beam hits a metal cathode ray tube which is further filtered to generate monochromatic radiation. Additionally, the monochromatic radiation is collimated to concentrate and focus it towards the analysed material. The constructive interference (and a diffracted ray) is generated by the interaction between the incident rays and the sample in such a way that Bragg's law conditions ($n\lambda=2d\sin\theta$) are satisfied [1,2].

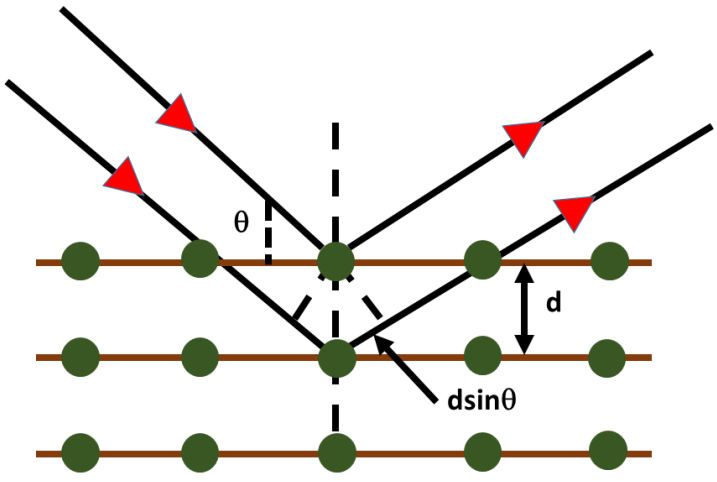

Figure 2.1: Schematic representation of Bragg**'s** law of x-ray diffraction.

This law gives the relation between the wavelength of the electromagnetic radiation and the diffraction angle in a crystal. All the possible diffraction directions of the lattice due

to the random orientation of the powdered material should be attained by scanning the sample over a wide range of 2θ angles. Each material has a set of unique d-spacing. Thus, determining the d-spacing using diffraction peaks and comparing d-spacing with standard reference patterns permits the identification of the materials. The angle between the incident and diffracted rays is the key component of all diffraction.

Instrumentation of powder XRD:

X-ray diffractometer consists of three main elements, i.e., X-ray tube, X-ray detector and a sample holder. X-rays are generated by heating a filament at increased temperature, producing electrons in the cathode ray tube. Afterward, electrons are accelerated towards the target by applying a voltage bombarded onto the target. The characteristic X-ray spectra are obtained when the accelerating electrons with sufficiently large energy remove the target material's inner shell electrons. Several bands are produced in the obtained spectra, of which the most common bands are K_α and K_β. The K_α band further consists of two sub-bands, i.e., the $K_{\alpha1}$ and $K_{\alpha2}$ bands. The intensity of the $K_{\alpha1}$ is twice of $K_{\alpha2}$ and has a slightly shorter wavelength. To produce monochromatic X-rays, the filtering of spectra by foils or crystal monochromators is needed for the diffraction method. A weighted average of $K_{\alpha1}$ and $K_{\alpha2}$ is used as these two are significantly close in wavelength. The most commonly used target for single-crystal diffraction is copper having CuK_α radiation with a wavelength of 1.5418 Å. These collimated X-rays are focused on the sample. Once the X-rays interact with the sample, the reflected X-rays intensity is recorded using a rotating detector. When the X-rays incident on the sample fulfils the Bragg′s condition a constructive interference follows, which results in intense peaks. Produced X-ray signals are recorded on a detector that converts the signal into counts rate, then transferred to the computer monitor, an output device.

The X-ray diffractometer is designed in a way that it easily collects the diffracted X-rays with the detector fitted on one of its arms, while the sample rotates in the path of the collimated X-ray beam and the rotation between detector and X-ray beam is always at an angle of 2θ. The angel and rotation of the sample are preserved using a Goniometer. For typical powder samples, the data is recorded at an angle of 2θ ranges from 10° to 80°, which should be preset before every X-ray scan.

Figure 2.2. Powder X-ray diffractometer, Bruker, D8 Advance.

Applications of X-ray diffraction

The main function of XRD is the characterization of crystalline materials (e.g., inorganic compounds, minerals) and identifying unknown materials. Identifying unknown materials has significant importance to studies in material science, engineering, biology, environmental science and geology.

Additional important applications include:

- characterization of crystalline nanoparticles

- perform Rietveld refinement to determine crystal structures
- measurement of sample purity
- determination of unit cell dimensions
- quantitative analysis- determine modal amounts of minerals
- calculated lattice mismatch, stress and strain
- measuring super lattices in multi-layered epitaxial structures.

2.3. Fourier Transform Infrared Spectroscopy

In Fourier Transform Infrared Spectroscopy (FTIR), the infrared radiations are passed through the sample, a part of which is absorbed by the sample, and the remaining is transmitted through it. As a result, molecular absorption and transmission spectrum are obtained, which represents the molecular fingerprints of the sample. Different molecules give a unique infrared spectrum like a unique fingerprint scan. Thus, infrared spectroscopy is an essential tool for numerous types of analysis.

• It can be used to determine the sample's quality or its consistency.

• Using it, one can identify or characterize the unknown materials.

• Number of components in a mixture can also be determined using it

To overcome the restrictions encountered with dispersive instruments, FTIR spectrometry was developed. The main difficulty was the slow scanning rate. An advanced method was needed for fast and simultaneously scanning all the infrared frequencies, rather than individually. This problem was solved by employing an interferometer, a simple optical device [3]. The interferometer generates a unique encoded signal containing all ranges of the infrared frequencies. These signals can be recorded in the order of one second. Thus, they give a shortened scan time per sample, decreasing it from several minutes to a few seconds. A beam-splitter is employed in the interferometers to divide the incoming infrared beam into two optical beams. These two

beams travel towards their respective mirrors and reflect off. Then they recombined after coming back at the beam-splitter. There is a path difference between these two beams resulting from one fixed path beam and the other with a constantly changing path due to the movement of its mirror (typically a few millimeters).

Thus, the output signal of the interferometer shows a resultant “interfering” beam. The resulting signal is an interferogram that provides information on every unique property of the infrared frequency as a function of the changing mirror position. So, one can say that the recoded interferogram has all frequencies being measured simultaneously. But the specialist needs a frequency spectrum to identify, i.e., the plot of intensity vs. individual frequency. The recorded interferogram can’t be interpreted directly, individual frequencies are required to be decoded for the same. The decoding of the interferogram can be accomplished by using the Fourier transformation, i.e., a well-known mathematical technique. This can be done using a computer system that gives the desired spectral information for analysis in output.

Figure 2.3. FTIR Spectrometer NICOLET–380.

Advantages of FTIR

Advantages of FT-IR over the dispersive technique,

• Has high scan speed, which is also known as Felgett advantage.

• Has high sensitivity, which is referred to as the Jacquinot advantage.

• Internally calibrated through a HeNe laser as an internal wavelength calibration standard.

• Having mechanical simplicity with very little possibility of mechanical breakdown.

2.4. Field emission scanning electron microscopy

A scanning electron microscope (SEM) consists of a focused electron beam of high energy, which generates a range of signals at the solid specimen. After the interaction of the electron beam with the sample, a signal is produced which reveals various information about the material sample, including crystalline structure, chemical composition, external morphology and orientation of materials building up the sample. The data or information are recorded by scanning a small sample area, and 2D images are acquired, which shows the spatial variations in the above-listed properties. The typical selected area for conventional SEM imaging ranges approximately 1 cm to 5 microns in width with a spatial resolution of 50 to 100 nm. The magnification offered in the range from about 20X to 30,000X.

Figure 2.4. Scanning Electron Microscope, Model: Zeiss, Gemini SEM 500.

In SEM analysis, various singles are produced from the sample after the interaction with an electron beam. In general, the most commonly used detection mode in SEM is secondary generated electrons detection. The generation of secondary electrons varies with the angle of the beam at which it interacts with the surface of the specimen. A special detector is used to collect the secondary electrons after the scanning of the sample. Then an image is created by the recorded data, which displays the topography of the surface [4].

Principle of scanning electron microscopy

In SEM, a high energetic accelerated electron with a significant amount of kinetic energy interacts with a solid sample. The incident electrons are deaccelerated by their interaction with the sample releasing energy in the form of various signals. These signals comprise of diffracted backscattered electrons, photons (characteristic X-rays used for elemental analysis and continuum X-rays), secondary electrons (they are responsible for producing SEM images), backscattered electrons (BSE), visible light (cathode luminescence) and heat. Secondary and backscattered electrons are used for sample imaging; secondary electrons are given the topography and morphology of samples. The backscattered electrons are suitable in multiphase samples for showing contrasts in composition.

Applications of SEM

SEM is widely adopted to acquire high-resolution images of samples and also give the confirmation of spatial variations in chemical compositions:

- Determination of phases based on the mean atomic number using backscattering electrons (BSE).
- Acquiring elemental composition or chemical analyses using EDS.

- Elemental compositional mapping is also done based on differences in trace element "activators".
- SEMs equipped with BSE detectors can be employed for many materials to study micro-fabric and crystallographic orientation.
- Precise and very small feature measurements, i.e., the particle size up to 50 nm, can also be acquired through the SEM.

2.5 High-Resolution Transmission Electron Microscopy

HRTEM-High Resolution Transmission Electron Microscopy is a powerful device used to imaging nanoparticles on the atomic scale to study their morphologic, size, structure, and compositional properties. Simultaneously, it can also provide information in real and reciprocal spaces in imaging and diffraction patterns, respectively. In the HRTEM technique, a high-energy electron beam (~1 MeV) supplied by a thermionic or a field-emission gun is accelerated towards the specimen using a positive electrical potential. These electrons are then focused using electromagnet condenser lenses into a focused monochromatic beam. The beam passed through the specimen, with several interactions occur. The transmitted electrons are then focused using an additional electromagnetic lens termed the “objective lens,” then collected by a detector to form a magnified sample image and give the morphology. The resolution of TEM images depends upon the value of the spherical aberration coefficient of the objective lens and the wavelength of electrons used. The transmitted beam of electrons undergoes a line of multiple “intermediate lenses,” which enlarges the image, depending upon the set magnification. After that, the transmitted beam hitting the phosphor screen and light is engendered, attached to sensors such as a charge-coupled device (CCD) camera for users to see the image. The denser or thicker region is obtained as darker areas of the sample because

only fewer electrons were transmitted. The less-dense or thinner areas give a lighter image because more electrons were transmitted from these parts.

HRTEM has been successfully and extensively adopted for analyzing lattice imperfections and crystal structures on an atomic level. It is widely used for material characterization and different studies as surface structures, precipitates grain boundaries, dislocations, stacking faults and point defects. It is also moderately suitable to study various information in reciprocal space, i.e., the information about the material phases using the diffraction of electrons from the specimen [5]. For this work, we used the TALOS, Thermo scientific instruments, HRTEM at an accelerating voltage of 200kV.

Figure 2.5. HR-TEM Thermo Scientific, Talos.

2.6. UV/Vis/NIR Absorption Spectrophotometer

Absorption spectroscopy is a fundamental technique used to study optical properties of semiconductors nanocrystals or QDs, thin-film and insulators in bulk. Insulating and semiconducting materials possess an optical bandgap, so absorption takes place when the incident photon has sufficient energy to excite electrons from the valance band to the conduction band. Absorption spectra reveal the transition energy associated with its different excitonic levels. To study electronic structure and transitions from valance to conduction band, ultraviolet to near-infrared radiation is preferred, and absorbed intensity as a function of wavelength is recorded and obtained as spectra between in absorbance (A) versus wavelength [6].

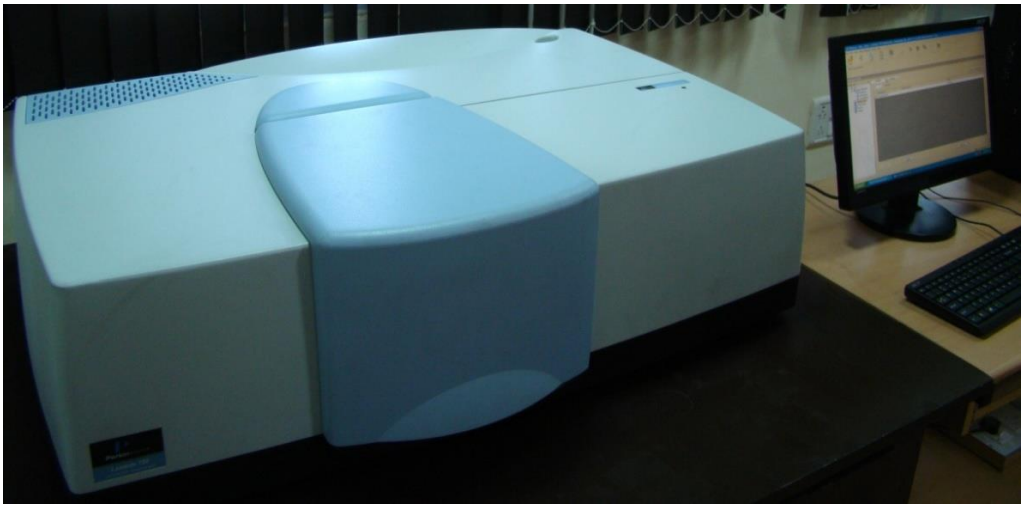

Figure 2.6. UV/Vis/NIR spectrometer, Model: Perkin Elmer LAMBDA-750.

In the present investigation, Perkin Elmer, UV/Vis/NIR Lambda-750 spectrometer equipped with deuterium and tungsten lamps is used, and the real captured image is illustrating in Figure 2.6. This spectrophotometer consists of a double beam system and monochromator with 190 nm to 3200 nm wavelength range with an accuracy of ± 1.5 nm. With the help of diffraction grating, a single beam of radiation is divided into its different components. A monochromator is used to separate each

wavelength and after that, through half mirror devices, the monochromatic beam is split into two equal intensity beams. From these two beams, one beam is used as a reference to eliminate the unwanted signals. The absorbance (A) can be calculated as per the following equation:

$$A = -\log\left(\frac{I}{I_0}\right) \quad (2.1)$$

where I_0 is the initial radiation intensity and I is the absorbed intensity. The absorption of radiation by the sample should be followed by the Beer-Lambert Law,

$$A = -\varepsilon c l \quad (2.2)$$

where ε represents the molar absorption coefficient, c denotes the solution concentration, and l is the absorption path length. This law is also useful for finding the unrecognized concentration of the samples.

2.7. Photoluminescence spectroscopy

Photoluminescence spectroscopy is a powerful and non-destructive optical characterization technique that probes the electronic structure with discrete energy levels of materials. The photoluminescence spectrum can provide additional information about the samples like quantum yield, mono-dispersibility, quenching phenomena, etc. Photoluminescence is a process in which the incident photons, i.e., electromagnetic radiation, are absorbed by the material and this absorbed energy is re-emits the photons. The photo-excitation phenomena occur, which states that when the material is excited with energy greater than its threshold value (with photons), the electrons in the valence band are excited towards the higher energy levels. After a short period, these excited electrons return and relax to the ground state with radiative or non-radiative relaxation processes of photons.

If the relaxation process is radiative or occurs with the emission of a photon, then the process is known as photoluminescence. The photoluminescence spectra offer the

identification of transition energies, impurity levels, defects and disorders in the samples, which can be very useful to determine the electronic energy states [7,8]. In the process of measuring the photoluminescence spectra, first of all, to identify the excitation wavelength for the material and fixed it for collecting the emission intensity as a function of wavelength. Whereas in the case of measurement of photoluminescence excitation spectra, the emission wavelength is kept fixed, and the intensity of photoluminescence is recorded as a function of wavelength. The band in the excitation spectrum has only appeared for the excitation line corresponding to the fixed emission.

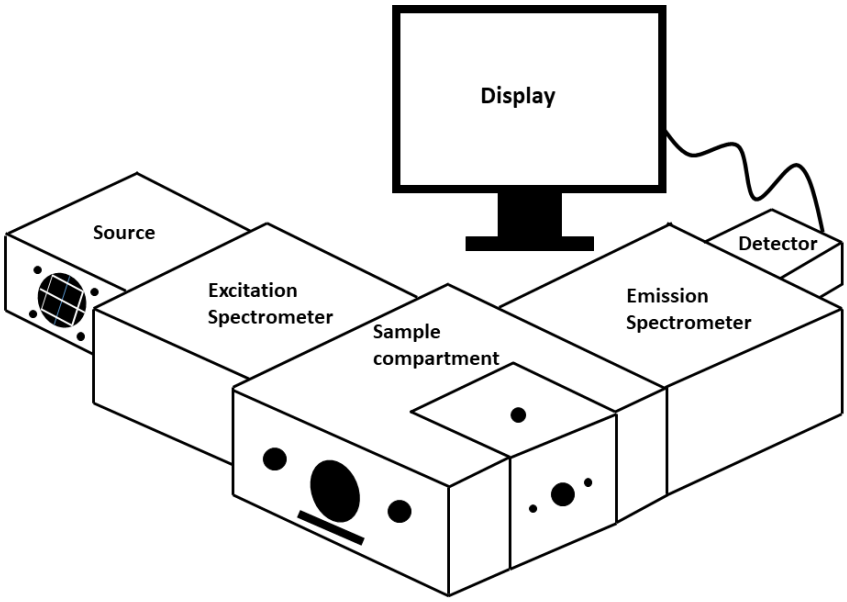

Figure 2.7. Schematic representation of Horiba Scientific Fluorolog-3 spectrofluorometer.

In the present study, photoluminescence studies were performed using Horiba Scientific Fluorolog-3 spectrofluorometer, equipped with Hamamatsu R928P photomultiplier tube (PMT) detector and double-grating at excitation as well as at emission monochromators (1200 grooves/mm) as represented by the schematic diagram (Figure 2.7). Most of the measurements were carried out at room temperature with an excitation source of 450 Watt continuous wavelength Xenon (Xe) lamp for UV

to the near-IR excitation wavelength. Figure 2.8 illustrates the real image of the instrument used for the photoluminescence studies.

We also adopted the photoluminescence instrument to measure photoluminescence decay of Mn@ZnSe QDs in some of our work using Xenon pulsed lamps as the excitation source. The obtained decay curves were fitted using the bi-exponential function as given by the Equation,

$$f(t) = \alpha_1 \exp\left(-\frac{t}{\tau_1}\right) + \alpha_2 \exp\left(-\frac{t}{\tau_2}\right), \quad (2.3)$$

Where τ_1 and τ_2 are the lifetime components and α_1 and α_2 are corresponding amplitudes [55], also, the average lifetime was calculated by employing the equation:

$$< \tau > = \frac{\alpha_1\tau_1^2 + \alpha_2\tau_2^2}{\alpha_1\tau_1 + \alpha_2\tau_2}, \quad (2.4)$$

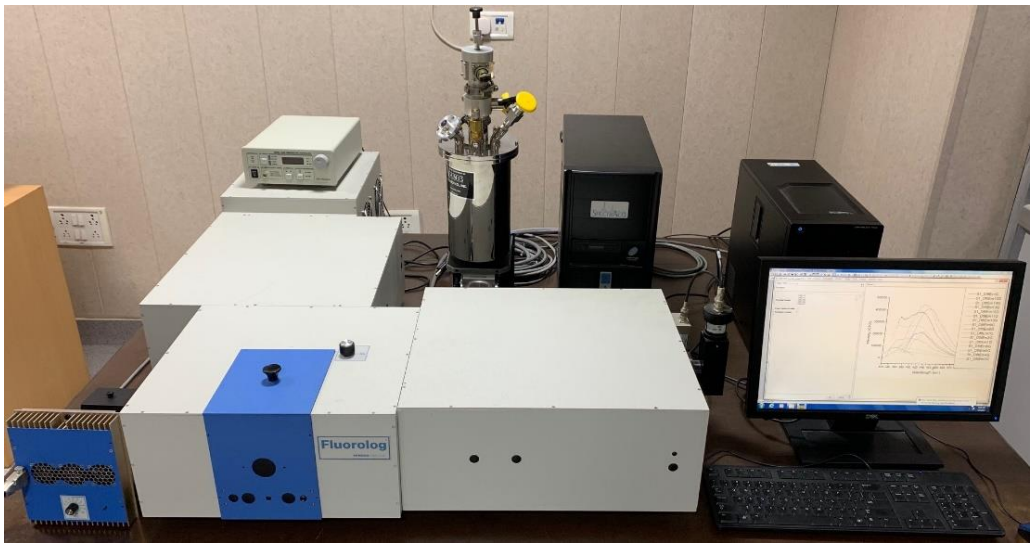

Figure 2.8. Photoluminescence spectrofluorometer set up.

2.8. Time-correlated single-photon counting system

Time-correlated spectroscopy for photon counting is a powerful and vital characterization technique for recording the fluorescence lifetime. It uses an excitation pulse to count the time-correlated photons and a time to amplitude converter (TAC). A short flash laser pulse is used for the time-dependent intensity profile recording [9]. The time-correlated single-photon counting system working involves the total time taken

between an excitation pulse emitted by a pulsed laser source and the generated (re-emitted radiation) fluorescent photon recorded at a photomultiplier tube (PMT). The time correlation between the excitation and emission events is achieved by using a time-to-amplitude convertor. The instrument response function (IRF) or an intensity-time profile of the laser pulse were recorded for the correction factor employing Stokes or Rayleigh Raman scattering by using a LUDOX solution at an appropriate wavelength [10].

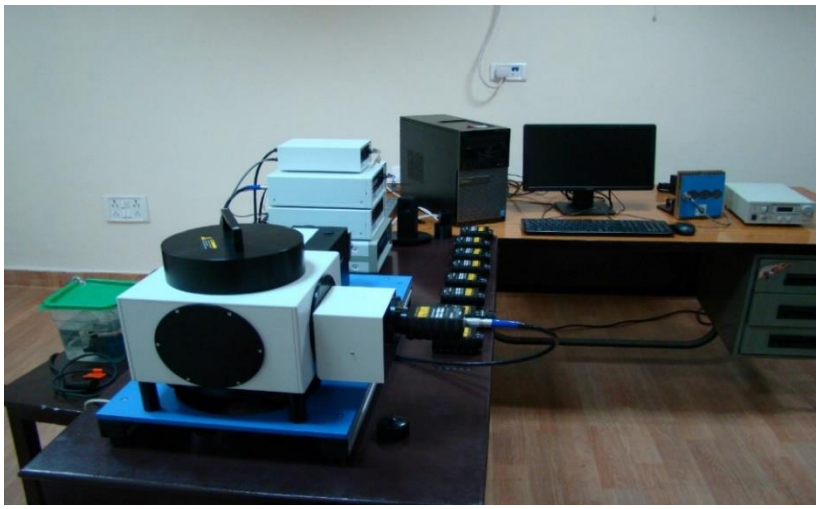

Figure 2.9. Time-correlated single photon counting system, DeltaFlex-01-DD.

All the fluorescence lifetime measurements were performed using Horiba Jobin Yvon, DeltaFlex-01-DD, time-correlated single-photon counting system equipped with Delta diode laser (in this work, we used 450 nm wavelength source) as pulse source and PPD.850 as a detector. The recorded data was analysed or fitted through the least square fitting method provided in the software installed with the time-correlated single-photon counting system by Horiba. The real image of the setup used for lifetime measurements is shown in Figure 2.9.

2.9. Transient absorption spectroscopy

The ultrafast transient absorption spectroscopy opened a new area of research to investigate the photophysical and photochemical reactions in real-time with the

femtosecond. The ultrafast transient absorption spectroscopy can measure the kinetics of atoms, molecules that have short-lived and non-phosphorescent populations within the triplet state decay path. The ultrafast transient absorption spectroscopy was carried out for all the transient absorption data acquisition through the pump probe method. A pump pulse of 30 fs with maxima at 360 nm was taken to excite the QDs. The sample holder is a 300 μm cell, which was positioned between incident laser pulses. The spectra obtained was corrected for the group delay dispersion of the supercontinuum by the method described below:

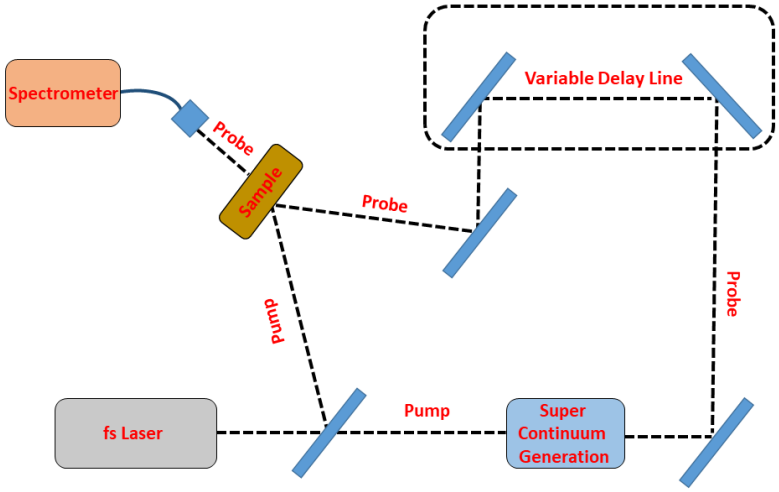

Figure 2.10. Ray diagram of transient absorption working.

The regenerative amplifier system (Spitfire, Spectra-Physics, USA) intensifies the output of a Ti:sapphire oscillator (800 nm, 80 MHz, 80 fs, Tsunami, Spectra-Physics, Santa Clara, CA, USA). The femtosecond gauss pump pulse of 200 nJ, 30 fs centered at 360 nm was used to excite the samples. The probe pulse was light of supercontinuum generated in H_2O cell by focused 800 nm femtosecond pulses. Transient absorbance change ΔA (t, λ) was measured over a wide wavelength range from 380–800 nm. During the pump-probe technique, the time window of the "coherence spike" was observed and neglected for the overlap. The pump beam frequency was reduced to half (500

Hz) using a chopper to obtain the difference spectra (DA) signal and the sample was then pumped at a fluency of ~20 μJ/cm^2. A visible light probe was used to experiment, while a highly stable output pump beam from TOPAS having a wavelength of 450 nm was used to excite the sample. In the present experiment, a time delay up to 2000 ps was conducted. The ray diagram of the working of transient absorption spectroscopy is represented in Figure 2.10. Surface Xplorer V4.0 and Origin 9.1 software are used to simulate the recorded experimental data.

References

[1] B. Cullity, Elements of x-ray diffraction, Second edition., Addison-Wesley Publishing Company Inc., Reading MA, 1978.

[2] H.M. Moghaddam, S. Nasirian, Dependence of activation energy and lattice strain on TiO_2 nanoparticles? , Nanosci. Methods. 1 (2012) 201–212.

[3] P. Larkin, Infrared and Raman spectroscopy: principles and spectral interpretation. Elsevier, 2017.

[4] R.F. Egerton, Physical principles of electron microscopy: An introduction to TEM, SEM, and AEM, Phys. Princ. Electron Microsc. An Introd. to TEM, SEM, AEM. (2005) 1–202.

[5] S.M. Bhagyaraj, O.S. Oluwafemi, N. Kalarikkal, S. Thomas, Characterization of nanomaterials: Advances and key technologies, Charact. Nanomater. Adv. Key Technol. (2018) 1–390.

[6] G. Wypych, Handbook of UV Degradation and Stabilization: Second Edition, Handb. UV Degrad. Stab. Second Ed. (2015) 1–419.

[7] C.R. Ronda, Luminescence : from theory to applications, (2008) 260.

[8] J.R. Lakowicz, Introduction to Fluorescence, Princ. Fluoresc. Spectrosc. (1983) 1–18.

[9] K. Wakabayashi, Y. Yamaguchi, T. Sekiya, S. Kurita, Time-resolved luminescence spectra in colorless anatase TiO_2 single crystal, J. Lumin. 112 (2005) 50–53.

[10] D. V. O'Connor, D. Phillips, Time-correlated single photon counting, (1984) 288.

Chapter 3

Synthesis of Mn^{2+}-doped ZnSe quantum dots for lead ions sensing in drinking water

3.1. Introduction

II-VI semiconductor quantum dots (QDs)/nanoparticles (NPs) have been considered as vibrant materials by the scientific community due to their excellent size-specific optical properties and biocompatibility [1-3]. QDs have unique features that include high quantum confinement, large active surfaces, high resistance to photo-bleaching, size-dependent tunable strong absorption and emission with broad photoexcitation and narrow band. These unique features expand the application of QDs as an active component for many devices like blue light-emitting lasers, photodetectors, light-emitting diodes (LEDs), photo-catalysis, sensitive luminescence-based probes for various biological purposes and in sensing of many health-hazardous heavy metal ions [4-15]. In the present era, heavy metal contamination in water and the quality of drinking water is the primary concern due to their high toxicity and hazardous effects on human health and other living organisms [16-19]. Notably, lead is well known for its highly toxic nature and its environmental impact, which causes a severe impact on human health. This hazardous element comes up from many industrial or natural sources, *i.e.*, lead has been distributed by various textile and batteries production industrial waste and some natural processes such as volcanic activity. Even at low concentrations, lead damages to the aquatic environment and microorganisms. Besides,

[*] *Content of this chapter have been published in* ***Materials Research Bulletin 134 (2021) 111121.***

lead-poisoning results in neurotoxic damages, mainly in children from its non-degradable nature. Thus, drinking water polluted with lead leads to several severe disorders in addition to neurological damage. Consequently, developing a sensitive, water-soluble, fast, cheap and reliable metal sensor for detecting lead in drinking water has a great significance. Many researchers have reported metal ion sensors using CdSe and CdS quantum dots [20-24], but due to their high toxicity, cadmium placed the CdX (X= Se, Te, S) QDs in an unfavorable position for the sensing and especially the biological applications. Cadmium could be leaked from CdX nanoparticles and may become a severe issue for biological systems and cause many environmental problems [25-27]. Thus, presently the priority is to search the non-cadmium alternatives, biocompatible, non-toxic QDs, which can be used for sensing. Therefore, ZnSe is one of the leading semiconductor QDs and gained great attraction because of its non-toxic nature for many applications such as photodetectors, sensors, color displays and biological applications [28-30].

For several decades, zinc chalcogenide-based II-VI semiconductors with paramagnetic impurities have been studied and are well-known as "diluted magnetic semiconductors" materials, possessing great applications for spintronic devices [31]. The most remarkable categories of diluted magnetic semiconductors are Mn^{2+} ions dopants, which produced visible (orange) emission due to the recombination in Mn^{2+} dopant ion center. In 1994 Bhargava *et al.* [32] reported that it was promising to attain efficient emission from Mn@ZnSe QDs synthesized by colloidal approaches. Mn^{2+}-doped ZnS QDs have been broadly explored in different fields [33-34]. The direct aqueous medium synthesis of water-dispersible, highly emissive Mn^{2+}-doped ZnSe/ZnS core-shell nanocrystals with MPA as capping ligand was reported firstly by Fang *et al.* [35]. In some cases, the metal ions could cooperate with colloidal QDs via

coordinate bonds, *e.g.*, metal sulfide (M–S) bond, which results in strong quenching of emission intensity due to aggregation or electron transfer from colloidal QDs. On the other hand, some quenching processes are stimulated or initiated via a collisional process. The detection of such fluctuation and quenching in the signals by numerous operative methods leads us to detect heavy metal ions. Further, the fluorescent sensors should have good biocompatibility, low toxicity, significant quantum yield, and photostability for sensing and imaging applications. Thus, the Mn@ZnSe QDs may be considered novel fluorescent probes due to their high PL intensity and non-toxic nature compared to CdX based nanoparticles/QDs [36].

Herein, cadmium-free quantum dots were prepared by aqueous synthesis method and capped or protected by the thiol functional group, which are accessible as the best substitute compared to dyes and organic fluorophores. Mn^{2+}-doped ZnSe QDs were directly synthesized in the aqueous medium with MPA capping [37]. The synthesized Mn@ZnSe QDs act as a sensing probe for heavy metal ions detection and show promising selectivity and high sensitivity towards Pb^{2+} ions in ultrapure, tap water and Yamuna river water. To test the selective and interference response of Mn@ZnSe QDs, the PL was measured in the presence of eleven different metal ions. We have reported Mn@ZnSe QDs as an active lead (Pb^{2+}) sensor in ultrapure DI water and drinking water.

3.2. Experimental

3.2.1. Materials and methods

All chemicals are of the AR spectroscopic mark and used without further purification. Sodium borohydride (95%) and manganese (II) chloride (99%) from CDH, and selenium powder (99.5%) from Sigma-Aldrich. Zinc acetate dihydrate (98%) and 3-mercaptopropionic acid (MPA, 99%) were procured from Acros Organics and ethanol

from Alfa Aesar. The metal ions used in the sensing experiment are lead (II) perchlorate trihydrate, cadmium (II) chloride hydrate, cobalt (II) perchlorate hexahydrate, aluminium (III) perchlorate nonahydrate, zinc (II) perchlorate hexahydrate, calcium (II) perchloride tetrahydrate, magnesium (II) perchloride hexahydrate, nickel (II) perchlorate hexahydrate, barium (II) perchlorate anhydrous, iron (II) perchlorate hydrate and iron (III) perchlorate hydrate were purchased from Sigma Aldrich having purity (99.8%). The ultrapure water was used in the synthesis process, having a resistivity 18.2 MΩ cm.

3.2.2. Synthesis method for water-dispersible Mn@ZnSe QDs

Water-dispersible and highly stable Mn@ZnSe QDs were prepared via a direct aqueous medium route by using mercaptopropionic acid (MPA) as a stabilizing ligand and adopted nucleation doping strategy. To synthesize Mn^{2+}-doped ZnSe QDs, a nucleation doping strategy with appropriate modifications was used. The synthesis process was performed in an inert environment under the continuous flow of N_2 gas through the reaction vessels and maintained the pH of the solution to be 10.3. The freshly prepared stock solution of NaHSe at room temperature by the reaction of selenium powder (Se) and sodium borohydride ($NaBH_4$) in distilled water was added to the three-neck flask (250 mL) that already containing zinc acetate (Zn^{2+}) precursor at 80℃ and simultaneously added 0.1 mM solution of manganese chloride (Mn^{2+}). After a few minutes, 1 mL MPA was added as a capping agent to the solution and then kept the Mn@ZnSe QDs at the same temperature for 20–30 min. Further, decrease the temperature and keep the solution at 70 ℃ for a reflux time of 90 min. for the growth of QDs. After that, switch off the heating and the solution was cool down freely under constant stirring at room temperature. MPA complex and other impurities from quantum dots were purified and separated via repetitive centrifuge with excess absolute

ethanol and distilled water to eliminate unreacted precursors. Finally, the QDs were then exposed with the UV for the photoactivation process of about 90−120 min.

3.3. Characterization techniques

The UV−vis spectroscopic studies were performed with Perkin-Elmer, Lambda-750 dual-beam UV/VIS spectrometer, Steady-state photoluminescence (PL) and time-resolved photoluminescence (TRPL) measurements were carried out with Fluorolog-3 spectrofluorometer, Horiba Jobin Yvon, equipped with photomultiplier tube (PMT) and 450 W xenon and flash lamps. A quartz cuvette was used as the sample container with an optical path of 10 mm. X-ray diffraction (XRD) pattern was obtained with Ultima IV, Rigaku operated at an acceleration voltage of 40 kV and using Cu (K_α) radiation. High-resolution transmission electron microscopy (HRTEM) images were captured by TALOS (Thermo scientific instruments) operated at an accelerating voltage of 200 kV. For the photoactivation process, samples were exposed to a Cole-Parmer UV lamp with a wavelength of 254 nm of 8 W and an irradiation dose of 1.2 Mw/cm^2 for 90-120 min.

3.4. Results and discussion

3.4.1. X-ray diffractometry

Fig. 3.1 illustrates the XRD pattern of Mn@ZnSe QDs taken by depositing the sample on a glass cover slide using a drop-cast technique. ZnSe has two types of crystal structures, one is hexagonal and the other is the cubic zinc blende. In low-temperature aqueous synthesis, the often obtained structure is a cubic zinc blende. The characteristic diffraction peaks corresponding to the diffraction planes (111), (220) and (311) of ZnSe crystal are observed at 2θ angles 27.2, 45.3 and 53.6°, respectively which are matched with cubic zinc blende structure (JCPDS card: 80-0021). The result indicates the incorporation of the Mn^{2+} dopant does not affect the structure of the crystal lattice. The broad diffraction peaks indicate the nano-crystalline nature of the synthesized QDs.

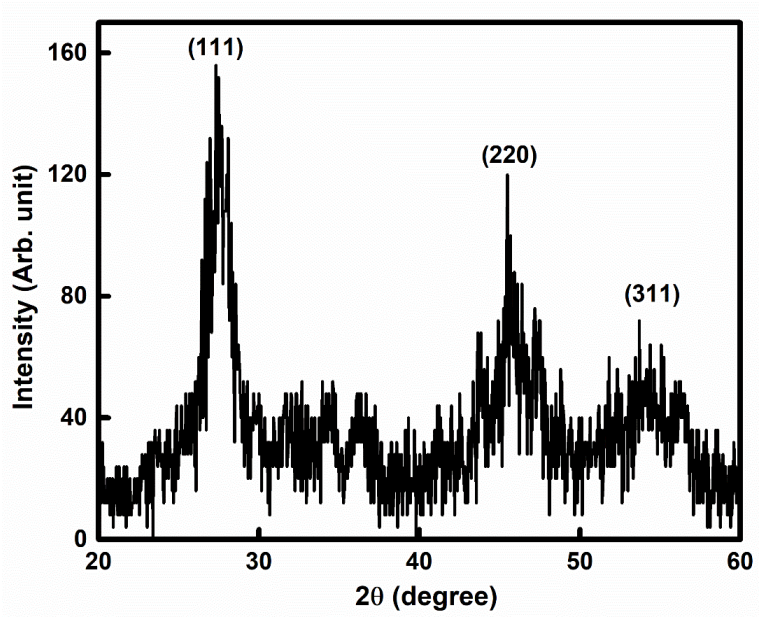

Figure 3.1. XRD pattern of Mn@ZnSe QDs having the cubic zinc blende crystal structure.

The average crystallite size (D) of synthesized Mn@ZnSe QDs was estimated by using Scherrer's equation $D = \frac{k\lambda}{\beta \cos\theta}$ is 3.8 nm. Here, ***k*** denotes the shape factor having a value of 0.89, λ denotes the X-ray wavelength corresponding to Cu K_α radiation, β denotes the full-width at half maximum (FWHM) of observed peak and θ represents the diffraction Bragg′s angle.

3.4.2. Transmission electron microscopy (TEM)

Fig. 3.2 illustrates the TEM (Fig. 3.2a) and HR-TEM (Fig. 3.2b) images of Mn^{2+}-doped ZnSe QDs. TEM images show that the particles are of spherical morphology with a small aggregation of particles, and the average particle size is 3–4 nm approximately. The HR-TEM image shows the lattice fringes of ZnSe crystal having the D-spacing of 0.13 nm, which are matched to (102) plane of ZnSe in the cubic phase. The energy-dispersive X-ray spectrum (EDX) confirms nucleation doping of Mn^{2+} ions as no Mn^{2+} related peaks are observed due to the deep implementation of Mn^{2+} ions in the ZnSe host, as shown in Fig. 3.2(e) and 3.2(f). The significant quantity of Zn and Se without

the other foreign elements confirms the purity and successful synthesis of the sample. The FFT (Fast Fourier Transform) image of the sample shown in Fig. 3.2d confirms the crystallinity of the as-prepared Mn^{2+}-doped ZnSe QDs. The TEM image and EDX of Mn@ZnSe QDs are also recorded in the presence of lead ions to understand the effect of these ions on the synthesized Mn@ZnSe QDs, as shown in Fig. 3.2c and 3.2(f), respectively. With the addition of Pb^{2+} ions, the TEM image shows the aggregation of the particles and the formation of some reduced size (PbSe) particles under the same imaging conditions. This can be visualized with the occurrence of Pb and Mn ion peaks in the EDX as PbSe particle formation with the displacement of some Mn ions.

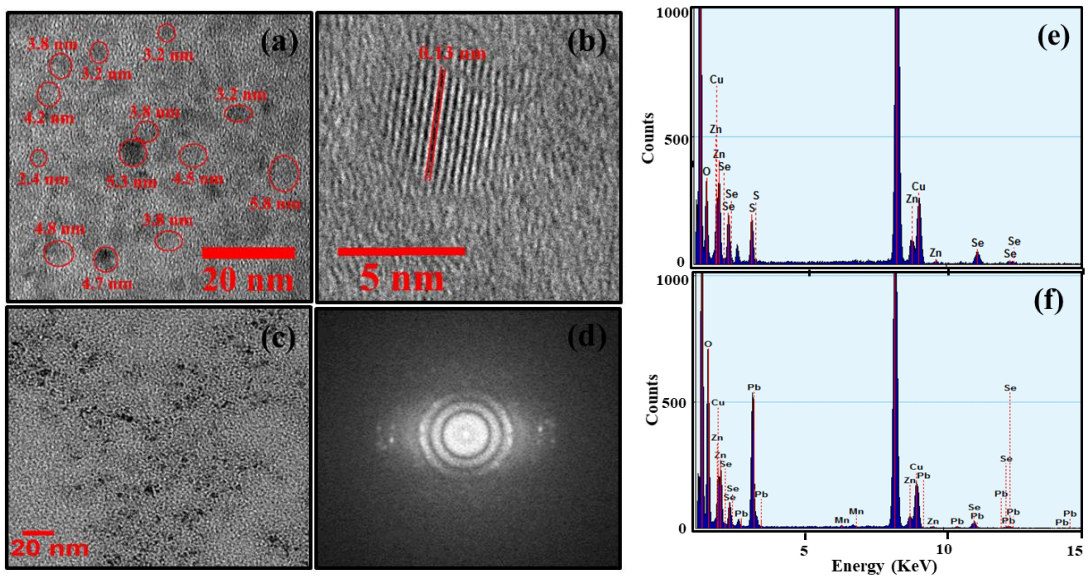

Figure 3.2. TEM (a) and HR-TEM (b) images of Mn@ZnSe QDs. TEM image of Mn@ZnSe QDs in the presence of [Pb^{2+}] ions (c) and FFT image (d). EDX spectra of bare Mn@ZnSe QDs (e) and with the addition of [Pb^{2+}] ions (f).

3.4.3. UV–Vis absorption spectrum

The absorption and PL excitation spectra of Mn@ZnSe QDs in water are shown in Fig. 3.3. The confinement band was appeared at around 320 nm, which was related to the band edge transition from the valence band to the conduction band. The high energy band at 320 nm is due to the highly confined QDs of 2–3 nm sizes. The excitation

spectrum shows a broad band with a maximum of around 350 nm. Thus, we can estimate the possible band gap for Mn@ZnSe QDs in water from absorbance and PL excitation lies in between the range 3.09–3.87 eV that signifies the quantum confinement of particles and reveals the reduction of particle size under identical experimental conditions. Compared with the bulk ZnSe (bandgap ~ 2.7 eV) [38], the fascinated bandgap of Mn@ZnSe QDs is quite large.

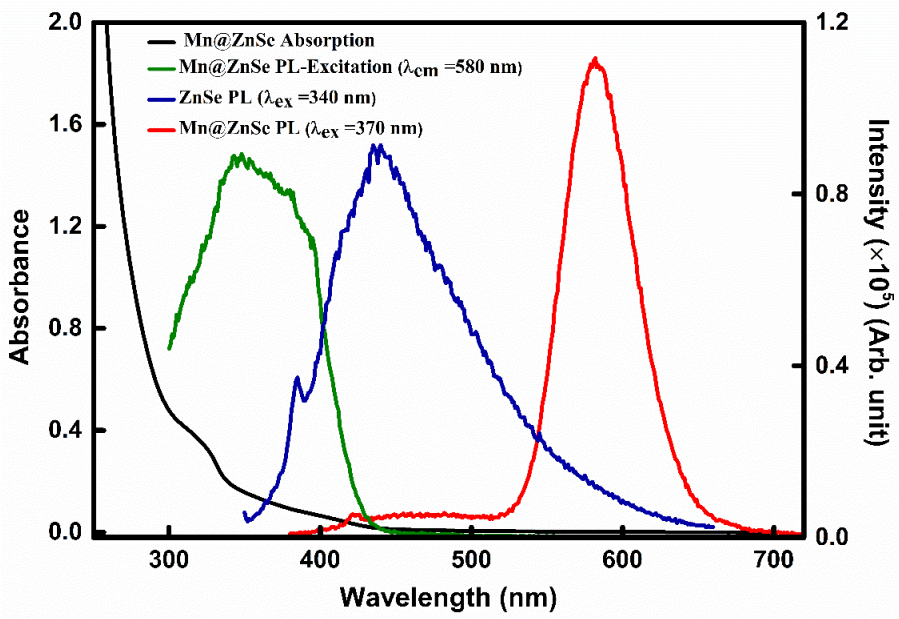

Figure 3.3. The PL spectra (Ex = 370 nm) of Mn^{2+}-doped and (Ex = 340 nm) un-doped ZnSe QDs along with the PL-excitation and absorption spectrum in water.

3.4.4. Photoluminescence spectral analysis

To achieve highly emissive colloidal nanoparticles in the direct aqueous medium, Mn@ZnSe QDs were prepared using the general "nucleation doping" strategy and without preferring the toxic organo-phosphines [39]. The PL spectra (λ_{ex} = 370 nm) of Mn@ZnSe QDs along with the un-doped ZnSe QDs are shown in Fig. 3.3. The undoped ZnSe QDs illustrate a small PL band at 380 nm and a broad peak at 435 nm related to water Raman and trap-states emission, respectively. The primary cause of these trap states in the aqueous ZnSe QDs are the point defects such as Frenkel (interstitial) defects

and the Schottky (vacancies) defects [40]. In the zinc blende structured ZnSe QDs, vacancy defects were dominant over the interstitials faults. Therefore, the broad PL peak possibly appears due to the recombination of electrons with Se vacancies (*i.e.*, holes), which are generated because of the lower Se/Zn ratio in the synthesis. Thus, the reason for relatively broad emission (FWHM = 105 nm) was the availability of many possible recombination paths, each with slightly different emission energy from the many trap-states. The PL spectrum of Mn^{2+}-doped ZnSe QDs shows a new band at 580 nm having FWHM of 60 nm beside the water Raman and trap-states emissions. The Mn^{2+} ions dopant produced visible (orange) PL as shown in the CIE plot (see Fig. 3.4) due to the recombination in Mn^{2+} ions following energy transfer in the ZnSe lattice, which has been attributed to the $^4T_1 \rightarrow {}^6A_1$ transition [41-44] as illustrated in Fig. 3.5.

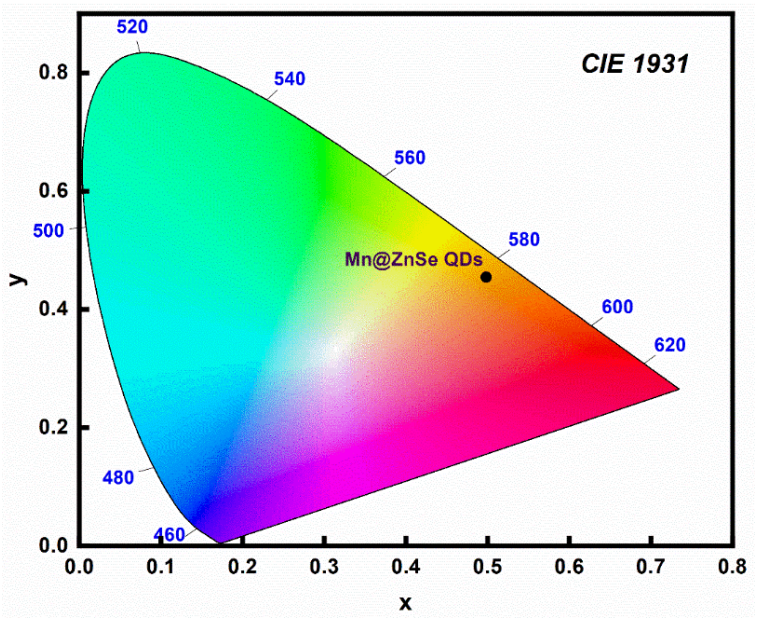

Figure 3.4. CIE 1931 plot corresponding to the PL spectra of Mn@ZnSe QDs.

According to Fang *et al.* [35], dopant emission is only observed when the dopant ions were incorporated into the lattice instead of attached to the outer surface. If the dopant is absorbed on the host's surface, the host emission decreased because the absorbed dopant ion acts as a surface trap that quenches the PL of the host [27]. The

occurrence of a new PL band and the enhancement of host ZnSe lattice emission shows the successful incorporation of Mn^{2+} in ZnSe lattice of Mn@ZnSe QDs.

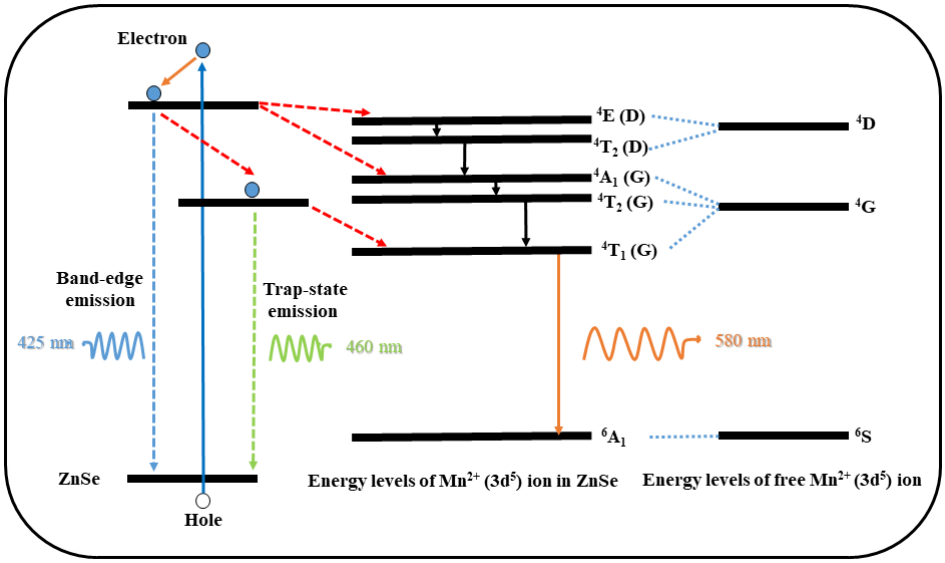

Figure 3.5. Schematic representation of various possible electronic transitions of Mn@ZnSe QDs, with ZnSe host and Mn^{2+} ion dopant energy levels.

3.4.5. Quantum yield (QY) calculations of Mn@ZnSe QDs

The quinine sulfate solution with a QY 54% was used to calibrate the spectrometer or considered a reference. First, the absorption spectra were recorded for both quinine sulphate solution and Mn@ZnSe quantum dots. The overlapping of both sample's absorption spectra gives a common point of absorbance where both the spectra crossed and noted that optical density (OD) at this point, which should not be higher than 0.1. In the next step, this crossed point wavelength (380 nm) was used as the excitation wavelength for both quinine sulfate and Mn@ZnSe samples. Then the PL spectra were recorded. The integral areas under the curves of both spectra were calculated and compared to obtain the QY of Mn@ZnSe quantum dots. The standard reference samples which have a known QY value is used for calculating the absolute values, according to the equation given below:

$$QY_D = QYr \times \left(\frac{I_D}{I_r}\right) \times \left(\frac{A_r}{A_D}\right) \times \left(\frac{n_D}{n_r}\right)^2 \quad (3.1)$$

QY_r and QY_D are the quantum yields of reference, *i.e.*, quinine sulfate (0.54) and the Mn@ZnSe QDs, respectively. A_D and A_r are the absorbances and I_D and I_r are corresponding integrated areas under the emission spectrum of QDs and the reference, respectively. n_r and n_D are the refractive indexes of the solvents used for reference and QDs, *i.e.*, sulfuric acid and distilled water, respectively. The calculated value of QY from the above equation comes out to be 17.3%.

3.4.6. Effect of UV irradiation on Mn@ZnSe QDs

The direct aqueous route has some drawbacks, such as the prepared QDs via aqueous route shows weak PL quantum yield and low stability. Because of the high surface area to volume ratio and high surface energy, the surface of QDs is very active; thus, in the presence of air, light and heat, there was a high aggregation possibility of the dots in water, which cause the reduced PL quantum yield. Numerous methods have been used to enhance the stability, biocompatibility and PL efficiency of the QDs. These methods include ultrasonic irradiation, doping transition metals, photoirradiation (photoactivation) and inorganic passivation [45-49]. The rise in PL quantum yield on exposure to UV radiation is generally called ‘‘photoactivation’’ and is also recognized as photo-brightening or photo-enhancement. Based on the previous reports [50], there are four major principal pathways for the photobrightening phenomenon, i.e., photoactivation due to heat-induction by light (photo-annealing), photoactivation due to adsorption of water molecules on the surface of QDs, photoactivation due to stabilization with surfactant molecules or surface-ligand passivation and photoactivation due to photo-oxidation. We used the photoactivation method for surface passivation of QDs and to enhance the PL properties.

The low PL QY of QDs might be due to the occurrence of intrinsic imperfections and surface dangling bonds, the Zn^{2+} vacancies combined with these surface defects in

the zinc blende structure of ZnSe. To reduce the surface defects, the photoactivation method was performed with the irradiation of ultra-violet radiation on the freshly synthesized Mn@ZnSe QDs. According to the observations, the photoactivation method enhances the excitonic emission/PL by reducing the surface imperfections. To promote the reduction of sulphur ions from the thiol group (–HS) of MPA capping agent, an ultra-violet (UV) lamp of 8W has been used for 90–120 min. Under UV radiation, the dissociated sulphur ions (S^{-}) bind to the Zn^{2+} vacancies and reduces surface defects. And observed a reduction in the PL related to the surface-defect states and an increase in PL related to Mn^{2+} ions. According to Silva *et al.* (2016), extended exposure of samples under UV irradiation causes the weakening of the QDs and reducing the PL intensity due to the complete reduction of capping/stabilizing agent shell [51]. We noted that the colloidal QDs persisted stability in water up to 120 min of high-intensity UV light irradiation, as shown in Fig. 3.6.

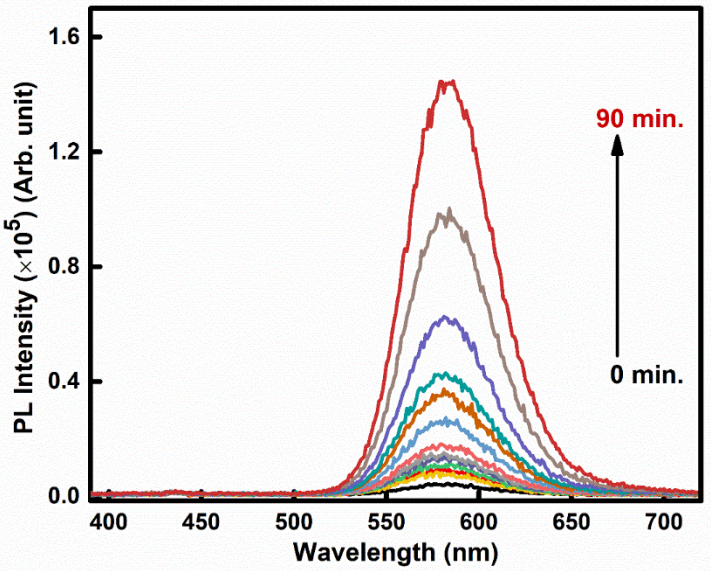

Figure 3.6. PL spectra of synthesized Mn@ZnSe QDs under UV irradiation (the effect of photoactivation) with time.

It was well accepted that the stability of QDs in an aqueous medium is lower than in the non-polar solvents. The reason for the lower photostability of QDs in

aqueous media is the involvement of O_2 and H_2O in the reaction mechanism of photodegradation or photocorrosion. It is also important to note that the photoactivation process, when carried out under high-intensity radiation (UV irradiation), leads to the photodecomposition or photochemical instability of the QDs.

The stability of Mn@ZnSe QDs under the persistent exposure to UV light or the extension of the photoactivation effect was also studied, as shown in Fig. 3.7. For this study, the previously prepared, filtered and room temperature stored Mn@ZnSe QDs were used rather than the freshly prepared QDs. The result shows an increase in the intensity of Mn-related emission with exposure to UV radiation and reached at the saturation point, i.e., after that, there is no further increase in the PL intensity.

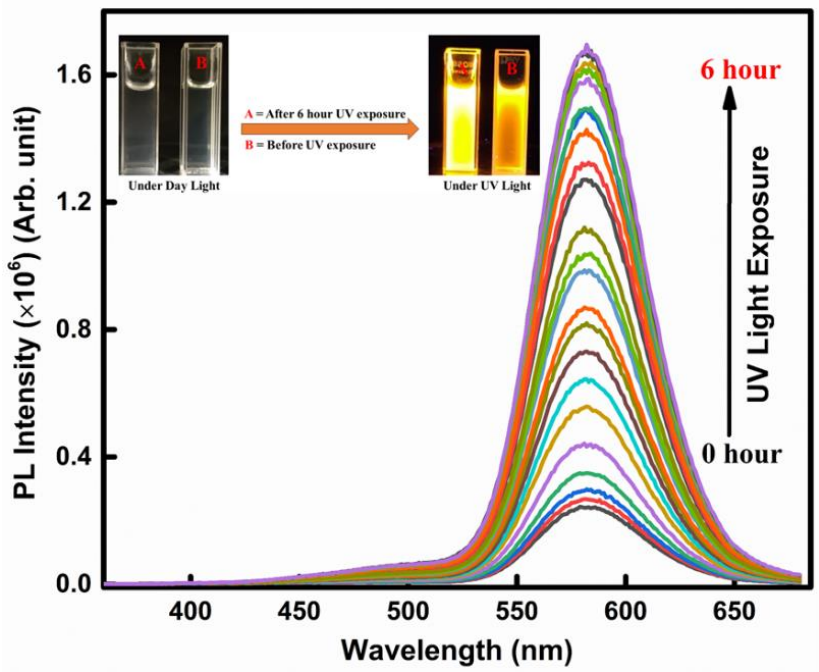

Figure 3.7. Stability of Mn@ZnSe QDs with the persistent exposure to UV light and extension of photo-activation effect.

3.5. Metal ion sensing

3.5.1. Effect of Pb^{2+} ions on the absorption and PL of Mn@ZnSe QDs

The experiments were performed with freshly prepared QDs before each experiment and diluted in 10 mL distilled (ultra-pure) water. The absorption and PL measurements

of QDs were carried out within 5 min after the mixing with metal ion solutions, as each measurement takes 1–2 min. Upon adding the metal ion [Pb^{2+}], a substantial increase in the absorbance and decrease in the PL intensity of Mn@ZnSe QDs has been observed. The PL spectra of Mn@ZnSe QDs in the absence and presence of various concentrations of metal ions observed under excitation at 370 nm along with the change in absorption spectra are shown in Fig. 3.8(a,b).

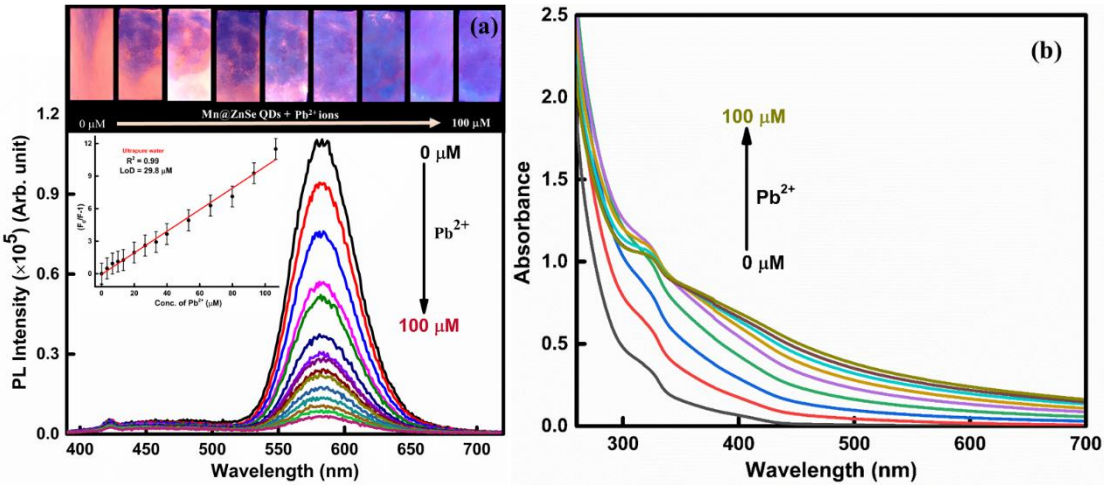

Figure 3.8. The PL spectra of Mn@ZnSe QDs (λ_{ex} = 370 nm) in ultrapure water with the addition of varying concentrations of [Pb^{2+}] ions (a) and the corresponding Stern-Volmer plot (inset of Fig. 3.8a). On the top of (a), the appeared image of the test strips coated with Mn@ZnSe QDs under a 365 nm UV lamp in the presence of different concentrations of Pb^{2+} ion. The absorption spectra of Mn@ZnSe QDs in water with the addition of different concentrations of [Pb^{2+}] ions (b).

The apparent change in PL of the prepared Mn@ZnSe QDs solution was observed by adding lead ions (0–100 μM). The PL intensity of synthesized Mn@ZnSe QDs was quenched gradually with the addition of Pb^{2+} ions. A strong quenching occurs without changing shape and the band position of PL, even remains unaltered at the concentration of 100 μM, indicating that there is no additional transition from the Mn@ZnSe QDs, which makes the system simple and applicable.

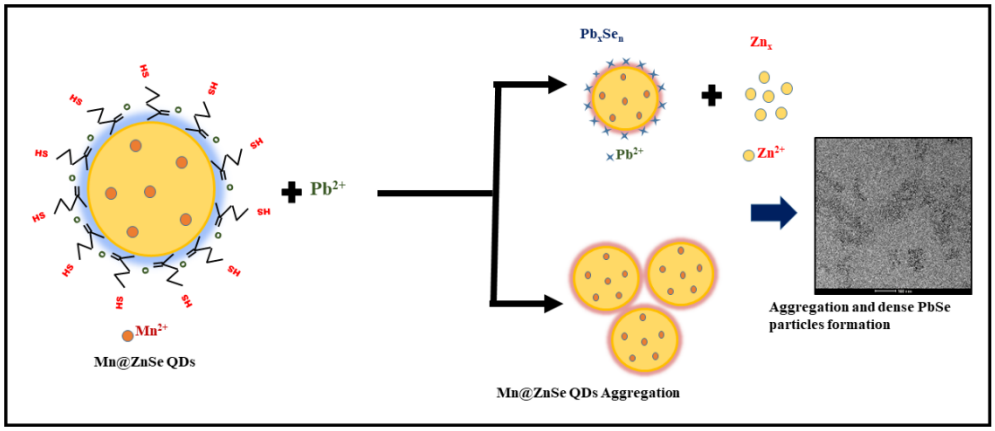

Figure 3.9. Schematic of the sensing mechanism for [Pb^{2+}] ions in water using Mn@ZnSe QDs as a sensing probe.

The Pb^{2+} ions react and formed the isolated or aggregated PbSe particles by displacing the Zn^{2+} ions because low solubility products are always preferred in the solution [52-54] that quench the PL of QDs by assisting non-radiative annihilation of charge carries, as shown in Fig. 3.9. Meanwhile, the color of the solution changes from transparent to light yellowish due to the attachment of Pb^{2+} ions with MPA ligand and the formation of a PbSe low solubility product.

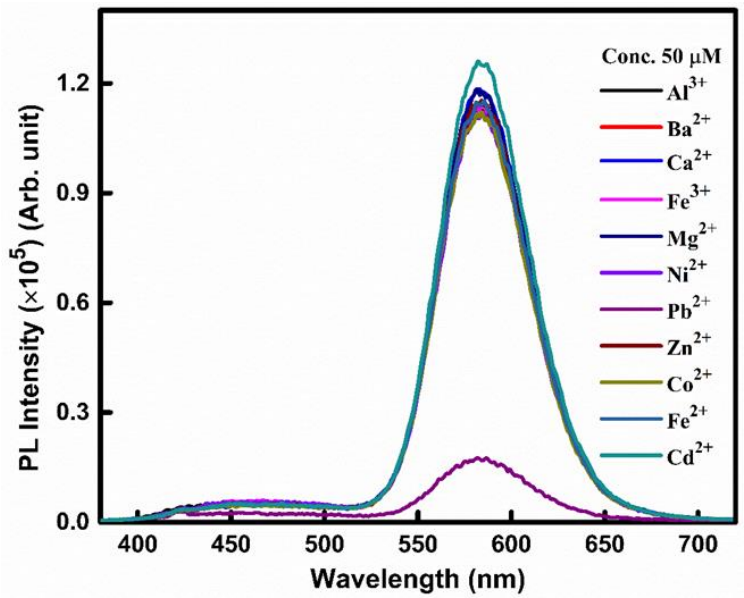

Figure 3.10. PL spectra of Mn@ZnSe QDs in the presence of a fixed concentration (50 µM) of various metal ions showing selective sensing for [Pb^{2+}].

To test the selective response of Mn@ZnSe QDs towards Pb^{2+} ions, which is important for practical applications, the PL spectra of QDs were recorded in the presence of 11 different metal ions, *i.e.*, Pb^{2+}, Cd^{2+}, Fe^{2+}, Fe^{3+}, Co^{2+}, Mg^{2+}, Al^{3+}, Ni^{2+}, Zn^{2+}, Cr^{2+} and Ca^{2+} (see Fig. 3.10). The PL intensity of Mn@ZnSe QDs in the presence of various metal ions is demonstrated by the bar diagram in Fig. 3.11(a). Thus, the MPA-capped Mn@ZnSe QDs did not show any significant response with other metal ions. It is also essential to investigate the interference effect of different metal ions for Mn@ZnSe QDs to be useful as sensing probes for Pb^{2+} ions. Then the PL spectra of Mn@ZnSe QDs are recorded in the presence of Pb^{2+} ions along with other metal ions and the obtained results are shown by the bar diagram in Fig. 3.11(b).

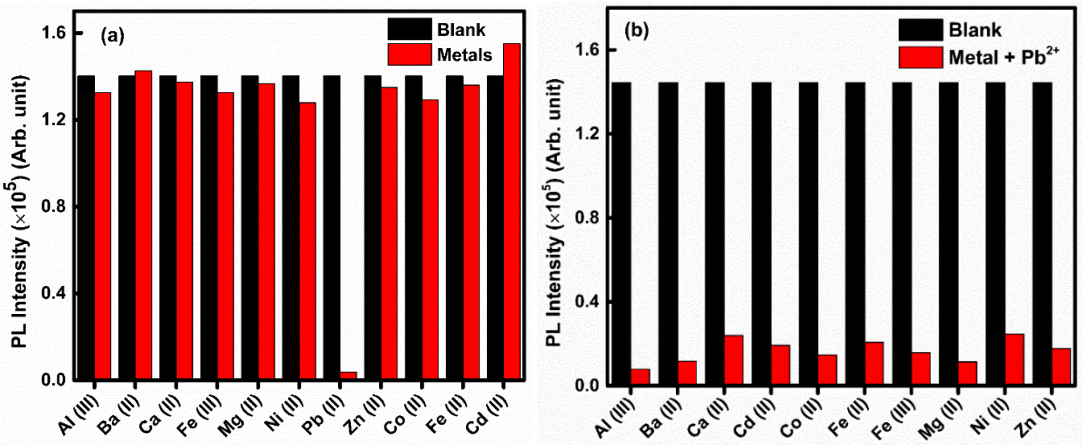

Figure 3.11. Bar diagram of PL intensity quenching of Mn@ZnSe QDs in the presence of various metal ions (a) and with a fixed concentration (100 µM) of [Pb^{2+}] in the presence of different metal ions (b).

The PL of QDs is entirely quenched by the addition of Pb^{2+} ions even in the presence of other foreign metal ions, which specifies that the presence of other metal ions in the probe solution does not affect the interaction between lead ions with the surface thiol ligands and shows the anti-interference effect.

3.5.2. Effect of Pb^{2+} ions on the lifetime of Mn@ZnSe QDs

Fig. 3.12 shows the PL decay profiles of Mn^{2+}-doped ZnSe QDs in the absence and the presence of a different concentration (0–100 µM) of Pb^{2+} ions dissolved in water. The excitation wavelength was 370 nm and decay was recorded up to 10 ms at monitoring the PL wavelength at 580 nm.

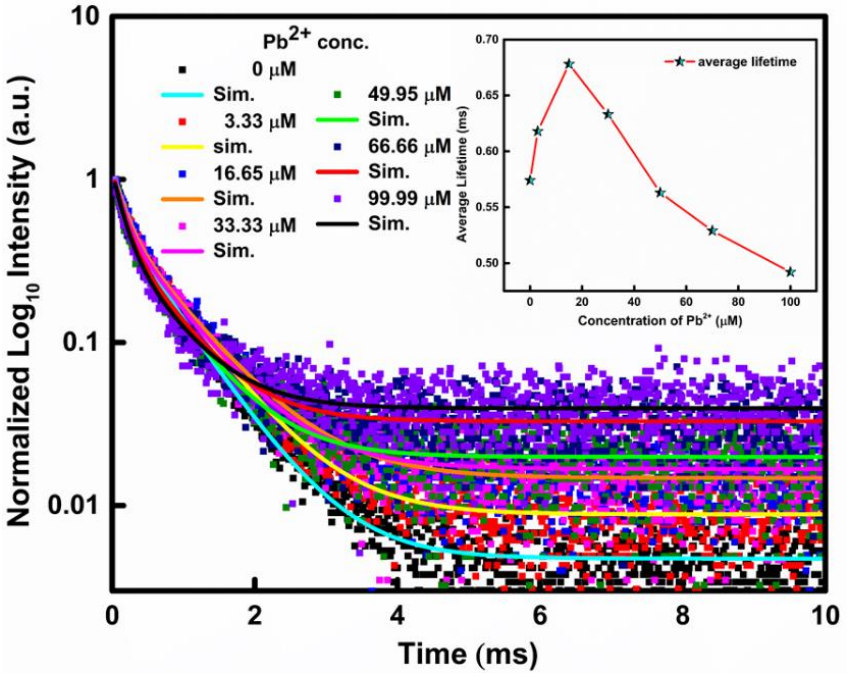

Figure 3.12. Fitted PL decay profiles of Mn@ZnSe QDs in the presence of different concentrations of [Pb^{2+}]. The excitation and PL wavelengths were 370 nm and 580 nm, respectively.

The obtained results could not have fitted with a single exponential and are fitted well with bi-exponential function by using the equation:

$$f(t) = \alpha_1 \exp\left(-\frac{t}{\tau_1}\right) + \alpha_2 \exp\left(-\frac{t}{\tau_2}\right), \quad (3.2)$$

Where τ_1 and τ_2 are the lifetime components and α_1 and α_2 are corresponding amplitudes [55]. The obtained lifetime and corresponding amplitudes together with average lifetime <τ> of Mn@ZnSe QDs with an increasing concentration of [Pb^{2+}] ions are listed in Table 3.1. The average lifetime was calculated by employing the equation:

$$< \tau > = \frac{\alpha_1 \tau_1^2 + \alpha_2 \tau_2^2}{\alpha_1 \tau_1 + \alpha_2 \tau_2}, \quad (3.3)$$

The average lifetime of Mn@ZnSe QDs increase**s** at the initial concentration (0–15 μM) of [Pb^{2+}] ions. Whereas decreases after that from 0.678 to 0.492 ms for the Pb^{2+} ion concentrations of 30–100 μM, as shown in the inset of Fig. 3.12.

Table 3.1. The lifetimes and pre-exponential factors of Mn@ZnSe QDs with different concentrations of [Pb^{2+}]. Excitation and PL wavelengths were 370 nm 580 nm, respectively.

(Mn@ZnSe)/Pb^{2+} (μM)	**τ_1 (ms)**	**τ_2 (ms)**	**α_1**	**α_2**	**τ_{av} (ms)**	**τ_{mean} (ms)**
0	0.195 ± 0.003	0.687 ± 0.007	0.51	0.49	0.574	0.441
3	0.157 ± 0.003	0.730 ± 0.007	0.53	0.47	0.618	0.443
15	0.176 ± 0.006	0.803 ± 0.010	0.53	0.47	0.678	0.489
30	0.140 ± 0.004	0.735 ± 0.010	0.52	0.48	0.633	0.437
50	0.129 ± 0.006	0.670 ± 0.010	0.56	0.44	0.563	0.399
70	0.138 ± 0.007	0.637 ± 0.020	0.56	0.44	0.529	0.387
100	0.156 ± 0.01	0.629 ± 0.030	0.62	0.38	0.492	0.392

The bi-exponential lifetimes of Mn@ZnSe QDs are associated with the Mn transitions populated via the excitation energy transfer from ZnSe and its defect/trap states. To

explore the excitation dynamics of QDs, the ps-fs time resolution is required and will be investigated.

3.5.3. Promising quenching mechanism

The quenching of PL in the presence of a quencher is either by static or dynamic interaction [56]. By the addition of Pb^{2+} ions, the PL of Mn@ZnSe QDs is remarkably quenched. The observed PL quenching follows a linear Stern-Volmer (S-V) relationship according to the equation:

$$\frac{F_0}{F} = 1 + K_D\,[C]\,, \tag{3.4}$$

Where F_0 and F are PL intensity of Mn@ZnSe QDs with and without the quenchers [Pb^{2+}], K_D is the S-V constant and *C* represents the molar concentration of [Pb^{2+}]. The relationship between relative PL intensity (F_0/F-1) of QDs and the concentrations of quencher [Pb^{2+}] is illustrated in the inset of Fig. 3.8(a). From the linear S-V plot, the calculated K_D value is 0.99×10^5 L mol^{-1}, and the limit of detection (LoD) is estimated using formula 3σ/K, comes out to be 29.8×10^{-6} mol L^{-1} for [Pb^{2+}]. Where K denotes the slope of the S-V plot and σ denotes the standard deviation. Furthermore, the quenching rate constant K_q, calculated by Eq. 5, was obtained to be 4.98×10^{10} L mol^{-1} s^{-1}.

$$K_D = K_q.\tau_0 \tag{3.5}$$

where τ_0 denotes the lifetime of Mn@ZnSe QDs in the absence of quencher. The maximum value of K_q for static collisional quenching is about 1-2 $\times 10^{10}$ L mol^{-1} s^{-1} [57]. The calculated value of K_q is higher than the maximum value indicating that the quenching is caused by a dynamic or collision in the excited state rather than the static due to complex formation in the ground state [58]. To further understand the mechanism of PL quenching by [Pb^{2+}] ions, the change in average lifetime provides us

with a clear thought. The corresponding fall in PL intensity and an average lifetime with increasing concentration of [Pb^{2+}] ions demonstrate an essential characteristic of dynamic quenching. The decrease in a lifetime and the PL intensity arises due to dynamic quenching, which is an additional rate process that aids the depopulation of excited states without radiative emission. The possible reason of an initial increase in the average lifetime of QDs with Pb^{2+} concentration (0–15 µM) is the formation of PbSe centers that induced geometrical distortions and decrease the overall non-radiative decay rate, and with increasing higher concentrations, the collisional rate increases that depopulate the excited states and thus observed a decrease in the lifetime with the further increase of Pb^{2+} ions [59].

3.5.4. Real samples detection and idea for device fabrication

The potential use of the Mn@ZnSe QDs for sensing Pb^{2+} ions in direct tap water and the Yamuna river water samples is further validated. The Yamuna river is the second largest affluent or tributary river of the holy Ganga river. Most of the rivers are not polluted near their origins in India. As the Yamuna river is getting polluted almost in Delhi by the pesticides, fertilizers, discharge of industrial effluents, and domestic sewage, that's why we used the Yamuna river water as a real sample analysis. For the experiment, 2 mL of Mn@ZnSe QDs was diluted to 10 mL by using the direct tap and Yamuna water and 3 mL of the diluted solution was used in a quartz cuvette (10 mm × 10 mm) for PL measurements.

The PL quenching was studied in tap and Yamuna river water in the presence of an ionic mixture of ten metal ions, with each metal having a concentration of 100 µM by dissolving all metals in tap water. Then added the concentration of Pb^{2+} metal ions according to the experimental procedure from 3.33 µM to 100 µM and recorded

the corresponding PL spectrum, as shown in Fig. 3.13(a,b), along with the corresponding S–V plots (inset).

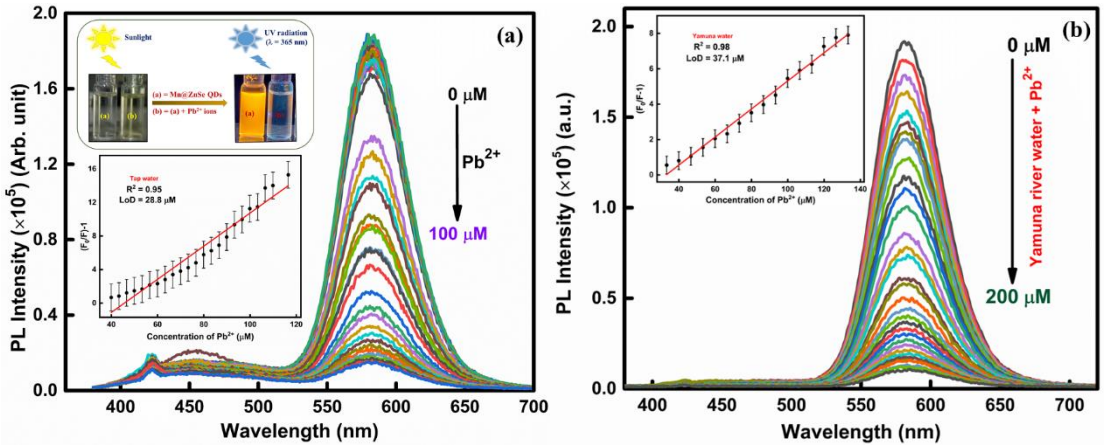

Figure 3.13. The PL spectra of Mn@ZnSe QDs (λ_{ex} = 370 nm) in tap water in the presence of varying concentrations of [Pb^{2+}] ions (a). The corresponding Stern-Volmer plot (bottom inset) and photographic representation of Mn@ZnSe QDs with and without the Pb^{2+} ions (PL turn-off) under UV radiation (top inset) are shown in the inset of (a). The PL spectra of Mn@ZnSe QDs (λ_{ex} = 370 nm) in Yamuna river water in the presence of varying concentrations of [Pb^{2+}] ions and corresponding Stern-Volmer plot are shown in (b) and inset of (b), respectively.

Table 3.2. Results of determination of Pb^{2+} ions in ultrapure water and real water samples.

Sample	LoD (μM)	Linearity range	R^2
Ultrapure water	29.8	0-100 μM	0.99
Tap water	28.8	40-110 μM	0.95
Yamuna river water	37.1	20-120 μM	0.98

The results of PL quenching as tabulated in Table 3.2 signify that the developed system was suitable for Pb^{2+} sensing in drinking water samples with high sensitivity. The photographic representation of Mn@ZnSe QDs sensor with and without the Pb^{2+} ions under the sunlight and UV radiation (λ= 365 nm) is shown in the inset of Fig. 3.11a.

Also, the effect of the presence of an excess amount of capping ligands MPA and TGA were recorded and presented in Fig. 3.14. The result shows a small increase in PL intensity with the initial volume of MPA and decreased with TGA. After that, for excess amounts, saturation was achieved.

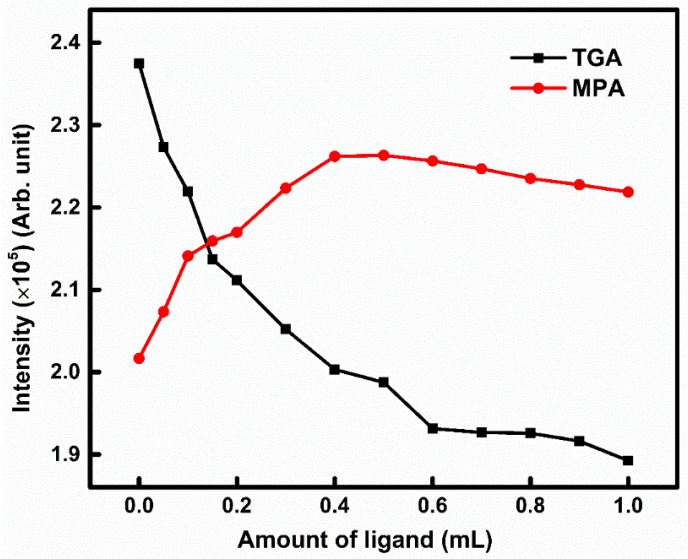

Figure 3.14. Stability of Mn@ZnSe QDs with the addition of an excess amount of MPA and TGA ligands.

A schematic representation of the test strip (filter paper) fabricated Mn@ZnSe QDs sensing probe for Pb^{2+} ions, as illustrated in the top of Fig. 3.7a. The Whatman filter papers were used as a substrate/test trip or base for the Mn@ZnSe QDs because the paper consists of cellulose fiber, which provides a great supporting or binding substrate. A 10 mm × 30 mm rectangular filter paper substrate was used after washing 2–3 times with ultrapure water and dipped in a concentrated 5 mL solution of Mn@ZnSe QDs for 30 min. under the mild heating conditions of 60 °C temperature. The QDs are absorbed and binds to the filter paper substrate and show good PL efficiency when excited under the UV lamp having the radiation of wavelength 365 nm. The PL quenching was studied in the presence of a different concentration of Pb^{2+} metal ions added uniformly throughout the paper substrate by using a micropipette of range 1–200 μL. The digital

pictures taken at different increasing concentrations of Pb^{2+} metal ions show the quenching in PL of deposited Mn@ZnSe QDs. This demonstrates that the prepared Mn@ZnSe QDs system could be promising for sensing device fabrication. A comparison of different reported sensors for Pb^{2+} and other metal ions using different QDs probes are represented in the tabular form in Table 3.3.

Table 3.3. Comparison of different reported sensors for Pb and other metal ions detection.

QDs	Capping agents	Ions	Method	References
Mn@ZnSe	3-Mercaptopropionic acid (MPA)	Pb^{2+}	Fluorescence and lifetime	this work
ZnSe	L-glutathione	Hg^{2+}	Fluorescence	60
ZnS:Mn/ZnS	Iminodiacetic acid (IDA)	Ag^{+}	Fluorescence	61
ZnS:Ce	Unmodified	Hg^{2+}	Fluorescence	62
CdTe	Mercaptoacetic acid (MAA)	Cu^{2+}	Fluorescence	63
CdTe	Thioglycolic acid (TGA)	Pb^{2+}	Fluorescence	64
CdSe/CdS	Dithizone (Dz)	Pb^{2+}	Fluorescence	65

3.6. Conclusions

In conclusion, the non-toxic direct aqueous route synthesized MPA-capped Mn@ZnSe QDs having ~17.3% QY are demonstrated selective PL quenching in the presence of Pb^{2+} ions. The PL intensity was quenched up to 98% with the addition of 100 µM of Pb^{2+}. The results indicated that the prepared QDs could sense Pb^{2+} ions in ultrapure water, real water samples (tap and Yamuna river water) and even in the presence of an ionic mixture without the interference of other metal ions. The detection limits calculated with the help of the linear S-V plot at room temperature for Pb^{2+} ions are 29.8, 28.8 and 37.1 µM in ultrapure, tap water and the Yamuna river water, respectively. Steady-state and PL lifetime accomplished dynamic interaction between the quenchers

and QDs as the possible mechanism of PL quenching. The QY and CIE plot exhibit that the material is essential for the orange QLEDs.

References

[1] Y. Jang, A. Shapiro, M. Isarov, A. Rubin-Brusilovski, A. Safran, A.K. Budniak, F. Horani, J. Dehnel, A. Sashchiuk, E. Lifshitz, Interface control of electronic and optical properties in IV-VI and II-VI core/shell colloidal quantum dots: a review, Chem. Commun. 53 (2017) 1002–1024.

[2] S. Xiong, S. Huang, A. Tang, F. Teng, Synthesis and luminescence properties of water-dispersible ZnSe nanocrystals, Mater. Lett. 61 (2007) 5091–5094.

[3] I.M.R. Moura, P.E.C. Filho, M.A.B.L. Seabra, G. Pereira, G.A.L. Pereira, A. Fontes, B.S. Santos, Highly fluorescent positively charged ZnSe quantum dots for bioimaging, J. Lumin. 201 (2018) 284–289.

[4] I.A. Mir, H. Alam, E. Priyadarshini, R. Meena, K. Rawat, P. Rajamani, M.S. Rizvi, H.B. Bohidar, Antimicrobial and biocompatibility of highly fluorescent ZnSe core and ZnSe@ZnS core-shell quantum dots, J. Nanopart. Res. 20 (2018) 174-184.

[5] N. De Acha, C. Elosúa, J.M. Corres, F.J. Arregui, Fluorescent sensors for the detection of heavy metal ions in aqueous media, Sensors 19 (2019) 599-632.

[6] H. Li, Y. Li, Z. Zhang, X. Pang, X. Yu, Highly selective luminescent sensing of Cu^{2+} in aqueous solution based on a Eu(III)-centered periodic mesoporous organosilicas hybrid, Mater. Des. 172 (2019) 107712-107720.

[7] Y. Gao, X. Pan, S. Xu, Z. Liu, J. Wang, K. Yu, C. Wang, H. Yuan, S. Wu, Fluorescence-enhanced microfluidic sensor for highly sensitive in-situ detection of copper ions in lubricating oil, Mater. Des. 191 (2020) 108693-108701.

[8] X. Cheng, Y. Yu, Y. Jia, L. Duan, Fluorescent PU films for detection and removal of Hg^{2+}, Cr^{3+} and Fe^{3+} ions, Mater. Des. 95 (2016) 133–140.

[9] M.K. Singh, M.S. Mehata, Phase-dependent optical and photocatalytic performance of synthesized titanium dioxide (TiO_2) nanoparticles, Optik. 193 (2019) 163011-163021.

[10] M.S. Mehata, Enhancement of charge transfer and quenching of photoluminescence of capped CdS quantum dots, Sci. Rep. 5 (2015) 12056.

[11] M.S. Mehata, R.K. Ratnesh, Luminescence properties and exciton dynamics of core-multi-shell semiconductor quantum dots leading to QLEDs, Dalton Trans. 48 (2019) 7619–7631.

[12] B. Li, Z. Zhang, J. Qi, N. Zhou, S. Qin, J. Choo, L. Chen, Quantum dot-based molecularly imprinted polymers on three-dimensional origami paper microfluidic chip for fluorescence detection of phycocyanin, ACS Sens. 2 (2017) 243–250.

[13] Y. N. Raoa, A. Dattaa, S. K. Dasb, A. Saha, Irradiation route to aqueous synthesis of highly luminescent ZnSe quantum dots and its function as a copper ion fluorescence sensor, Mater. Res. Bull. 80 (2016) 280–287.

[14] S. Shena, M. Jiaa, Z. Tanga, S. Changa, P. Shia, J. Yanga,b, Preparation and application of Mn-doped $Zn_{0.5}Cd_{0.5}S$@ZnS nanorods with high quantum yield as sensitive fluorescence probe for detection of glucose, Mater. Res. Bull. 106 (2018) 471–477.

[15] P. Sharma, M. S. Mehata, Rapid sensing of lead metal ions in an aqueous medium by MoS_2 quantum dots fluorescence turn-off, Mater. Res. Bull 131 (2020) 110978.

[16] J. Ke, X. Li, Q. Zhao, Y. Hou, J. Chen, Ultrasensitive quantum dot fluorescence

quenching assay for selective detection of mercury ions in drinking water, Sci. Rep. 4 (2014) 5624.

[17] L.A. Malik, A. Bashir, A. Qureashi, A.H. Pandith, Detection and removal of heavy metal ions: a review, Environ. Chem. Lett. 17 (2019) 1495–1521.

[18] D. Wu, Z. Chen, G. Huang, X. Liu, ZnSe quantum dots based fluorescence sensors for Cu^{2+} ions, Sens. Actuators A Phys. 205 (2014) 72–78.

[19] P. Sharma, M.S. Mehata, Colloidal MoS_2 quantum dots based optical sensor for detection of 2,4,6-TNP explosive in an aqueous medium, Opt. Mater. 100 (2020) 109646.

[20] Y. Jiao, D. Yu, Z. Wang, K. Tang, X. Sun, Synthesis , nonlinear optical properties and photoluminescence of ZnSe quantum dots in stable solutions, Mater. Lett. 61 (2007) 1541–1543.

[21] A. Zuber, M. Purdey, E. Schartner, C. Forbes, B. Van Der Hoek, D. Giles, A. Abell, T. Monro, H. Ebendorff-Heidepriem, Detection of gold nanoparticles with different sizes using absorption and fluorescence based method, Sens. Actuators B Chem. 227 (2016) 117–127.

[22] Y.K. Yang, K.J. Yook, J. Tae, A rhodamine-based fluorescent and colorimetric chemodosimeter for the rapid detection of Hg^{2+} ions in aqueous media, J. Am. Chem. Soc. 127 (2005) 16760–16761.

[23] H. Zheng, Z.H. Qian, L. Xu, F.F. Yuan, L.D. Lan, J.G. Xu, Switching the recognition preference of rhodamine B spirolactam by replacing one atom: design of rhodamine B thiohydrazide for recognition of Hg(II) in aqueous solution, Org. Lett. 8 (2006) 859–861.

[24] M.B. Gumpu, S. Sethuraman, U.M. Krishnan, J.B.B. Rayappan, A review on detection of heavy metal ions in water - An electrochemical approach, Sens.

Actuators B Chem. 213 (2015) 515–533.

[25] A. Çelik, Ü. Çömelekoğlu, S. Yalin, A study on the investigation of cadmium chloride genotoxicity in rat bone marrow using micronucleus test and chromosome aberration analysis, Toxicol. Ind. Health. 21 (2005) 243–248.

[26] A.M. Derfus, W.C.W. Chan, S.N. Bhatia, Probing the cytotoxicity of semiconductor quantum dots, Nano Lett. 4 (2004) 11–18.

[27] N. Pradhan, D.M. Battaglia, Y. Liu, X. Peng, Efficient, stable, small, and water-soluble doped ZnSe nanocrystal emitters as non-cadmium biomedical labels, Nano Lett. 7 (2007) 312–317.

[28] S.K. Hong, E. Kurtz, J.H. Chang, T. Hanada, M. Oku, T. Yao, Low stacking-fault density in ZnSe epilayers directly grown on epi-ready GaAs substrates without GaAs buffer layers, Appl. Phys. Lett. 78 (2001) 165–167.

[29] H. Jeon, J. Ding, W. Patterson, A. V. Nurmikko, W. Xie, D.C. Grillo, M. Kobayashi, R.L. Gunshor, Blue-green injection laser diodes in (Zn,Cd)Se/ZnSe quantum wells, Appl. Phys. Lett. 59 (1991) 3619–3621.

[30] S. Kundu, S. Maiti, D. Ghosh, C.N. Roy, A. Saha, Aqueous synthesis of protein-encapsulated ZnSe quantum dots and physical significance of semiconductor-induced Cu(II) ion sensing, ChemPhysChem 18 (2017) 2533–2540.

[31] J.K. Furdyna, Diluted magnetic semiconductors, J. Appl. Phys. 64 (1988) 26-64.

[32] R.N. Bhargava, D. Gallagher, X. Hong, A. Nurmikko, Optical properties of manganese-doped nanocrystals of ZnS, Phys. Rev. Lett. 72 (1994) 416–419.

[33] R. Subha, V. Nalla, J.H. Yu, S.W. Jun, K. Shin, T. Hyeon, C. Vijayan, W. Ji, Efficient photoluminescence of Mn^{2+}-doped ZnS quantum dots excited by two-photon absorption in near-infrared window II, J. Phys. Chem. C. 117 (2013) 20905–20911.

[34] N. Pradhan, X. Peng, Efficient and color-tunable Mn-doped ZnSe nanocrystal emitters : control of optical performance via greener synthetic chemistry, J. Am. Chem. Soc. 129 (2007) 3339–3347 .

[35] Z. Fang, P. Wu, X. Zhong, Y.-J. Yang, Synthesis of highly luminescent Mn:ZnSe/ZnS nanocrystals in aqueous media, Nanotechnology. 21 (2010) 305604-305612.

[36] Y. Nandan, M.S. Mehata, Wavefunction engineering of type-I/type-II excitons of CdSe/CdS core-shell quantum dots, Sci. Rep. 9 (2019) 2.

[37] V. Sharma, M.S. Mehata, Synthesis of photoactivated highly fluorescent Mn^{2+}-doped ZnSe quantum dots as effective lead sensor in drinking water, Mater. Res. Bull. 134 (2021) 111121.

[38] F. Qiao, R. Kang, Q. Liang, Y. Cai, J. Bian, X. Hou, Tunability in the optical and electronic properties of ZnSe microspheres via Ag and Mn doping, ACS Omega. 4 (2019) 12271–12277.

[39] R. Zeng, M. Rutherford, R. Xie, B. Zou, X. Peng, Synthesis of highly emissive Mn-Doped ZnSe nanocrystals without pyrophoric reagents, Chem. Mater. 22 (2010) 2107–2113.

[40] D. Denzler, M. Olschewski, K. Sattler, Luminescence studies of localized gap states in colloidal ZnS nanocrystals, J. Appl. Phys. 84 (1998) 2841–2845.

[41] S. Acharya, D.D. Sarma, N.R. Jana, N. Pradhan, An alternate route to high-quality ZnSe and Mn-doped ZnSe nanocrystals, J. Phys. Chem. Lett. 1 (2010) 485–488.

[42] C. Wang, X. Gao, Q. Ma, X. Su, Aqueous synthesis of mercaptopropionic acid capped Mn^{2+}-doped ZnSe quantum dots, J. Mater. Chem. 19 (2009) 7016–7022.

[43] C. Graf, A. Hofmann, T. Ackermann, C. Boeglin, R. Viswanatha, X. Peng, A.F.

Rodríguez, F. Nolting, E. Rühl, Magnetic and structural investigation of ZnSe semiconductor nanoparticles doped with isolated and core-concentrated Mn^{2+} ions, Adv. Funct. Mater. 19 (2009) 2501–2510.

[44] A. Hofmann, C. Graf, C. Boeglin, E. Rühl, Magnetic and structural investigation of Mn^{2+}-doped ZnSe semiconductor nanoparticles, ChemPhysChem. 8 (2007) 2008–2012.

[45] C. Luo, B. Li, H. Peng, X. Tang, Y. Wang, J. Travas-Sejdic, The effect of photo-irradiation on the optical properties of thiol-capped CdTe quantum dots, J. Nanosci. Nanotechnol. 12 (2012) 2998–3005.

[46] R. Saleh, N.F. Djaja, Transition-metal-doped ZnO nanoparticles: synthesis, characterization and photocatalytic activity under UV light, Spectrochim. Acta - Part A Mol. Biomol. Spectrosc. 130 (2014) 581–590.

[47] V. Krivenkov, A. Tretyachenko, P.S. Samokhvalov, A.A. Chistyakov, I. Nabiev, Controllable photo-brightening/photo-darkening of semiconductor quantum dots under laser irradiation, Nanophotonics VI. 9884 (2016) 1-6.

[48] S. Mathew, B.S. Bhardwaj, A.D. Saran, P. Radhakrishnan, V.P.N. Nampoori, C.P.G. Vallabhan, J.R. Bellare, Effect of ZnS shell on optical properties of CdSe-ZnS core-shell quantum dots, Opt. Mater. 39 (2015) 46–51.

[49] X. Wang, X. Kong, Y. Yu, Y. Sun, H. Zhang, Effect of annealing on upconversion luminescence of $ZnO:Er^{3+}$ nanocrystals and high thermal sensitivity, J. Phys. Chem. C. 111 (2007) 15119–15124.

[50] C. Carrillo, S. Cardenas, B.M. Simonet, M. Valcarcel, Quantum dots luminescence enhancement due to illumination with UV/Vis light, Chem. Commun. 35 (2009) 5214–5226.

[51] T.G. Silva, I.M.R. Moura, P.E.C. Filho, M.I.A. Pereira, C.A.A. Filho, G. Pereira,

G.A.L. Pereira, A. Fontes, B.S. Santos, ZnSe:Mn aqueous colloidal quantum dots for optical and biomedical applications, Phys. Status Solidi Curr. Top. Solid State Phys. 13 (2016) 530–533.

[52] E.M. Soliman, M.E. Mahmoud, S.A. Ahmed, Reactivity of thioglycolic acid physically and chemically bound to silica gel as new selective solid phase extractors for removal of heavy metal ions from natural water samples, Int. J. Environ. Anal. Chem. 82 (2002) 403–413.

[53] S.A. Elfeky, Facile sensor for heavy metals based on thiol-capped CdTe quantum dot, J. Environ. Anal. Chem. 05 (2018) 1–5.

[54] S. Parani, N. Tsolekile, B.M.M. May, K. Pandian, O. S. Oluwafemi, Mn-Doped ZnSe Quantum Dots as Fluorimetric Mercury Sensor. Intech. 13 (2002) 201-219.

[55] M.K. Singh, M.S. Mehata, Enhanced photoinduced catalytic activity of transition metal ions incorporated TiO_2 nanoparticles for degradation of organic dye: Absorption and photoluminescence spectroscopy, Opt. Mater. 109 (2020) 110309.

[56] L.K. Fraiji, D.M. Hayes, T.C. Werner, Static and dynamic fluorescence quenching experiments for the physical chemistry laboratory, J. Chem. Educ. 69 (1992) 424–428.

[57] M.E.K. Wahba, N. El-Enany, F. Belal, Application of the Stern-Volmer equation for studying the spectrofluorimetric quenching reaction of eosin with clindamycin hydrochloride in its pure form and pharmaceutical preparations, Anal. Methods. 7 (2015) 10445–10451.

[58] M.M. Dzagli, V. Canpean, M. Iosin, M.A. Mohou, S. Astilean, Study of the interaction between CdSe/ZnS core-shell quantum dots and bovine serum albumin by spectroscopic techniques, J. Photochem. Photobiol. A: Chem. 215

(2010) 118–122.

[59] L. Wang, R. Liu, Z. Chi, B. Yang, P. Zhang, M. Wang, Spectroscopic investigation on the toxic interactions of Ni^{2+} with bovine hemoglobin, Spectrochim. Acta - Part A Mol. Biomol. Spectrosc. 76 (2010) 155–160.

[60] Z.X. Cai, B.Q. Shi, L. Zhao, M.H. Ma, Ultrasensitive and rapid lead sensing in water based on environmental friendly and high luminescent L-glutathione-capped ZnSe quantum dots, Spectrochim. Acta - Part A Mol. Biomol. Spectrosc. 97 (2012) 909–914.

[61] B.H. Zhang, L. Qi, F.Y. Wu, Functionalized manganese-doped zinc sulfide core/shell quantum dots as selective fluorescent chemodosimeters for silver ion, Microchim. Acta 170 (2010) 147.

[62] H. Chu, D. Yao, J. Chen, M. Yu, L. Su, Double-emission ratiometric fluorescent sensors composed of rare-earth-doped ZnS quantum dots for Hg^{2+} detection, ACS Omega 5 (2020), 9558-9565.

[63] C. X. Guo, J.L. Wang, J. Cheng, Z.F. Dai, Determination of trace copper ions with ultrahigh sensitivity and selectivity utilizing CdTe quantum dots coupled with enzyme inhibition, Biosens. Bioelectron. 36 (2012) 69–74.

[64] J.Y. Xia, W.B. Xu., The application of TGA - CdTe quantum dots in fluorescent Probe, J. Synth. Cryst. 41 (2012) 193–199.

[65] Q. Zhao, X.L. Rong, H.B. Ma, G.H. Tao, Dithizone functionalized CdSe/CdS quantum dots as turn-on fluorescent probe for ultrasensitive detection of lead ion, J. Hazard. Mater. 250 (2013) 45–52.

Chapter 4

ZnSe quantum dots as an optical sensor for recognition of explosive 2,4,6-TNP traces

4.1. Introduction

Nitroaromatic compound**,** 2,4,6-trinitrophenol (2,4,6-TNP) or picric acid, is used worldwide in numerous industries to manufacture fireworks, military explosives, matches, pesticides, dyes and pigments [1–3]. 2,4,6-TNP has a higher explosive nature than the well-known 2,4,6-trinitrotoluene (2,4,6-TNT) because of its low safety coefficient and greater detonation velocity [4]. Also, picric acid has vast applications in forensic investigations and various industries like pharmaceutical, leather and dye due to high water solubility and its disposal. The explosive bomb blasts carried out by terrorist groups contain 2,4,6-TNP, leading to increased water and soil contamination. The nitroaromatic 2,4,6-TNP is also known for its haematotoxin and hepatotoxic effects, which lead to carcinogenesis and mutagenesis in the living cells [5]. Even a small intake of 2,4,6-TNP causes severe health damage to the nervous system, liver, kidneys, and eyes, leading to cancer in humans and wildlife animals [6,7]. Therefore, novel, reliable, rapid, efficient and economical analytical approaches are essential for on-site monitoring and detecting traces of nitroaromatic compounds, i.e., picric acid from the water medium. The different existing methods and techniques, such as mass spectroscopy, Raman spectroscopy, cyclic voltammetry, chromatographic technique, and gas chromatography for sensing explosives, are based on field sampling [8–10].

[*] *Content of this chapter have been published in* ***Spectrochimica Acta Part A: Molecular and Biomolecular Spectroscopy 260 (2021) 119937.***

However, for practical uses, these techniques have many drawbacks such as sophisticated instrumentation, higher time consumption, multistep synthesis processes, poor selectivity and less sensitivity. Therefore, there is a need to develop a new technique for fast and reliable recognition. In this regard, the fluorescence (emission) technique is one of the most suitable because of its low cost, easy operation, high sensitivity and selectivity [11,12]. So, a fluorescent sensing material having rapidness and good sensitivity with high fluorescence is exceptionally desirable. The semiconductors quantum dots (QDs) with high quantum efficiency are essential in fabricating fluorescence sensors. The photoluminescence (PL) of the semiconductor QDs is tunable with the variation of size and the introduction of dopant ions.

Most importantly, the nanoparticles/QDs allows the surface modification by various functional groups and recognize different receptors, allowing the detection selectivity to specific targets [13–18], including the other probes [19,20]. Therefore, the sensors centered on the QDs fluorescence have a notable benefit above the other old sensing schemes regarding detection selectivity and sensitivity. Although the fluorescent QDs applied sensors have been broadly studied, the non-toxic, direct aqueous synthesized high fluorescent semiconductor QDs with high sensitivity and selectivity to the specific analytes or targets have rarely been studied. It is well-known that ZnSe QDs are principally suitable for sensing applications because of their moderate bandgap (2.7 eV) and non-toxic nature. The fluorescent ZnSe QDs has emerged as a fascinating class of nanomaterial for superior photocatalysis like TiO_2 nanoparticle [20,21], drug delivery, biosensors, bioimaging, optoelectronics and chemo-sensors applications due to their ease of synthesis, desirable biocompatibility, large Stoke's shift, high aqueous solubility, tunable photoluminescence and low toxicity. 3-mercaptopropionic acid (MPA) capped QDs has several advantages over the

other capping agents. MPA provides a rich sulfur (S) source, excellent thermal stability and water solubility, which helps in increasing the PL quantum efficiency of the QDs. Herein, because of the above facts, the blue fluorescent ZnSe QDs were synthesized through a direct aqueous route at 70 ℃ and further applied to recognize 2,4,6-TNP in water through the sensitive and selective fluorescence turn-off method [22].

4.2. Experimental

4.2.1. Materials and Methods

All the precursors are of analytical grade and used without any purification. Zinc acetate dihydrate, 98% ($Zn(CH_3COO)_2.H_2O$) and 3-mercaptopropionic acid (MPA), 99% ($C_3H_6O_2S$,) were purchased from ACROS Organics. Selenium powder, 99.5% (Se) was purchased from Sigma Aldrich, Sodium borohydride, 95% ($NaBH_4$) was purchased from Central Drug House. Sodium hydroxide, 85% (NaOH) was purchased from RANKEM. The nitroaromatic compounds, i.e., 2,4,6-trinitrophenol (2,4,6-TNP), 2,6-dinitrotoluene (2,6-DNT), 1,2-dinitrobenzene (1,2-DNB), 2-nitrotoluene (2-NT), 4-nitrotoluene (4-NT) were purchased from Sigma Aldrich and Acetonitrile (ACN) was purchased from SRL Chem. The ultra-pure DI water was used as a solvent in the synthesis and all the experiments.

Caution: The explosive picric acid (2,4,6-TNP) should be handled and used cautiously and in small amounts.

4.2.2. Synthesis of ZnSe QDs

The stable and water-soluble blue fluorescent ZnSe QDs were synthesized using the previously reported direct aqueous route approach with minor modifications at 70 ℃ (below the water boiling point) with 3-mercaptopropionic acid (MPA) as a stabilizing and reducing agent [23]. In the typical procedure, a 250 mL three-neck round-bottomed vessel was loaded with 25 mL ultra-pure DI water with a pH value of 11.3, adjusted

using a 1M solution of NaOH and monitored with the help of a pH meter. Added an appropriate amount of zinc acetate and heated to 70 ℃ for 30 min. in the inert environment with the continuous flow of nitrogen gas. Separately, NaHSe stock solution was prepared in ultra-pure DI water by the reaction of sodium borohydride ($NaBH_4$) and selenium powder (Se) at room temperature. Then, transferred this freshly prepared stock solution of NaHSe to the 250 mL vessel containing zinc precursor and simultaneously added 0.5 mL MPA solution. After 30 min., the color of the product changes from transparent to yellowish, then turn off heating and collect the prepared raw ZnSe QDs. The prepared solution was precipitated using ethanol and washed with water by using a centrifuge. The filtered and washed ZnSe QDs were dried under vacuum at 60 ℃ and stored for further use.

4.2.3. Characterization tools

High-resolution transmission electron microscopy (HR-TEM) images were acquired by the TALOS instrument at a working accelerating voltage of 200 kV. The absorption studies were carried out by using the Lambda-750 dual-beam UV/VIS/NIR spectrometer (Perkin-Elmer), photoluminescence (PL) investigations were performed on Horiba Jobin Yvon, Fluorolog-3 spectrofluorometer equipped with 450 W xenon lamp and a photomultiplier tube (PMT). The PL decays were studied via DeltaFlex-01-DD, Horiba Jobin Yvon time-correlated single-photon counting system (TCSPC) equipped with PPD-850 detector and Delta diode (λ_{ex} = 340 nm) were used for the excitation.

4.3. Results and discussion

The synthesis includes the direct aqueous route with less toxic materials and relatively lower temperatures at 70 ℃ below the boiling point of water. Before applying the freshly prepared ZnSe QDs as an analytic probe for picric acid, some essential

characterizations were performed to confirm the successful synthesis. The structural analysis was done with the help of XRD and TEM characterization. The XRD pattern and TEM/HR-TEM images of synthesized ZnSe QDs are represented in Fig. 4.1.

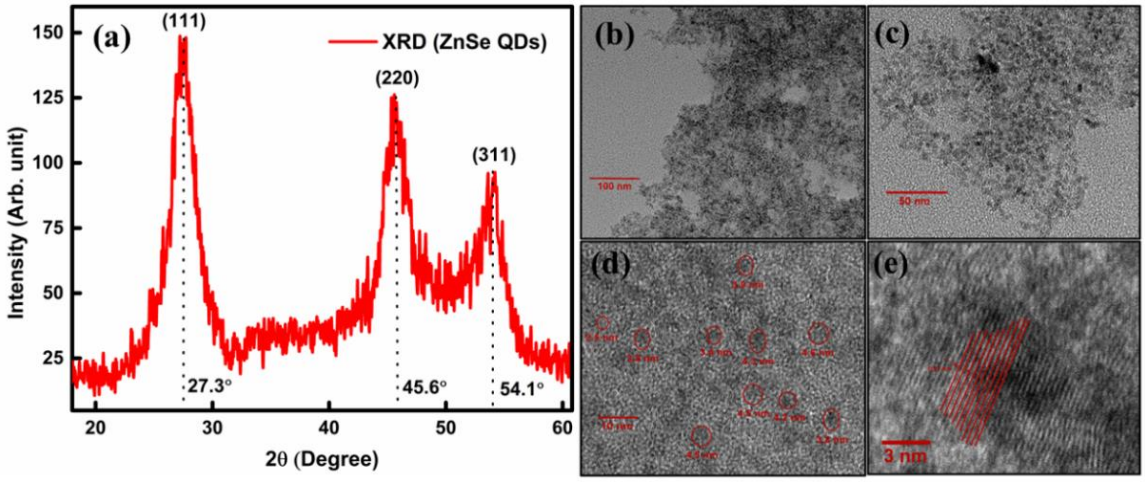

Figure 4.1. XRD pattern (a) and TEM and HR-TEM images (b-e) of MPA-protected ZnSe QDs.

Fig. 4.1a represented the XRD pattern of synthesized ZnSe QDs, in which the diffraction peaks are observed at diffraction angles 27.3°, 45.6° and 54.1° corresponding to the planes (111), (220) and (311), respectively. The strong diffraction peaks develop alone in the (111) crystal faces attribute to the zinc-blend structure of synthesized ZnSe QDs. Fig. 4.1b illustrates the highly dense formation of quantum dots, i.e., the large number of QDs are present in a small volume. Fig. 4.1c and d shows the uniform and spherical morphology with a 3 to 5 nm size range. Fig. 4.1e illustrates the formation of crystalline ZnSe QDs with the lattice d-spacing to be 0.2 nm.

Next, the absorption and PL spectroscopic investigations were performed to understand the optical properties of synthesized QDs. Fig. 4.2 shows the absorption and PL spectrum along with the excitation spectrum of water-dispersed ZnSe QDs. The absorption spectrum offers an extended range of absorption from 300-450 nm. The

characteristic absorption band is observed at around 400 nm, corresponding to transitions from the deep valance to the conduction band.

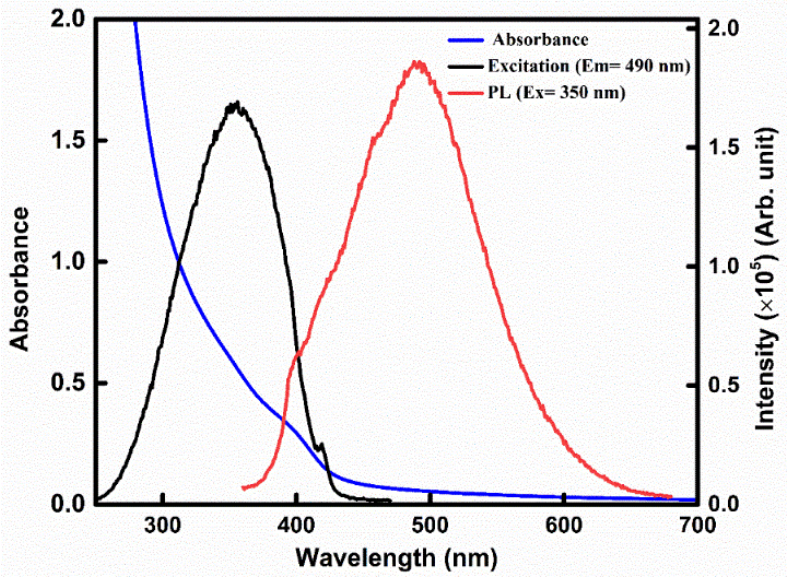

Figure 4.2. The absorption, PL and PL-excitation spectra of ZnSe QDs. The excitation wavelength was 350 nm and the emission wavelength for PL-excitation was 490 nm.

The PL excitation maximum is detected at 350 nm and well-matched with the absorption spectrum. The PL spectrum exhibit maximum at around 490 nm (λ_{ex} = 350 nm) with full-width half maxima (FWHM) of 124 nm and assigned to the PL of the defect states. The broad FWHM indicates the presence of different possible transition paths due to a large number of surface defects. The PL spectra of ZnSe QDs were also recorded at different excitation wavelengths varying from 320 to 380 nm with a step size of 10 nm at room temperature, as illustrated in Fig. 4.3a. This indicates the excitation independent PL behavior of ZnSe QDs and further signifies the uniformity in size ZnSe QDs. The blue emission has been observed with a maximum peak at 490 nm using an optimized excitation wavelength of 350 nm (see Fig. 4.3a inset) and represented with the help of CIE plot in Fig. 4.3b.

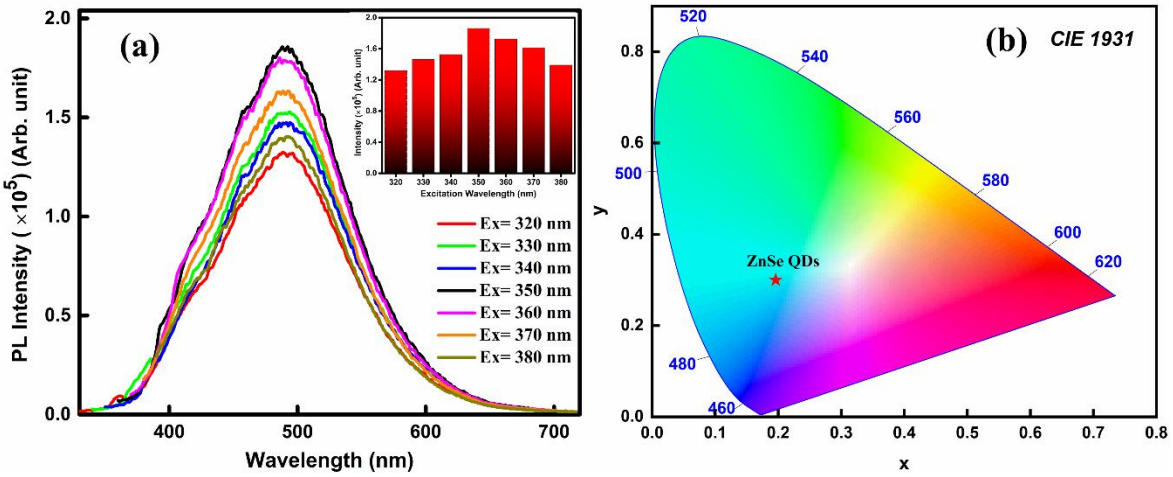

Figure 4.3. PL spectra of ZnSe QDs with different excitation wavelength (a) and intensity variation with excitations (inset). The CIE 1931 plot of synthesized ZnSe QDs with blue emission (b).

Further, the quantum yield or efficiency (QY), which is a significant parameter of fluorescent materials, was calculated using absorption and PL data of ZnSe QDs and quinine sulphate as a standard sample. The computed value of QY is found to be 7.4 % by employing the Eq. (1) given below:

$$QY_D = QYr \times \left(\frac{I_D}{I_r}\right) \times \left(\frac{A_r}{A_D}\right) \times \left(\frac{n_D}{n_r}\right)^2 \quad (4.1)$$

Where QY_r and QY_D are the quantum yields of reference, *i.e.,* quinine sulfate (0.54) and the ZnSe QDs, respectively [24]. A_D and A_r are the absorbance and I_D and I_r are corresponding integrated areas under the PL spectrum of QDs and the reference, respectively. n_r and n_D are the refractive indexes of the solvents used for reference and QDs, *i.e.,* sulfuric acid and distilled water, respectively. From the above-obtained results, it has been concluded that the blue light-emitting ZnSe QDs based sensing probe was successfully prepared and could be applied for sensing purposes.

Fig. 4.4(a) represents the absorption spectra of prepared ZnSe QDs in water with the addition of different concentrations of 2,4,6-TNP. The optical density of QDs was increased in the presence of 2,4,6-TNP, and the increase of the absorbance is observed

in terms of sharpening of the 354 nm band. The careful study of the absorption spectrum is useful in distinguishing between static and dynamic quenching. As the collisional quenching only disturbs the excited states, therefore no modifications in the absorption are observed.

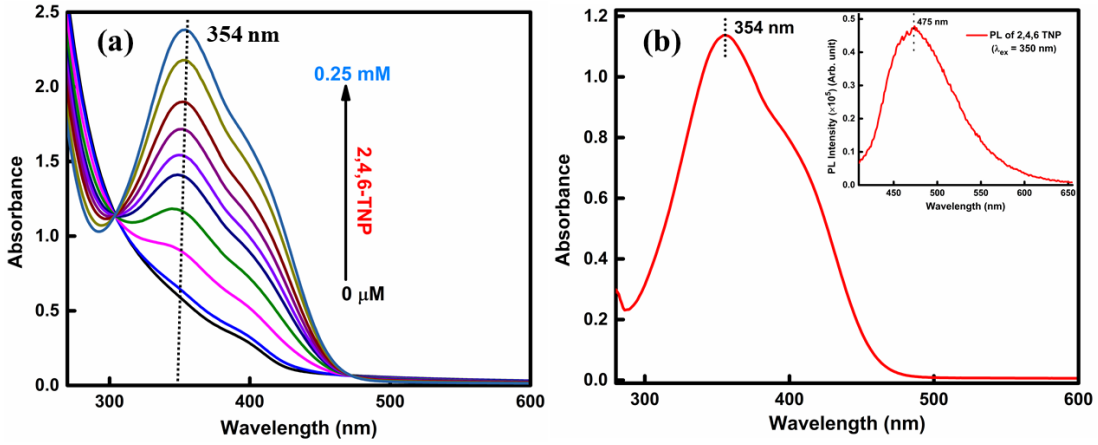

Figure 4.4. Absorption spectra of ZnSe QDs with a varying concentration of 2,4,6-TNP (a) and bare 2,4,6-TNP (b). The inset of (b) shows the PL spectrum of 2,4,6-TNP in water.

On the other hand, the ground-state complex formation will affect the absorption spectrum with a shift in the absorption band. But in our system, no such effects were observed with the addition of 2,4,6 TNP. Thus, we can say that neither static nor dynamic quenching mechanism was followed in this system. Further, a study of the bare 2,4,6 TNP absorption spectrum suggests that the obtained increase in absorbance of ZnSe QDs with the addition of 2,4,6 TNP was due to the individual absorbance of 2,4,6 TNP molecules, as shown in Fig. 4.4b. The PL spectrum of bare 2,4,6 TNP shows the band maximum at 475 nm, very close to the PL of ZnSe QDs (490 nm), as represented in the inset of Fig. 4.4b. Further, the PL study was carried out in the presence of 2,4,6-TNP, which shows a strong PL quenching of ZnSe QDs with 2,4,6-TNP.

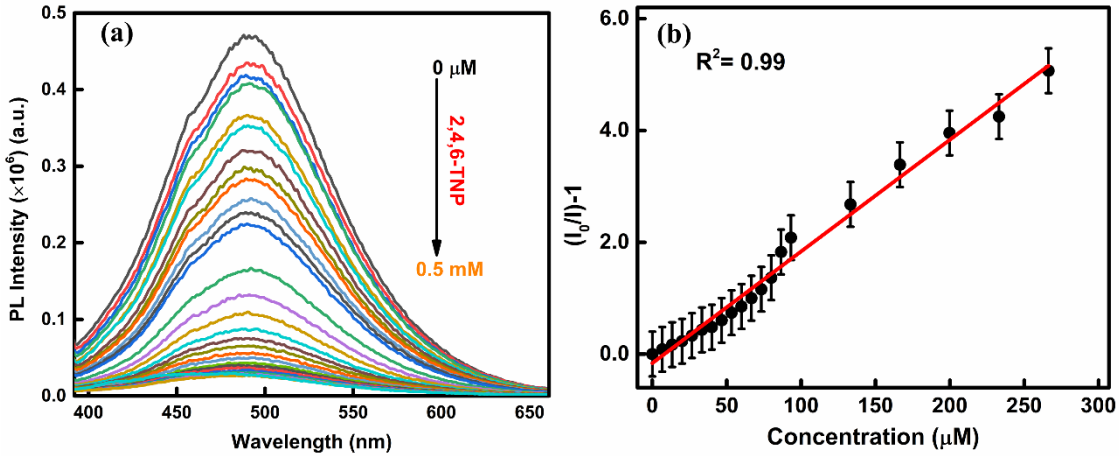

Figure 4.5. Photoluminescence spectra of ZnSe QDs (at λ_{ex}= 350 nm) in DI water with increasing concentration of 2,4,6-TNP (a) and the corresponding S-V plot (b).

Fig. 4.5(a) shows that the PL of ZnSe QDs at 490 nm gradually decreased in the presence of 2,4,6-TNP. With increasing concentration of 2,4,6-TNP, the PL intensity decreases monotonically, and the quenching process in the presence of 2,4,6-TNP is schematically represented in Fig. 4.6.

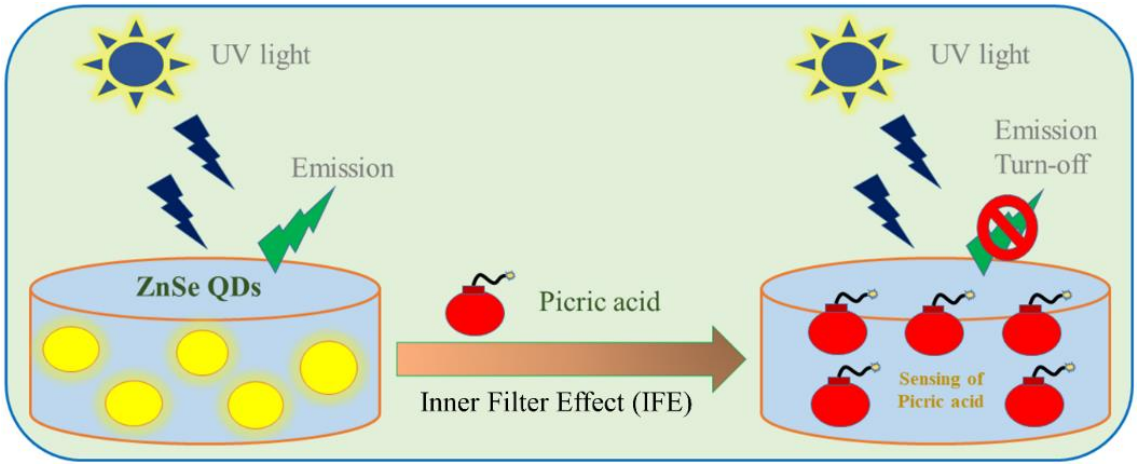

Figure 4.6. Schematic representation of recognition of 2,4,6-TNP in water through ZnSe QDs under UV light via PL turn-off mechanism.

A significant PL response of ZnSe QDs with 2,4,6-TNP was observed in the water, and the corresponding Stern-Volmer (S-V) plot of the changes of relative PL intensities of ZnSe QDs with increasing 2,4,6 TNP concentration, i.e., I_0/I vs. 2,4,6 TNP concentration was plotted by following Eq. (2).

$$\frac{I_0}{I} = 1 + K_{SV}[C] \quad (4.2)$$

Where I_0 and I are PL intensities of bare ZnSe QDs and with the quencher [2,4,6-TNP] respectively, ***C*** represents the molar concentration of [2,4,6-TNP] and K_{SV} is the quenching constant. The S-V plots exhibit a straight line over the concentration range 2.0 μM–0.25 mM with R^2 value of 0.98, as shown in Fig. 4.5b, which signifies that a single quenching mechanism is effective [25-27]. The value of the limit of detection (LoD) was calculated and came out to be 12.4×10^{-6} M for 2,4,6-TNP. To examine the selectivity of synthesized ZnSe QDs, a fluorescence study with the addition of different nitroaromatic compounds was performed. In the experiments, PL quenching titrations with various concentrations of 2,4,6-TNP in aqueous medium and other four nitroaromatic compounds, such as 2,6-DNT, 4-NT, 2-NT and 1,2-DNB, have been performed in the water + acetonitrile solution with a specific ratio, as these compounds are not completely soluble (or some are insoluble) in water.

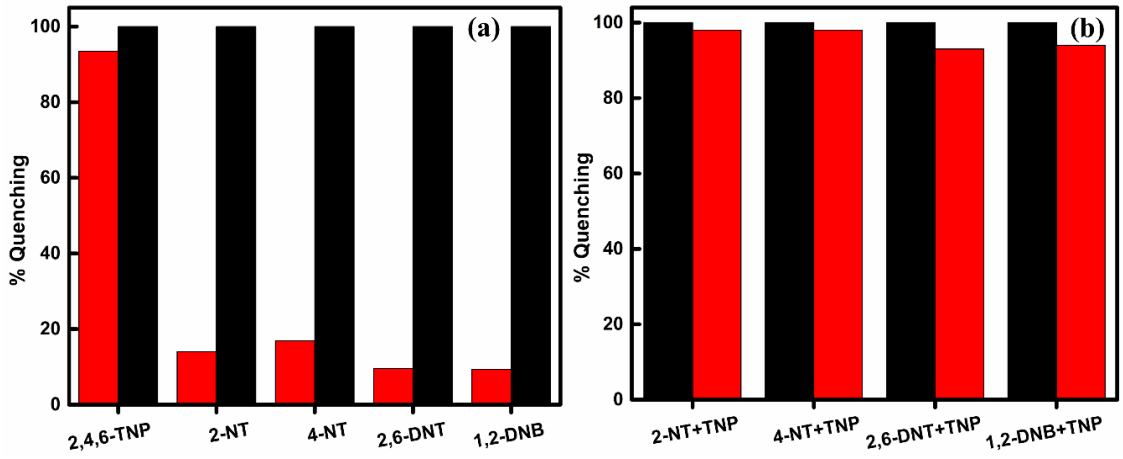

Figure 4.7. The bar graphs represent the percentage PL quenching of ZnSe QDs with a fixed concentration (0.40 mM) of 2,4,6-TNP, 2-NT, 4-NT, 2,6-DNT and 1,2-DNB (a) and in the presence of a fixed concentration of various nitroaromatic compounds along with 2,4,6-TNP, representing an anti-interference effect (b).

Fig. 4.7(a) illustrated the percentage quenching of PL with each nitroaromatic compound with the help of a bar graph. The significant and maximum quenching was observed with 2,4,6-TNP, i.e., 98%. For the reliability of the sensor, the interference effect was also carried out in the presence of various nitroaromatic compounds with 2,4,6-TNP, as represented in Fig. 4.7b. The result indicates that other nitroaromatic compounds do not affect the sensor and show an anti-interference effect with other compounds.

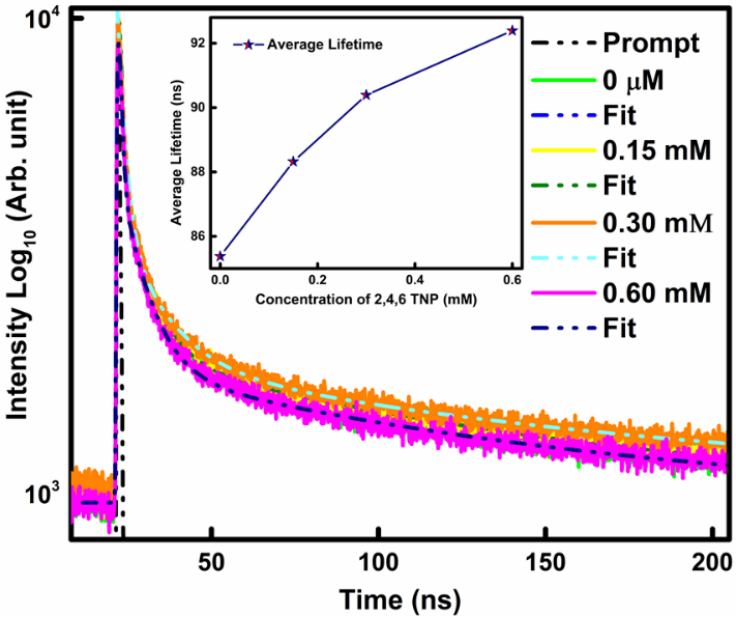

Figure 4.8. Fitted PL decay curves of ZnSe QDs in the water at varying concentrations of 2,4,6-TNP. The inset shows the variation in the average lifetime with the concentration of 2,4,6 TNP. The excitation and emission wavelengths were 340 and 490 nm, respectively.

The PL decay of pure ZnSe QDs and with the addition of 2,4,6 TNP was measured at a PL wavelength of 490 nm and using the excitation wavelength 340 nm for a deep understanding of the quenching mechanism, as shown in Fig. 4.8. The observed decay profiles could not well fit with a single and bi-exponential function [28,29] but are fitted well with tri-exponential functions as follows:

$$I(t) = \alpha_1 e^{\left(-\frac{t}{\tau_1}\right)} + \alpha_2 e^{\left(-\frac{t}{\tau_2}\right)} + \alpha_3 e^{\left(-\frac{t}{\tau_3}\right)} \quad (4.3)$$

where τ_i represents the lifetime components and α_i are the corresponding pre-exponential factors. The lifetime components are 111.39, 6.99 and 0.59 ns in the absence of TNP (Table 4.1).

The normalized amplitude of 0.56 ns lifetime is 82%, indicating the maximum contribution, whereas the longest lifetime component of 111.39 ns has the lowest contribution (4%). In the presence of TNP, the lifetime of all the components increases. The average PL lifetime (τ_{av}) calculated using the relation $\tau_{av} = \frac{\sum \alpha_i \tau_i^2}{\sum(\alpha_i \tau_i)}$, show a notable change in the presence of 2,4,6-TNP and varies from 85.38 ns to 92.39 ns, as shown in Table 4.1 and represented in Fig. 4.8 (inset). No additional lifetime component was noticed after adding 2,4,6-TNP in the ZnSe QDs solution, suggesting no new fluorescent entity formation. The increase in the average lifetime may be due to the increase in overall radiative rates.

Table 4.1. Fitted decay parameters and the average lifetime of ZnSe QDs with the addition of different concentrations of TNP. The excitation and emission wavelengths were 340 and 490 nm, respectively.

TNP (Conc.)	**τ_1 (ns)**	**τ_2 (ns)**	**τ_3 (ns)**	**α_1**	**α_2**	**α_3**	**τ_{av} (ns)**
0.00 μM	6.99±0.11	111.39±1.46	0.56±0.01	0.14	0.04	0.82	85.38
0.15 mM	6.98±0.10	112.99±1.38	0.52±0.01	0.13	0.04	0.83	88.32
0.30 mM	7.18±0.14	115.78±1.59	0.53±0.01	0.13	0.04	0.83	90.39
0.60 mM	11.78±0.35	121.09±2.17	1.91±0.02	0.20	0.09	0.71	92.39

To examine energy transfer phenomena, like fluorescence resonance energy transfer (FRET) and photoinduced electron transfer (PET) between the ZnSe QDs and

2,4,6 TNP, the PL spectrum of ZnSe QDs (donor) and the absorption spectrum of 2,4,6-TNP (acceptor) were recorded. The result shows that the actual overlapping of the absorption spectrum of 2,4,6 TNP and PL spectrum of ZnSe QDs is not enough for non-radiative energy transfer between the 2,4,6 TNP and ZnSe QDs, as shown in Fig. 4.9. Here, the absorption spectrum of the acceptor is observed at a lower wavelength region than the donor PL spectrum. Without any exception, the energy transfer takes from a donor absorbing at higher energies to acceptor absorbing at lower because a transfer in the reverse direction is forbidden for energetic reasons [30,31]. The study of absorption and PL of 2,4,6-TNP clears that the energy transfer from ZnSe QDs to 2,4,6-TNP and vice-versa is not feasible.

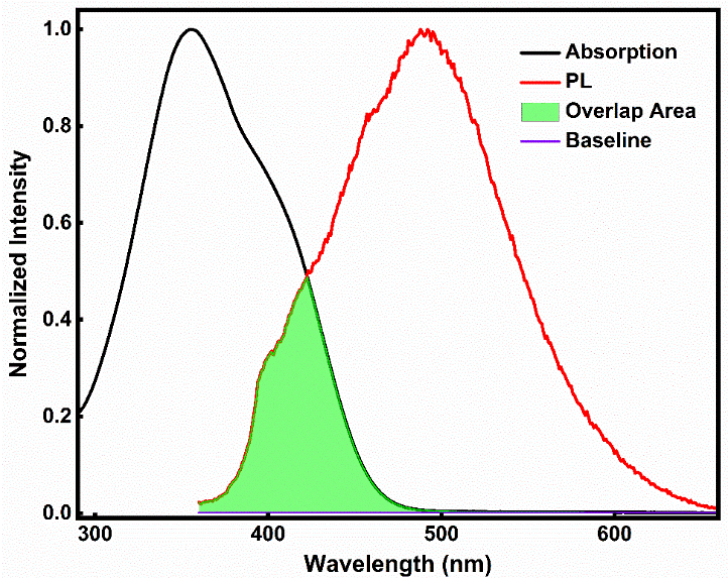

Figure 4.9. The spectral overlapping between the absorption of 2,4,6-TNP (acceptor) and PL spectrum of ZnSe QDs (donor).

The three most feasible and observed quenching mechanisms are photoinduced electron transfer (PET), fluorescence resonance energy transfer (FRET) and inner filter effect (IFE) [32-34]. The above findings suggested that FRET and PET are not accountable for the existing quenching. Further, the IFE quenching mechanism was tested for the proposed ZnSe QDs probe. The IFE is important in fluorescence

quenching, as it can affect the PL intensity during the experiment. The UV–vis absorption spectrum of 2,4,6 TNP, PL and PL-excitation spectra of ZnSe QDs were recorded and depicted in Fig. 4.10. There is a significant spectral overlapping between the absorption spectrum of 2,4,6 TNP and the excitation spectrum of ZnSe QDs. In other words, the excitation wavelength of ZnSe QDs was well-matched with the absorption band (excitation) of 2,4,6 TNP, which suggests that IFE is the major cause for PL quenching [35, 36]. One of the biggest causes of the IFE is the absorption of excitation and/or emission light by the quencher [37].

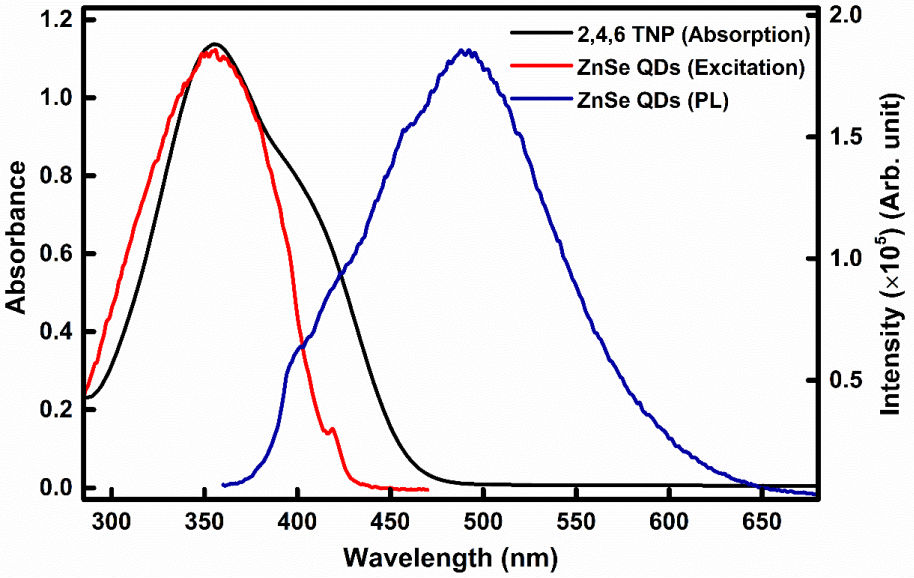

Figure 4.10. Spectral overlapping of the absorption spectrum of 2,4,6 TNP with PL and PL-excitation spectra of ZnSe QDs.

As the quencher concentration increases, the ability of the quencher to absorb the excitation/emission light will also increase, and thus, the quenching in PL intensity is observed. In the case of static quenching, lifetime should not change and in dynamic quenching, lifetime should decrease. The increase in the lifetime of individual components and the average lifetime of QDs with the addition of 2,4,6 TNP is primarily related to the decrease of non-radiative rates, which may be the absorption of excitation/emission light by 2,4,6 TNP. The variation in a PL lifetime of QDs with the

concentration of 2,4,6 TNP shows a linear behavior, as shown in the inset of Fig. 4.8. This suggests that the change in average lifetime is directly proportional to the concentration of 2,4,6 TNP in this system. The schematic representation of the inner filter effect as per the findings of absorption, PL and PL-excitation spectra of ZnSe QDs and 2,4,6 TNP is illustrated in Fig. 4.11.

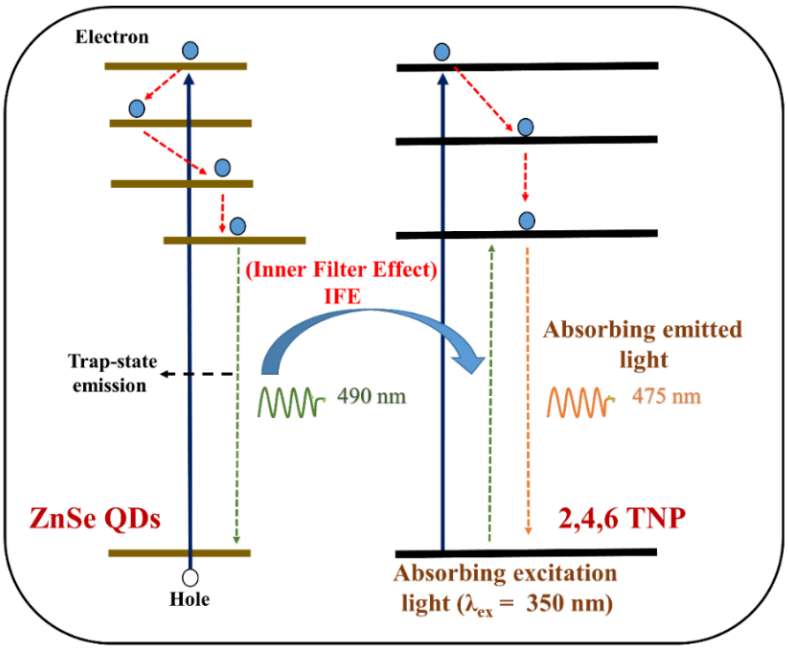

Figure 4.11. Schematic representation of inner filter effect in ZnSe QDs and 2,4,6 TNP system.

For the analogue of real sample analysis, the river water was used as a solvent for 2,4,6-TNP. The PL responses of ZnSe QDs under various concentrations of 2,4,6-TNP in river water were recorded according to the above pre-defined procedure. The observed results are shown in Fig. 4.12(a) and the corresponding S-V plot is given in 4.12(b). The S-V plot shows linearity over a range of 2.0 μM to 0.5 mM of 2,4,6-TNP with R^2 value 0.97, and the calculated LoD comes out to be 18.9×10^{-6} M.

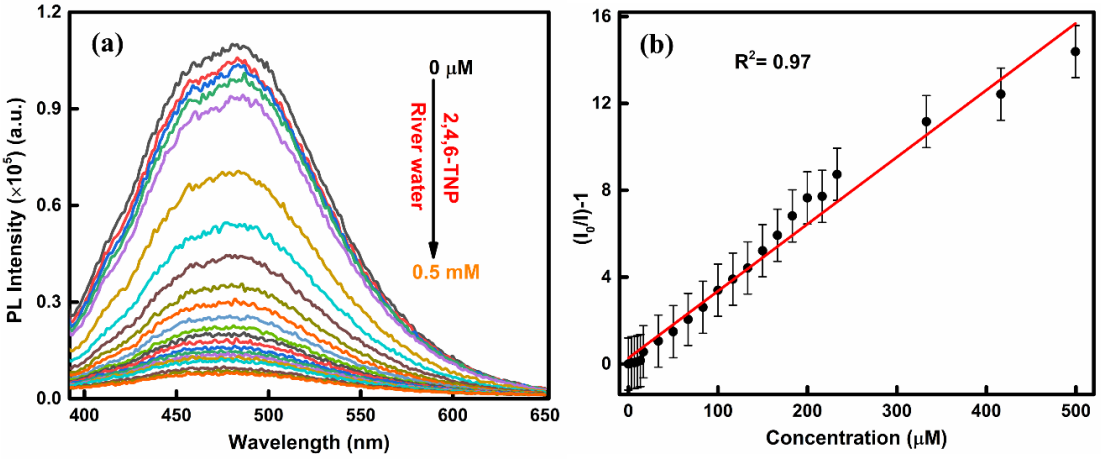

Figure 4.12. PL spectra (λ_{ex}= 350 nm) of ZnSe QDs in the river water with increasing concentration of 2,4,6-TNP (a) and the corresponding S-V plot (b).

The findings of PL quenching of ZnSe QDs by 2,4,6-TNP in DI water and river water are summarised in Table 4.2. The reason for the specific selectivity of ZnSe QDs towards the 2,4,6 TNP is the exactly matched excitation wavelength of ZnSe QDs with the absorption of 2,4,6 TNP. The other nitroaromatic compounds like 2-NT, 4-NT, 2,6-DNT, 1,2-DNB do not show a similar effect.

Table 4.2. Results of 2,4,6-TNP detection in DI water and real water samples through ZnSe QDs.

Samples	LoD (M)	Linearity range	Adj. R^2
DI water	12.4×10^{-6}	0.0-0.25 mM	0.99
River water	18.9×10^{-6}	0.0-0.50 mM	0.97

The stability under the variation of pH values was monitored via the change in PL intensity of ZnSe QDs. The ZnSe QDs shows good stability in the pH range of 8.0 to 12.0, and a minor decrease in the PL intensity is noticed in the pH range of 4.0 to 7.0, as shown in Fig. 4.13.

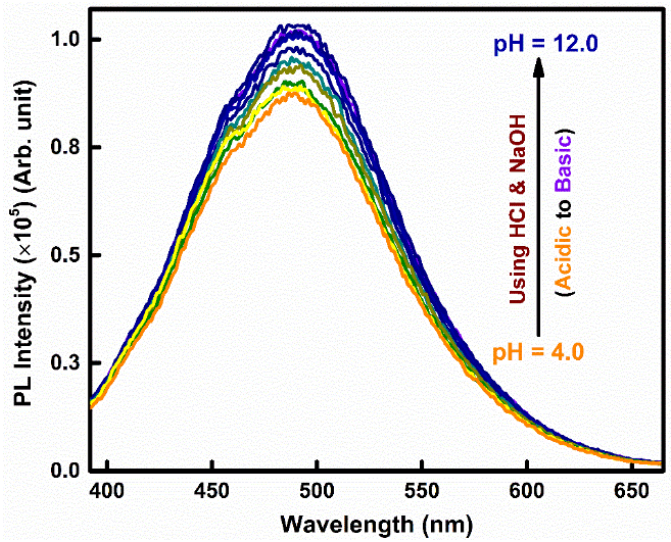

Figure 4.13. Photoluminescence spectra of ZnSe QDs at different pH from 4.0 to 12.0.

Form the obtained results, it has been proposed that the synthesized MPA-protected ZnSe QDs could be applied as a sensor for 2,4,6-TNP traces in water. The comparison of synthesized ZnSe QDs based probe with the other reported sensing probes for 2,4,6 TNP (picric acid) sensing is tabulated in Table 4.3.

Table 4.3. Comparison of ZnSe QDs probe with the reported probes for TNP sensing.

Probe	**Ligands**	**Synthesis Method**	**Analytes**	**LoD (μM)**	**Linearity range (μM)**	**Ref.**
ZnSe QDs	Mercaptopropionic acid (MPA)	Direct aqueous route	TNP	12.4	0.0 –250	[22]
MoS_2 QDs	Diaminobutane (DAB)	Hydrothermal	TNP	5.0	–	[38]
CdS QDs	lysozyme	Aqueous route	TNP	0.1	0.5–15	[39]
CdSe@SiO_2	Amino group (-NH_2)	Hot injection	TNP	0.05	0.1–100	[40]
N, B-CDs	None	Hydrothermal	TNP/Hg	0.35	0.02–0.16	[41]
N-GQDs	Creatinine	Carbonization	TNP	1.24	2 - 200	[42]

4.4. Conclusions

In summary, water-soluble ZnSe QDs having 7.4% of quantum efficiency were synthesized by the direct aqueous route. The synthesized ZnSe QDs show the fluorescence in the visible region (blue) has been utilized as a selective 2,4,6-TNP (picric acid) sensor among the various nitroaromatic compounds. The PL of fluorescent ZnSe QDs is selectively quenched with 2,4,6-TNP without showing any interference effects of other nitroaromatic compounds. The proposed probe shows a detection limit of 12.4 $\times 10^{-6}$ M and 18.9 $\times$ 10^{-6} M in DI water and river water, respectively. The emission intensity is quenched up to 98% with the addition of 2,4,6-TNP. The quenching mechanism has been discussed based on spectral and lifetimes measurements and indicates the feasibility of the inner filter effect with increasing concentration of 2,4,6-TNP as a possible PL quenching mechanism and precludes the FRET mechanism. The represented CIE plot suggests that the synthesized ZnSe QDs can also be used as an active material for blue QLED in various devices.

References

[1] S. Kumar, N. Venkatramaiah, S. Patil, Fluoranthene based derivatives for detection of trace explosive nitroaromatics, J. Phys. Chem. C. 117 (2013) 7236–7245.

[2] S. Shanmugaraju, S.A. Joshi, P.S. Mukherjee, Fluorescence and visual sensing of nitroaromatic explosives using electron rich discrete fluorophores, J. Mater. Chem. 21 (2011) 9130–9138.

[3] D.K. Singha, S. Bhattacharya, P. Majee, S.K. Mondal, M. Kumar, P. Mahata, Optical detection of submicromolar levels of nitro explosives by a submicron sized metal-organic phosphor material, J. Mater. Chem. A. 2 (2014) 20908–20915.

[4] O. Abuzalat, D. Wong, S.S. Park, S. Kim, Highly selective and sensitive fluorescent zeolitic imidazole frameworks sensor for nitroaromatic explosive detection, Nanoscale. 12 (2020) 13523–13530.

[5] M. Kaur, S.K. Mehta, S.K. Kansal, A fluorescent probe based on nitrogen doped graphene quantum dots for turn off sensing of explosive and detrimental water pollutant, TNP in aqueous medium, Spectrochim. Acta - Part A Mol. Biomol. Spectrosc. 180 (2017) 37–43.

[6] A. Chowdhury, P.S. Mukherjee, Electron rich triphenylamine based sensors for picric acid detection, J. Org. Chem., 8 (2015) 80.

[7] S.S. Nagarkar, A. V. Desai, P. Samanta, S.K. Ghosh, Aqueous phase selective detection of 2,4,6-trinitrophenol using a fluorescent metal-organic framework with a pendant recognition site, Dalt. Trans. 44 (2015) 15175–15180.

[8] K. Håkansson, R. V. Coorey, R.A. Zubarev, V.L. Talrose, P. Håkansson, Low-mass ions observed in plasma desorption mass spectrometry of high explosives,

J. Mass Spectrom. 35 (2000) 337–346.

[9] J.M. Sylvia, J.A. Janni, J.D. Klein, K.M. Spencer, Surface-enhanced Raman detection of 2,4-dinitrotoluene impurity vapor as a marker to locate landmines, Anal. Chem. 72 (2000) 5834–5840.

[10] M.E. Walsh, Determination of nitroaromatic, nitramine, and nitrate ester explosives in soil by gas chromatography and an electron capture detector, Talanta. 54 (2001) 427–438.

[11] M.E. Germain, M.J. Knapp, Optical explosives detection: From color changes to fluorescence turn-on, Chem. Soc. Rev. 38 (2009) 2543–2555.

[12] X. Chen, C. Sun, Y. Liu, L. Yu, K. Zhang, A.M. Asiri, H.M. Marwani, H. Tan, Y. Ai, X. Wang, S. Wang, All-inorganic perovskite quantum dots $CsPbX_3$ (Br/I) for highly sensitive and selective detection of explosive picric acid, Chem. Eng. J. 379 (2020) 122360.

[13] E.R. Goldman, I.L. Medintz, J.L. Whitley, A. Hayhurst, A.R. Clapp, H.T. Uyeda, J.R. Deschamps, M.E. Lassman, H. Mattoussi, A hybrid quantum dot - Antibody fragment fluorescence resonance energy transfer-based TNT sensor, J. Am. Chem. Soc. 127 (2005) 6744–6751.

[14] I.L. Medintz, H.T. Uyeda, E.R. Goldman, H. Mattoussi, Quantum dot bioconjugates for imaging, labelling and sensing, Nat. Mater. 4 (2005) 435–446.

[15] W.C.W. Chan, S. Nie, Quantum dot bioconjugates for ultrasensitive nonisotopic detection, Science. 281 (1998) 2016–2018.

[16] S. Dayal, C. Burda, Surface effects on quantum dot-based energy transfer, J. Am. Chem. Soc. 129 (2007) 7977–7981.

[17] P. Sharma, M.S. Mehata, Rapid sensing of lead metal ions in an aqueous medium by MoS_2 quantum dots fluorescence turn-off, Mater. Res. Bull. 131 (2020)

110978.

[18] R.K. Ratnesh, M.S. Mehata, Investigation of biocompatible and protein sensitive highly luminescent quantum dots/nanocrystals of CdSe, CdSe/ZnS and CdSe/CdS, Spectrochim. Acta - Part A Mol. Biomol. Spectrosc. 179 (2017) 201–210.

[19] M.S. Mehata, An efficient excited-state proton transfer fluorescence quenching based probe (7-hydroxyquinoline) for sensing trivalent cations in aqueous environment, J. Mol. Liquids, 326 (2021) 115379.

[20] N. Radhika, S.L. I, Synthesis of L-Cysteine capped ZnSe QDs and their photocatalytic activity, Int. J. Appl. Sci. Eng. 3 (2016) 5–7.

[21] M.K. Singh, M.S. Mehata, Phase-dependent optical and photocatalytic performance of synthesized titanium dioxide (TiO_2) nanoparticles, Optik. 193 (2019) 163011.

[22] V. Sharma, M.S. Mehata, Rapid optical sensor for recognition of explosive 2,4,6-TNP traces in water through fluorescent ZnSe quantum dots, Spectrochim. Acta-Part A Mol. Biomol. Spectrosc. 260 (2021) 119937.

[23] V. Sharma, M.S. Mehata, Synthesis of photoactivated highly fluorescent Mn^{2+}-doped ZnSe quantum dots as effective lead sensor in drinking water, Mater. Res. Bull. 134 (2021) 111121.

[24] J. R. Lakowicz, Principles of fluorescence spectroscopy, Springer, Singapore, (2010) 331–352.

[25] X. Gong, Y. Liu, Z. Yang, S. Shuang, Z. Zhang, C. Dong, An “on-off-on” fluorescent nanoprobe for recognition of chromium(VI) and ascorbic acid based on phosphorus/nitrogen dual-doped carbon quantum dot, Anal. Chim. Acta. 968 (2017) 85–96.

[26] L.K. Fraiji, D.M. Hayes, T.C. Werner, Static and dynamic fluorescence quenching experiments for the physical chemistry laboratory, J. Chem. Educ. 69 (1992) 424–428.

[27] M.E.K. Wahba, N. El-Enany, F. Belal, Application of the Stern-Volmer equation for studying the spectrofluorimetric quenching reaction of eosin with clindamycin hydrochloride in its pure form and pharmaceutical preparations, Anal. Methods. 7 (2015) 10445–10451.

[28] M.K. Singh, M.S. Mehata, Enhanced photoinduced catalytic activity of transition metal ions incorporated TiO_2 nanoparticles for degradation of organic dye: Absorption and photoluminescence spectroscopy, Opt. Mater. 109 (2020) 110309.

[29] Valeur, B. Molecular fluorescence: Principles and applications, Wiley, Weinheim, (2002) 256–260.

[30] Th. Förster, 10th spiers memorial lecture transfer mechanisms of electronic excitation, Faraday Soc. 27 (1959) 7.

[31] D.L. Dexter, A theory of sensitized luminescence in solids, J. Chem. Phys. 21 (1953) 836.

[32] H. Liu, M. Wang, Z. Li, C. Xin, G. Huang, A fluorescence sensing method for brilliant blue with gold nanoclusters based on the inner filter effect, Anal. Methods. 12 (2020) 4551–4555.

[33] S. Nath, S.K. Pathak, B. Pradhan, R.K. Gupta, K.A. Reddy, G. Krishnamoorthy, A.S. Achalkumar, A sensitive and selective sensor for picric acid detection with a fluorescence switching response, New J. Chem. 42 (2018) 5382–5394.

[34] N. Shao, Y. Zhang, S.M. Cheung, R.H. Yang, W.H. Chan, T. Mo, K.A. Li, F. Liu, Copper ion-selective fluorescent sensor based on the inner filter effect using

a spiropyran derivative, Anal. Chem. 77 (2005) 7294–7303.

[35] Q. Sun, Y. Long, S. Pan, H. Liu, J. Yang, X. Hu, Carbon dot-based fluorescent probes for sensitive and selective detection of luteolin through the inner filter effect, Luminescence. 33 (2018) 1401–1407.

[36] S. Kadian, G. Manik, A highly sensitive and selective detection of picric acid using fluorescent sulfur-doped graphene quantum dots, Luminescence. 35 (2020) 763–772.

[37] D. Zhang, Z. Dong, X. Jiang, M. Feng, W. Li, G. Gao, A proof-of-concept fluorescent strategy for highly selective detection of Cr(vi) based on inner filter effect using a hydrophilic ionic chemosensor, Anal. Methods. 5 (2013) 1669–1675.

[38] P. Sharma, M.S. Mehata, Colloidal MoS_2 quantum dots based optical sensor for detection of 2,4,6-TNP explosive in an aqueous medium, Opt. Mater. 100 (2020) 2–6.

[39] W. Na, X. Liu, S. Pang, X. Su, Highly sensitive detection of 2,4,6-trinitrophenol (TNP) based on lysozyme capped CdS quantum dots, RSC Adv. 5 (2015) 51428–51434.

[40] W. Gong, H. Li, X. Gong, Z. Zhang, Z. Lu, Fabrication of amine functionalized $CdSe@SiO_2$ nanoparticles as fluorescence nanosensor for highly selective and sensitive detection of picric acid, Spectrochim. Acta-Part A Mol. Biomol. Spectrosc. 233 (2020) 118221.

[41] Q. Ye, F. Yan, D. Shi, T. Zheng, Y. Wang, X. Zhou, L. Chen, N, B-doped carbon dots as a sensitive fluorescence probe for Hg^{2+} ions and 2,4,6-trinitrophenol detection for bioimaging, J. Photochem. Photobiol. B Biol. 162 (2016) 1–13.

[42] S. Chen, Y. Song, F. Shi, Y. Liu, Q. Ma, Sensitive detection of picric acid based

on creatinine-capped solid film assembled by nitrogen-doped graphene quantum dots and chitosan, Sensors Actuators, B Chem. 231 (2016) 634–640.

Chapter 5

Dual analytes (Hg^{2+} and Pb^{2+}) sensor in water using 3-marcaptoproponic acid protected Mn^{2+} doped ZnSe quantum dots

5.1. Introduction

Heavy metals are highly hazardous to the ecological environment and human health. Mainly, mercury and lead ions are dangerous to the health of human beings because of their high mobility, toxicity and capability to add through the atmosphere, water and food chains in the ecological system [1–5]. Even the small quantity intake of these heavy metals can causes serious health risks to living organisms. Therefore, due to the high health concerns, many researchers are working in a direction to develop various techniques or probes for effectively and quantitatively rapid on-site recognition of lead and mercury ions in the environment and water resources. Several probe materials are being developed for heavy metal ions detections under various conditions [6–10]. Still, developing rapid, facile and sensitive methods for efficiently recognizing such heavy metals in real samples remains challenging.

The various reported methods such as voltammetry, X-ray analysis method, atomic absorption spectroscopy, mass spectroscopy and UV-visible absorption spectroscopy [11–15] are used to detect heavy metals and other hazardous compounds. However, the above-listed methods are not convenient because of the complicated pretreatment of samples and expensive equipment requirements. Fluorescent sensors have attracted huge popularity in the last few years because they provide high technical

[*] *Content of this chapter has been published in* ***Chemical Physics Letters 787 (2022) 139270.***

simplicity, fast response time, high specificity and low detection limits. The working principle of fluorescent sensors deals with the emission of light when excited at lower wavelengths and the PL intensity (or PL lifetime) changes with the variation of concentration of the target analyte. Several compounds and materials, such as organic dyes [16], fluorescent aptamers [17], organic frameworks [18], porphyrins [19], metal-DNAzymes [20], or quantum dots [21] have been prepared for the recognition of toxic heavy metal. Hence, advanced analytical techniques for heavy metals recognition are highly preferred, such as fluorescent QDs based optical sensors with high quantum efficiency and sensitivity towards the analyte. In this regard, QDs have gained growing attention due to their unique properties and various benefits, such as facile synthesis route, low cost, high photo and chemical stability, low cytotoxicity, good biocompatibility, and superior quality luminescence properties with narrow-band emission and broad excitation spectrum. The excellent luminescence properties are essential in detecting various analytes via interaction with quantum dots and shows drastic fluctuation, such as fluorescence quenching. Over the past, researchers have studying numerous novel and effective fluorescent probes that can selectively respond to Hg^{2+} and Pb^{2+} ions [22-25]. However, there are various issues with the proposed QDs based fluorescent sensors, like the high intrinsic toxicity, use of hazardous ligands or solvents and high synthesis temperature range.

Keeping in view, in this work, a facile and non-toxic direct aqueous synthesis strategy is developed for MPA-protected Mn^{2+}-doped ZnSe QDs at a low temperature, i.e., 70 ℃. MPA was preferred because it has excellent thermal stability and can be used in transparent products with superior stabilizing properties. The successful Mn^{2+} doping gives a strong orange emission with relatively high quantum efficiency up to 17.3 %. As-prepared Mn@ZnSe QDs have been applied to recognize dual analytes Hg^{2+}

and Pb^{2+} in water through the optical fluorescence turn-off method, *i.e.*, optical sensor. The Mn@ZnSe QDs probe shows promising high sensitivity towards the analytes and could be distinguished through PL decays. The PL decays of synthesized QDs with Hg^{2+} and Pb^{2+} analytes show different behavior and lifetime values, i.e., the average lifetime monotonically decreases with increasing the amount (0 to 100 μM) of [Hg^{2+}] ion. In contrast, a different trend was observed in the presence of Pb^{2+}. Here, Mn@ZnSe QDs as active dual ions (Hg^{2+} and Pb^{2+}) sensing probe has been reported in the water. The sensing mechanism is also investigated, and results indicate that the possible mechanism is a non-radiative dynamic collisional interaction quenching.

5.2. Experimental section

All precursors and ligands were of analytical reagent (AR) spectroscopic mark and procured from reputed suppliers i.e., Sigma-Aldrich, Acros Organics, Alfa Aesar and CDH. The heavy metals involved in the sensing investigation were mercury (II) chloride, iron (II) perchlorate hydrate, cadmium (II) chloride hydrate, magnesium (II) perchloride hexahydrate, zinc (II) perchlorate hexahydrate, aluminium (III) perchlorate nonahydrate, calcium (II) perchloride tetrahydrate, cobalt (II) perchlorate hexahydrate, nickel (II) perchlorate hexahydrate, barium (II) perchlorate anhydrous and iron (III) perchlorate hydrate having purity (99.8%) were purchased from Sigma-Aldrich.

To synthesize the 3-mercaptopropionic acid (MPA, 99%) protected Mn^{2+}-doped ZnSe QDs, a direct aqueous medium route at low temperature was adopted with appropriate variations. The synthesis process was performed under the N_2 gas atmosphere and preserved the pH value 11.0 using NaOH solution. The NaHSe stock solution was prepared using sodium borohydride ($NaBH_4$, 95%) and elementary selenium powder (Se, 99.5%) in DI water at room temperature. The stock solution should be prepared cautiously and used in small quantities as the reaction was highly

exothermic. The main reaction was performed in a 250 mL three-neck flask containing zinc acetate (Zn^{2+}, 98%) precursor solution in DI water at 70 ℃ and 1 mL MPA as ligand. After a few minutes, the freshly prepared stock solution and simultaneously 0.2 mM manganese chloride ($MnCl_2$, 99%) as Mn^{2+} precursor was added to the main reaction slowly and in a controlled manner by using an injection. Further, lower down the temperature up to 60 ℃ and then kept the solution was kept for the growth of doped-QDs for a time of 90 min. After that, the prepared QDs were separated and purified by repetitive centrifuge with excess DI water and ethanol 3-4 times at 6500 rpm for 10 min.

5.3. Characterization techniques

Lambda-750 dual-beam UV-VIS spectrometer, Perkin-Elmer, was used to measure absorption spectra and study the change in absorbance with the interaction of analytes. The steady-state PL, PL efficiency and time-resolved photoluminescence (TRPL) spectra were acquired with Horiba Jobin Yvon, Fluorolog-3 spectrofluorometer mounted 450 W xenon, and flash lamps as excitation sources and a photomultiplier tube (PMT). High-resolution transmission electron microscopy (HR-TEM) imaging was carried out with TALOS, Thermo scientific instruments functioned at 200 kV accelerating voltage.

5.6. Results and discussion

The structural characterization of synthesized Mn@ZnSe QDs described using XRD and TEM images along with energy-dispersive X-ray spectrum (EDS) [26]. The XRD pattern shows the characteristic diffraction peaks at 2θ angles 53.5°, 45.2 and 27.3 corresponding to the diffraction planes (311), (220) and (111) respectively, which confirms the formation of cubic zinc blende structure. The TEM and HR-TEM images

illustrated the spherical morphology of Mn@ZnSe QDs with average particle size 3 to 4 nm and showed minor aggregation of particles.

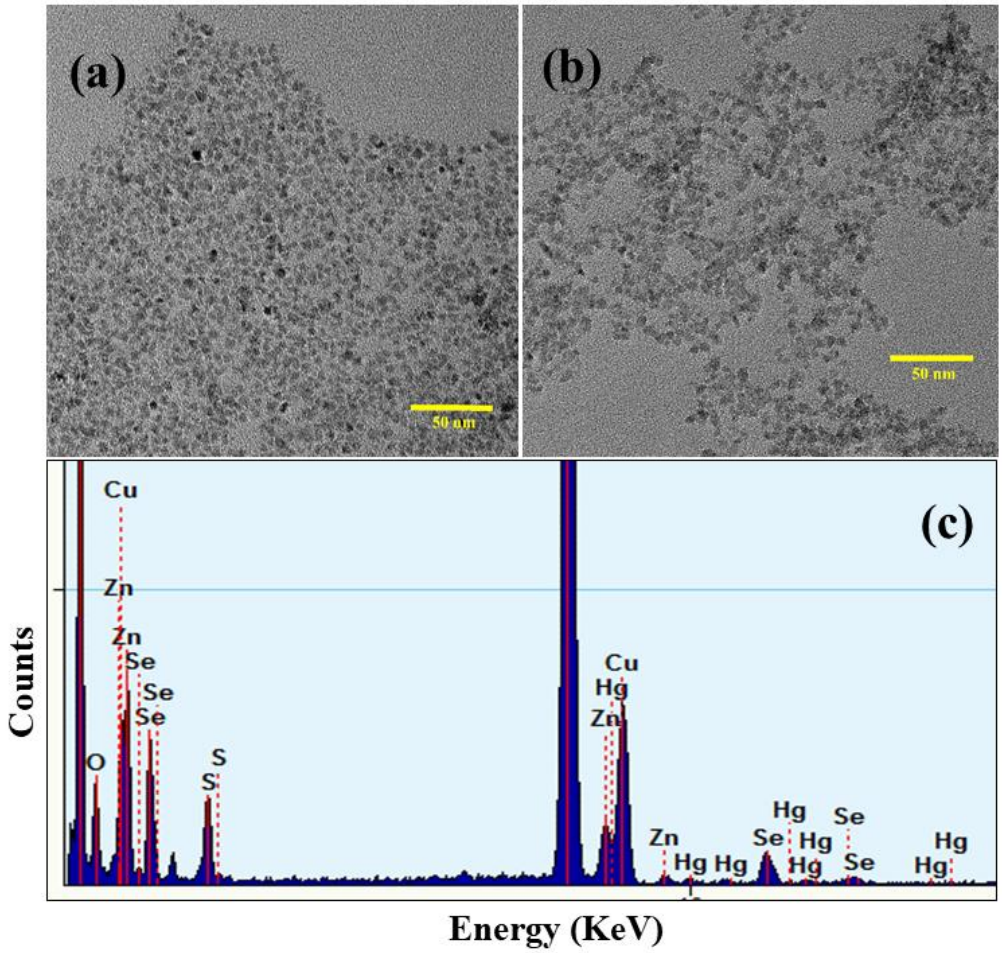

Figure 5.1. The TEM images of Mn@ZnSe QDs without Hg^{2+} (a), with the addition of Hg^{2+} (b) and corresponding EDS spectrum with a fixed amount of Hg^{2+} ions.

Herein, Fig. 5.1 represents the TEM images of synthesized Mn@ZnSe QDs without Hg^{2+} (a) and with the addition of Hg^{2+} ions (b) along with the corresponding EDS spectrum (c). Also, the images show the formation of a uniform and a large number of QDs in a small volume of sample (highly dense) with a particle size in the nano regime. The significant extent of Zn and Se peaks in EDS without any foreign elements peaks signifies the successful synthesis and purity of the Mn@ZnSe QDs. On comparing Fig. 5.1 (a) and (b), with the addition of Hg^{2+} ions in QDs, observed an increase in the contrast and aggregation of QDs in the same imaging conditions that

indicated the interaction of heavy metal (Hg^{2+}) ions with the QDs. It may be ascribed to the strong interaction between Hg^{2+} and -SH of MPA, or the cation-exchange reaction between Zn among ZnSe QDs and Hg^{2+}, which is further studied using other techniques or by testing different possible quenching mechanisms [27].

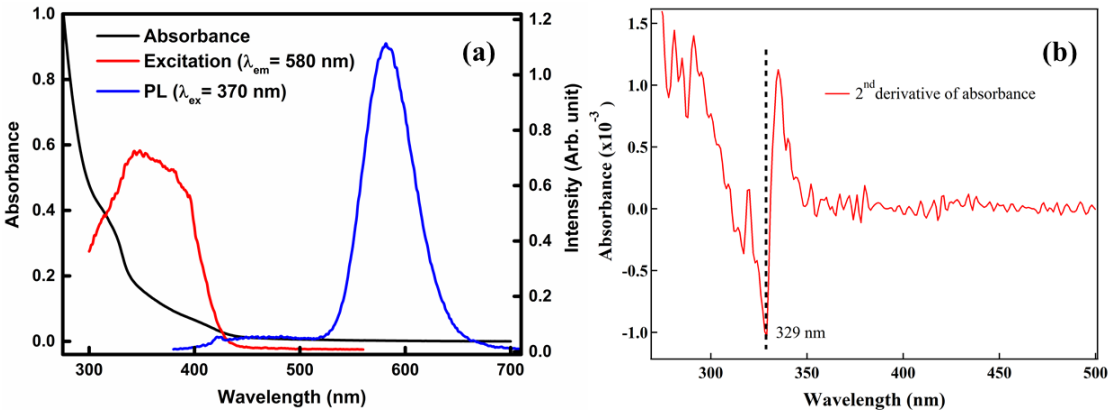

Figure 5.2. The absoption and excitation spectrum (λ_{em} = 580 nm) of Mn@ZnSe QDs along with the PL spectrum (λ_{ex} = 370 nm) (a). The absorption band edge at 329 nm obtained form the 2nd order derivative of absorbance (b).

Fig. 5.2(a) shows the absorption, PL and PL-excitation (λ_{em} = 580 nm) spectra of Mn@ZnSe QDs in DI water. The absorption spectrum shows a confinement band at around 320 nm corresponding to the valence band to the conduction band transitions of electrons, i.e., band-edge excitation. The absorption band edge was obtained at 329 nm from 2nd order derivative of absorbance as shown in Fig. 5.2(b). The excitation spectrum shows a broad band with a peak maximum at 350 nm, which was well-matched with the absorption spectrum. The PL spectrum (λ_{ex} = 370 nm) shows a sharp and narrow-band at 580 nm corresponding to the $^4T_1 \rightarrow {}^6A_1$ transition [28]. The PL quantum efficiency of photoactivated [29-30] Mn@ZnSe QDs calculated using the standard reference quinine sulfate [31] comes out to be 17.3%.

The effect/interaction of Hg^{2+} ions on Mn@ZnSe QDs in water was recorded with optical absorption and PL. Upon adding Hg^{2+} ions, the absorption intensity i.e.,

optical density (OD) of synthesized QDs increases with the concentration of Hg^{2+}, as shown in Fig. 5.3. A significant increase in OD of QDs was noticed without the appearance of any new band or shifting with an increasing concentration of [Hg^{2+}], which signified that there was no formation of ground-state complex or any new entities.

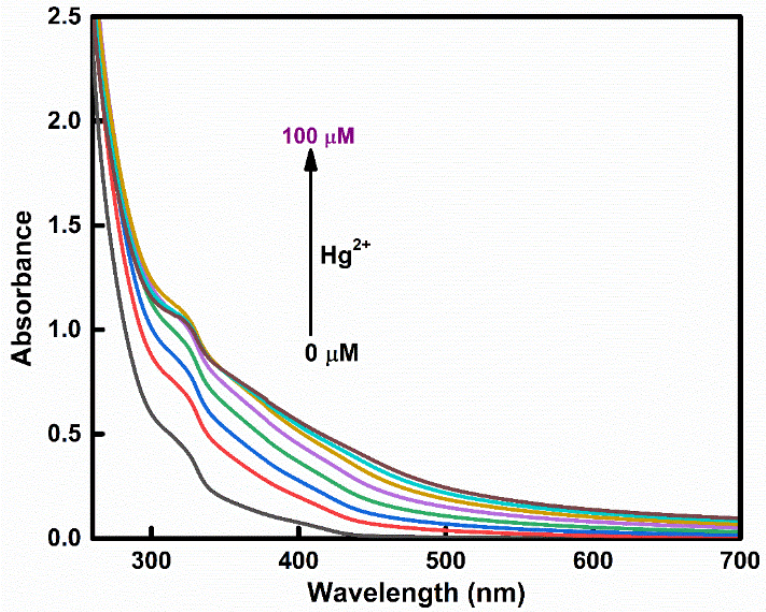

Figure 5.3. The absorption spectra of Mn@ZnSe QDs with varying concentration (0-100 μM) of Hg^{2+} ions.

In PL spectra under the excitation wavelength 370 nm, a gradual quenching of PL intensity has been detected, as illustrated in Fig. 5.4 with the addition of Hg^{2+} ions (0-100 μM). The PL intensity quenching of Mn@ZnSe QDs with Hg^{2+} in water under visible and UV light is also represented photographically in Fig. 5.4 (inset). The PL spectra shows a strong quenching without altering or changing the shape and peak position, which indicates no additional transitions from QDs in the presence of Hg^{2+} ions and makes the probe reliable and feasible for sensing applications.

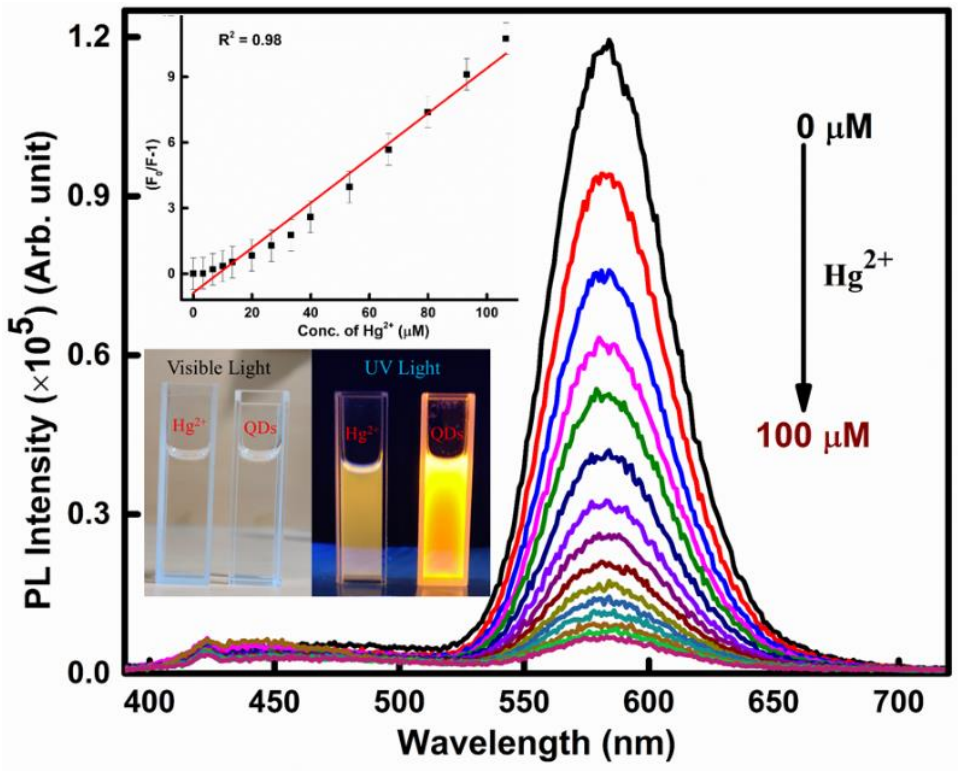

Figure 5.4. The PL spectra of Mn@ZnSe QDs in the presence of various concentration of Hg^{2+} ions. The linear S-V plot and photographic representations of quenching with Hg^{2+} under visible and UV light (inset).

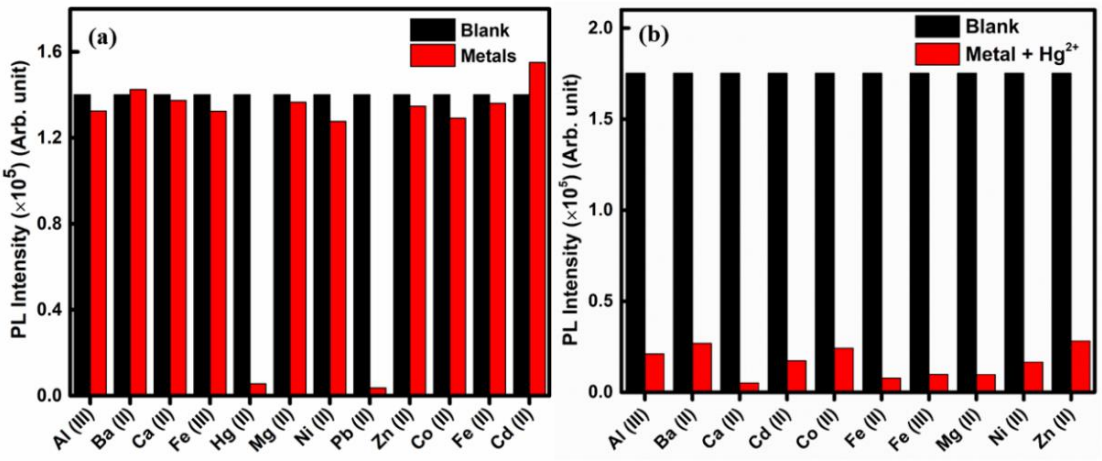

Figure 5.5. Bar diagram of PL intensity quenching of Mn@ZnSe QDs in the presence of various metal ions (a) and with a fixed concentration (100 μM) of [Hg^{2+}] in the presence of different metal ions (b).

For practical applications as a sensor, the probe should show a selective or distinct response towards a specific target. To test such distinct responses towards Hg^{2+} and Pb^{2+} ions, the PL spectra of Mn@ZnSe QDs were noted with numerous heavy metals, *i.e.*, Hg^{2+}, Pb^{2+}, Fe^{2+}, Zn^{2+}, Fe^{3+}, Co^{2+}, Cd^{2+}, Mg^{2+}, Cr^{2+}, Ca^{2+}, Ni^{2+} and Al^{3+} as illustrated in Fig. 5.5(a). The probe shows PL intensity quenching merely with Hg^{2+} and Pb^{2+} ions up to 98%, whereas the intensity was barely affected with other metal ions. For the sensor's reliability, the probe has been tested for Hg^{2+} and Pb^{2+} ions in the presence of other metals also, *i.e.*, the interference effect. The effect on PL intensity in the presence of various metal ions along with Hg^{2+} is represented in Fig. 5.5(b). It is important to note that even in the presence of other metal ions, the PL of QDs strongly quenched by Hg^{2+}. The PL quenching of synthesized QDs was also illustrated in Fig. 5.6 with Hg^{2+} and Pb^{2+} in the presence of other metals and found that there was no interference-effect.

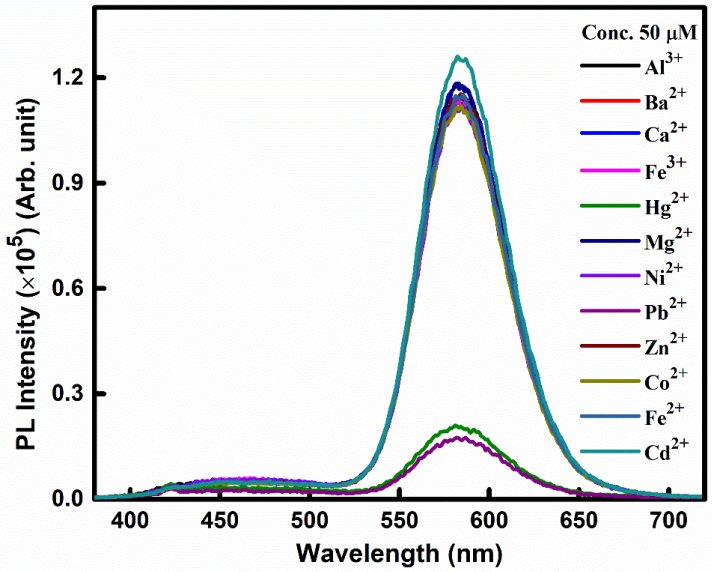

Figure 5.6. PL spectra of Mn@ZnSe QDs with a fixed amount (50 μM) of different heavy metal ions.

The lifetime measurements of Mn@ZnSe QDs in the water were performed with the addition of varying concentration (0-100 μM) of Hg^{2+} and the decays are

shown in Fig. 5.7. The lifetimes were collected at 580 nm emission wavelength with 370 nm excitation.

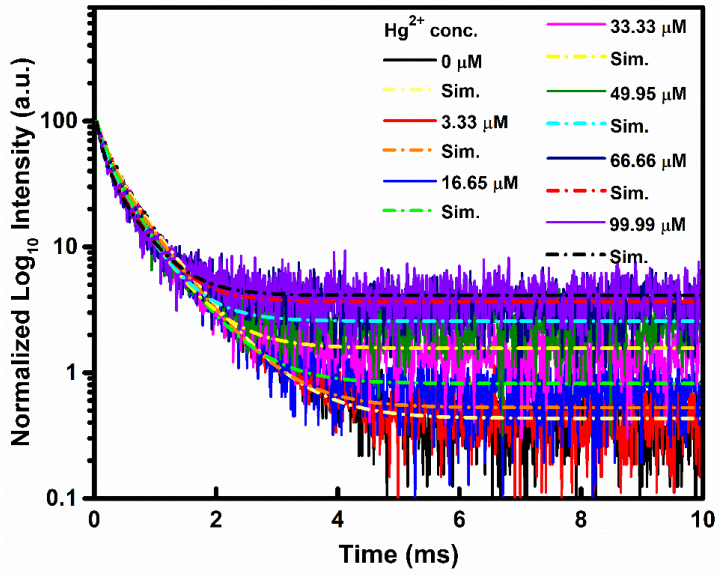

Figure 5.7. The PL decay curves of Mn@ZnSe QDs in the presence of different concentration of Hg^{2+} ions. Emission and excitation wavelengths were 580 nm and 370 nm, respectively.

The recorded decay curves were well-fitted with a bi-exponential function according to Eq. (5.1).

$$f(t) = \alpha_1 e^{\left(-\frac{t}{\tau_1}\right)} + \alpha_2 e^{\left(-\frac{t}{\tau_1}\right)} \quad (5.1)$$

Here, τ_1 and τ_2 represent the lifetime values. α_1 and α_2 are the corresponding amplitudes [32]. The lifetimes and corresponding amplitudes are summarized in Table 5.1. The average lifetime $<\tau>$ was estimated using Eq. (5.2), also given in Table 5.1.

$$< \tau > = \frac{\alpha_1\tau_1^2 + \alpha_2\tau_2^2}{\alpha_1\tau_1 + \alpha_2\tau_2}, \quad (5.2)$$

The normalized amplitude of both the lifetimes, τ_1 and τ_2 has almost equal contribution of 51 and 49%, respectively. The average lifetime of synthesized Mn@ZnSe QDs shows a decrease with Hg^{2+} ions concentration and the value decreases from 0.574 ms to 0.403 ms. The PL quenching mechanism and details of the specific interaction of

Mn@ZnSe QDs with Pb^{2+} ions have been discussed in the previous report, exhibits the dynamic interaction between the Pb^{2+} ions and Mn@ZnSe QDs by assisting non-radiative annihilation of charge carriers. The initial increase in the average lifetime of Mn@ZnSe QDs with Pb^{2+} concentration (0-15 µM) possibly due to the formation of PbSe centers which prompted the geometrical distortions. Thus, a decrease in the overall non-radiative decay rate was observed. With increasing higher concentration, the collisional rate increases that depopulate the excited states and thus observed a decrease in the lifetime with the further increase of Pb^{2+} [26].

Table 5.1. The lifetime and corresponding pre-exponential coefficients of Mn@ZnSe QDs with varying concentration of [Hg^{2+}]. The emission and excitation wavelengths were 580 nm and 370 nm, respectively.

(Mn@ZnSe)/Hg^{2+}	**τ_1 (ms)**	**τ_2 (ms)**	**α_1**	**α_2**	**τ_{av} (ms)**
0 µM	0.195 ± 0.003	0.687 ± 0.007	0.51	0.49	0.574
3 µM	0.179 ± 0.004	0.660 ± 0.007	0.51	0.49	0.554
15 µM	0.163 ± 0.008	0.615 ± 0.004	0.54	0.46	0.507
30 µM	0.132 ± 0.005	0.567 ± 0.01	0.52	0.48	0.479
50 µM	0.111 ± 0.007	0.495 ± 0.01	0.51	0.49	0.422
70 µM	0.102 ± 0.007	0.483 ± 0.01	0.53	0.47	0.409
100 µM	0.089 ± 0.006	0.478 ± 0.01	0.56	0.44	0.403

Here, the promising quenching mechanism of synthesized QDs with Hg^{2+} ions is based on the results of absorption, PL and PL lifetime. There was no significant change in the shape of the absorption spectrum in the presence of Hg^{2+} ions, indicating dynamic quenching as the prominent mechanism, as dynamic quenching does not affect the ground state absorption. Mn@ZnSe QDs gives a remarkable PL quenching with the addition of Hg^{2+} ions and follows a linear Stern-Volmer (S-V) relation between the relative PL intensity and concentration of Hg^{2+} ions, as shown in Fig. 5.4 (inset) according to Eq. (5.3).

$$\frac{F_0}{F} = 1 + K_{SV}[Q] \quad (5.3)$$

Here, F_0 and F represent the initial PL intensity and PL intensity after a specific amount of Hg^{2+} quencher [Q] in Mn@ZnSe QDs and K_{SV} stands for the S-V constant. The calculated K_{SV} value for Hg^{2+} from the linear S-V plot is 1.02×10^5 L mol^{-1} and the value of the limit of detection (LoD) calculated with equation $3\sigma/K$ obtained to be 28.6×10^{-6} mol L^{-1}. Here σ denotes the standard deviation and K_{SV} represents the slope of the linear S-V plot. The dynamic quenching can also be explained by PL lifetime measurements because there is a comparable decrease in PL lifetime and intensity. The reduction in the average lifetime of Mn@ZnSe QDs was observed with the increase in the concentration of Hg^{2+}. Using the lifetime, the rate constant (k_q) of quenching is calculated with the equation $K_{SV} = k_q \tau_0$ and comes out to be 1.77×10^8 L mol^{-1} s^{-1}. Where, τ_0 represents the lifetime of Mn@ZnSe QDs without Hg^{2+} ions. The reduction in the average lifetime and the PL intensity quenching with the addition of quencher also suggests that the possible quenching mechanism was a dynamic quenching, which provides an additional decay path for depopulation of excited states via a non-radiative route [33]. The obtained linear S-V plot is an adequate description in the case of a dynamic quenching mechanism, i.e., the collisional interaction [34-37].

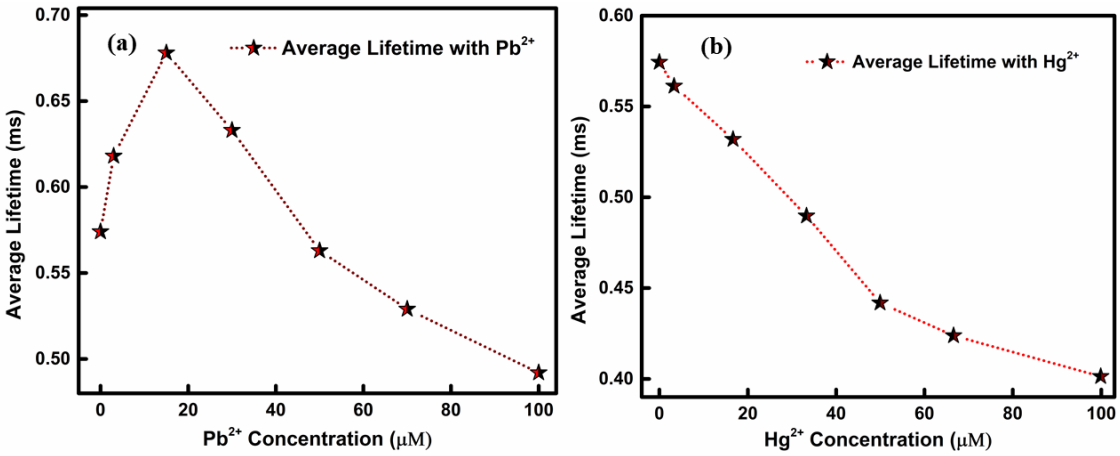

Figure 5.8. Plots of average PL lifetime of Mn@ZnSe QDs with the addition of Pb^{2+} (a) and Hg^{2+} ions (b).

Fig. 5.8 shows the behavior and change of the average lifetime of Mn@ZnSe QDs with the addition of Pb^{2+} Fig. 5.8(a) and Hg^{2+} Fig. 5.8(b) ions. The average lifetime behaves differently for Pb^{2+} and Hg^{2+} ions, which provides the key to distinguished the effects of both the quenchers. The stability of the probe was tested at different pH values varying from 4 to 12 using 0.1M HCl and NaOH solutions. As illustrated in Fig. 5.9, the PL spectra show good stability of the probe over a wide pH range.

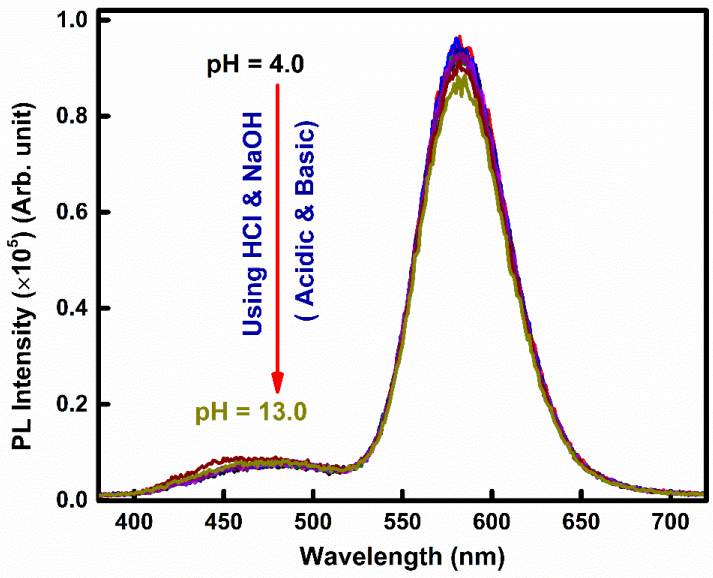

Figure 5.9. The effect of pH on PL intensity of Mn@ZnSe QDs.

Finally, the Mn@ZnSe QDs sensing probe was tested for real sample analogue using river water as a solvent without any purification. The PL quenching was recorded

with the addition of pre-defined varying concentration from 0 to 100 µM of Hg^{2+} ions, as shown in Fig. 5.10 and the corresponding S-V plot (inset). The estimated value for LoD in river water comes out to be 23.4×10^{-6} mol L^{-1}. The results suggest that the prepared Mn@ZnSe QDs probe sensor for sensing dual ions (Hg^{2+} and Pb^{2+}) is highly adaptable and promisingly working in distilled water and real samples, i.e., river water.

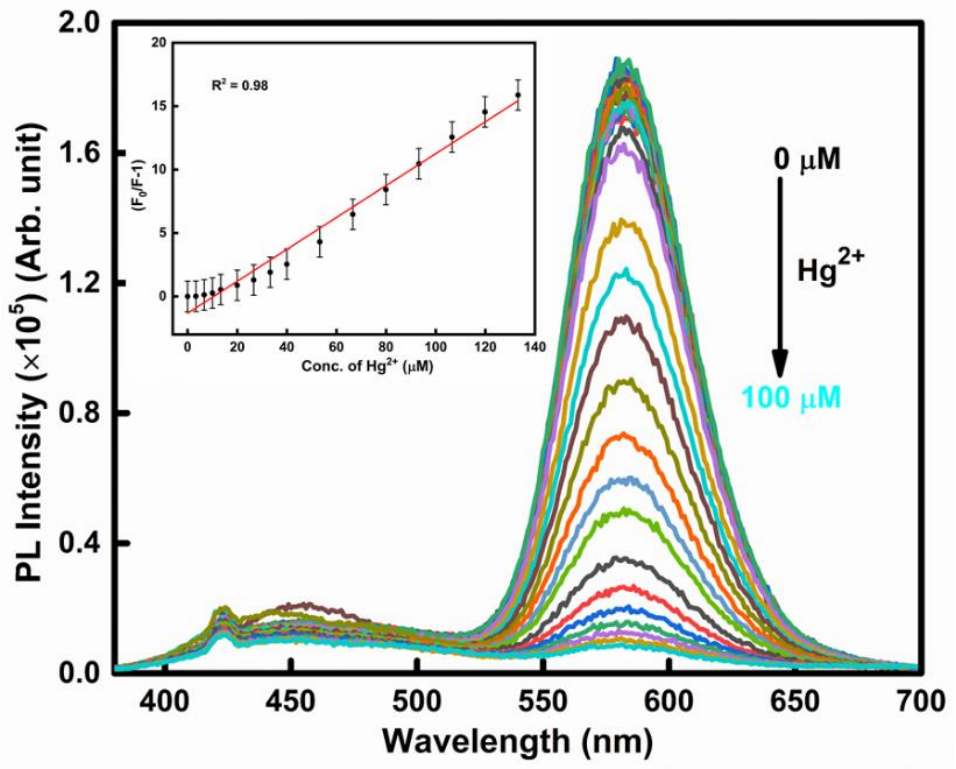

Figure 5.10. PL spectra of Mn@ZnSe QDs in river water with the addition of various concentration of Hg^{2+} and the corresponding linear S-V plot (inset).

For on-site applications, a filter paper-based sensor was developed by coating Mn@ZnSe QDs on the paper strips. The detailed procedure for the preparation of filter paper sensing strips and the colorimetric detection of Pb^{2+} ions was discussed in the previous report [26]. Herein, the prepared sensing strips have been successfully tested for sensing of Hg^{2+} via colorimetric and fluorometric detection methods. The quenching in the PL of the Mn@ZnSe QDs coated paper strip with the addition of increasing concentration of Hg^{2+} ions was recorded by placing the strip in a spectrofluorometer.

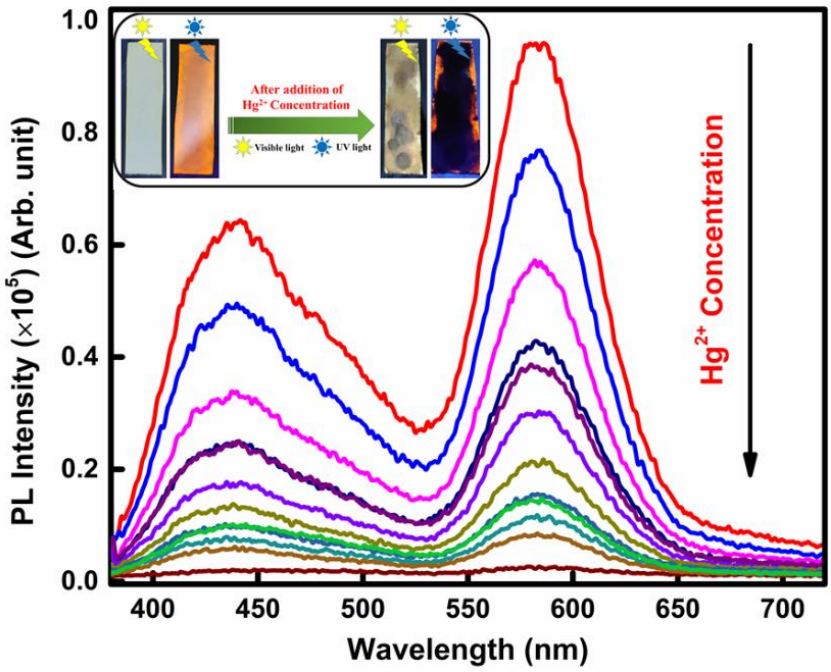

Figure 5.11. PL spectra of Mn@ZnSe QDs coated paper strip with Hg^{2+} ions and the photographic representation of colorimetric sensor under visible and UV light (inset).

Fig. 5.11 shows the change in the emission of the sensing strip with the addition of Hg^{2+} ions and the colorimetric detection with a camera under the visible light and UV lamp with a wavelength of 365 nm (inset). The increased intensity of 435 nm band can be explained with the help of PL spectrum of uncoated filter paper strips overlapped with Mn@ZnSe QDs coated filter paper strip, as shown in Fig. 5.12

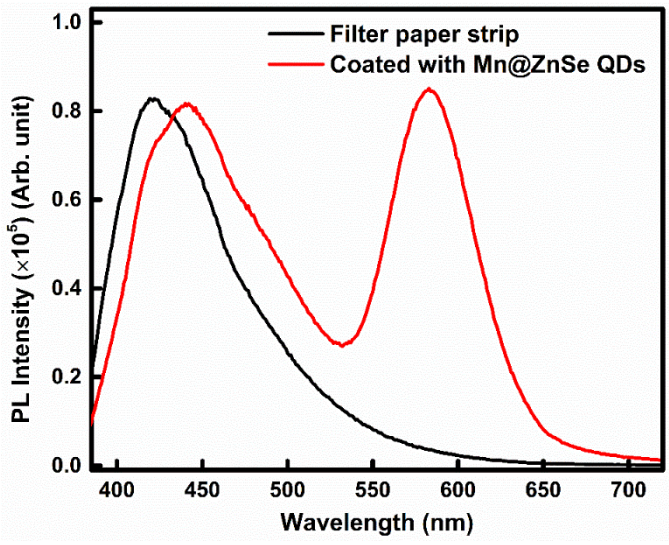

Figure 5.12. PL spectra of uncoated and Mn@ZnSe QDs coated filter paper strip.

5.7. Conclusions

In conclusion, the MPA-protected Mn@ZnSe QDs were successfully synthesized at optimized conditions and ambient temperature using a direct aqueous route. As-synthesized Mn@ZnSe QDs were employed as dual Pb^{2+} and Hg^{2+} sensors in the water. Mn@ZnSe QDs probe shows drastic PL quenching up to 98% with small concentrations of Pb^{2+} and Hg^{2+}. PL quenching with both the metal ions can be distinguished from the PL lifetimes as both the metal ions interact differently with MPA-protected Mn@ZnSe QDs. The average lifetime decreases monotonically with the increasing amount of Hg^{2+} while increasing with Pb^{2+} ions. The average lifetime increases at initial concentrations and decreases subsequently [20]. The steady-state PL and PL decay analysis suggest that the feasible quenching mechanism is a non-radiative collisional/dynamic interaction of Hg^{2+} ions with the Mn@ZnSe QDs.

References

[1] L.M. Campbell, D.G. Dixon, R.E. Hecky, A review of mercury in Lake Victoria, East Africa: Implications for human and ecosystem health, 2003.

[2] S.A. Robinson, M.J. Lajeunesse, M.R. Forbes, Sex differences in mercury contamination of birds: Testing multiple hypotheses with meta-analysis, Environ. Sci. Technol. 46 (2012) 7094–7101.

[3] B.C. Hopkins, J.D. Willson, W.A. Hopkins, Mercury exposure is associated with negative effects on turtle reproduction, Environ. Sci. Technol. 47 (2013) 2416–2422.

[4] X. Yang, E. Wang, A nanoparticle autocatalytic sensor for Ag^{+} and Cu^{2+} ions in aqueous solution with high sensitivity and selectivity and its application in test paper, Anal. Chem. 83 (2011) 5005–5011.

[5] P. Sharma, M.S. Mehata, Rapid sensing of lead metal ions in an aqueous medium by MoS_2 quantum dots fluorescence turn-off, Mater. Res. Bull. 131 (2020) 110978.

[6] A. Zhitkovich, Chromium in drinking water: Sources, metabolism, and cancer risks, Chem. Res. Toxicol. 24 (2011) 1617–1629.

[7] Y. Yang, L. Jing, X. Yu, D. Yan, M. Gao, Coating aqueous quantum dots with silica via reverse microemulsion method: Toward size-controllable and robust fluorescent nanoparticles, Chem. Mater. 19 (2007) 4123–4128.

[8] K. Bera, A.K. Das, M. Nag, S. Basak, Development of a Rhodamine–Rhodanine-Based Fluorescent Mercury Sensor and Its Use to Monitor Real-Time Uptake and Distribution of Inorganic Mercury in Live Zebrafish Larvae, Anal. Chem. 86 (5) (2014) 2740–2746.

[9] N. Fatma, M.S. Mehata, N. Pandey, S. Pant, Flavones fluorescence-based dual

response chemosensor for metal ions in aqueous media and fluorescence recovery, J. Fluoresc. 30 (2020) 759–772.

[10] R.K. Ratnesh, M.S. Mehata, Tunable single and double emission semiconductor nanocrystal quantum dots: a multianalyte sensor, Methods Appl. Fluoresc. 6 (2018).

[11] M.S. Chan, S. Da Huang, Direct determination of cadmium and copper in seawater using a transversely heated graphite furnace atomic absorption spectrometer with Zeeman-effect background corrector, Talanta. 51 (2000) 373–380.

[12] C. Collado-Sánchez, J. Pérez-Peña, M.D. Gelado-Caballero, J.A. Herrera-Melian, J.J. Hernández-Brito, Rapid determination of copper, lead and cadmium in unpurged seawater by adsorptive stripping voltammetry, Anal. Chim. Acta. 320 (1996) 19–30.

[13] J. Wu, E.A. Boyle, Low blank preconcentration technique for the determination of lead, copper, and cadmium in small-volume seawater samples by isotope dilution ICPMS, Anal. Chem. 69 (1997) 2464–2470.

[14] A.M. Garcia Rodriguez, A. Garcia De Torres, J.M. Cano Pavon, C. Bosch Ojeda, Simultaneous determination of iron, cobalt, nickel and copper by UV- visible spectrophotometry with multivariate calibration, Talanta. 47 (1998) 463–470.

[15] V. Sharma, M.S. Mehata, Rapid optical sensor for recognition of explosive 2,4,6-TNP traces in water through fluorescent ZnSe quantum dots, Spectrochim. Acta-Part A Mol. Biomol. Spectrosc. 260 (2021) 119937.

[16] S. Cai, Y. Lu, S. He, F. Wei, L. Zhao, X. Zeng, A highly sensitive and selective turn-on fluorescent chemosensor for palladium based on a phosphine-rhodamine conjugate. Chem. Commun. 49 (2013) 822–824.

[17] Y. F. Zhu, Y. S. Wang, B. Zhou, J. H. Yu, L. L. Peng, Y. Q. Huang, X. J. Li, S. H. Chen, X. Tang, X. F. Wang, A multifunctional fluorescent aptamer probe for highly sensitive and selective detection of cadmium (II). Anal. Bioanal. Chem. 409 (2017) 4951–4958.

[18] J. Yang, Z. Wang, Y. Li, Q. Zhuang, W. Zhao, J. Gu, Porphyrinic MOFs for reversible fluorescent and colorimetric sensing of mercury (II) ions in aqueous phase. RSC Adv. 6 (2016) 69807–69814.

[19] M. Caselli, Porphyrin-based electrostatically self-assembled multilayers as fluorescent probes for mercury (ii) ions: A study of the adsorption kinetics of metal ions on ultrathin films for sensing applications. RSC Adv. 5 (2015) 1350–1358.

[20] J. L. He, S. L. Zhu, P. Wu, P. P. Li, T. Li, Z. Cao, Enzymatic cascade based fluorescent DNAzyme machines for the ultrasensitive detection of Cu(II) ions. Biosens. Bioelectron. 60 (2014) 112–117.

[21] H. Xu, R. Miao, Z. Fang, X. Zhong, Quantum dot-based turn-on fluorescent probe for detection of zinc and cadmium ions in aqueous media. Anal. Chim. Acta. 687 (2011) 82–88.

[22] Z. Cai, B. Shi, L. Zhao, M. Ma, Ultrasensitive and rapid lead sensing in water based on environmental friendly and high luminescent l-glutathione-capped-ZnSe quantum dots, Spectrochim. Acta - Part A Mol. Biomol. Spectrosc. 97 (2012) 909–914.

[23] H. Chu, D. Yao, J. Chen, M. Yu, L. Su, Double-emission ratiometric fluorescent sensors composed of rare-earth-doped ZnS quantum dots for Hg^{2+} detection, ACS Omega. 5 (2020) 9558–9565.

[24] X. Wang, X. Kong, Y. Yu, Y. Sun, H. Zhang, Effect of annealing on

upconversion luminescence of ZnO:Er^{3+} nanocrystals and high thermal sensitivity, J. Phys. Chem. C. 111 (2007) 15119–15124.

[25] Q. Zhao, X. Rong, H. Ma, G. Tao, Dithizone functionalized CdSe/CdS quantum dots as turn-on fluorescent probe for ultrasensitive detection of lead ion, J. Hazard. Mater. 250–251 (2013) 45–52.

[26] V. Sharma, M.S. Mehata, Synthesis of photoactivated highly fluorescent Mn^{2+}-doped ZnSe quantum dots as effective lead sensor in drinking water, Mater. Res. Bull. 134 (2021) 111121.

[27] R.E. Dong, P. Kang, X.L. Xu, L.X. Cai, Z. Guo, Cation-exchange strategy for a colorimetric paper sensor: Belt-like ZnSe nanoframes toward visual determination of heavy metal ions, Sens. Actuators B Chem. 312 (2020) 128013.

[28] V. Sharma, M.S. Mehata, A parallel investigation of un-doped and manganese ion-doped zinc selenide quantum dots at cryogenic temperature and application as an optical temperature sensor, Mater. Chem. Phys. 276 (2022) 125349.

[29] C. Luo, B.o. Li, H. Peng, X. Tang, Y. Wang, J. Travas-sejdic, The effect of photoirradiation on the optical properties of thiol-capped CdTe quantum dots, J. Nanosci. Nanotechnol. 12 (4) (2012) 2998–3005.

[30] V. Krivenkov, A. Tretyachenko, P.S. Samokhvalov, A.A. Chistyakov, I. Nabiev, Controllable photo-brightening/photo-darkening of semiconductor quantum dots under laser irradiation, Nanophotonics VI. 9884 (2016) 98843L.

[31] G.A. Crosby, J.N. Demas, Measurement of photoluminescence quantum yields. Review, J. Phys. Chem. 75 (1971) 991–1024.

[32] M.K. Singh, M.S. Mehata, Enhanced photoinduced catalytic activity of transition metal ions incorporated TiO_2 nanoparticles for degradation of organic dye: Absorption and photoluminescence spectroscopy, Opt. Mater. 109 (2020)

110309.

[33] Fraiji, L. K.; Hayes, D. M.; Werner, T. C. Static and dynamic fluorescence quenching experiments for the physical chemistry laboratory. J. Chem. Edu. 69 (1992) 424-428.

[34] E.M. Soliman, M.E. Mahmoud, S.A. Ahmed, Reactivity of thioglycolic acid physically and chemically bound to silica gel as new selective solid phase extractors for removal of heavy metal ions from natural water samples, Int. J. Environ. Anal. Chem. 82 (2002) 403–413.

[35] S.A. Elfeky, Facile sensor for heavy metals based on thiol-capped CdTe quantum dot, J. Environ. Anal. Chem. 5 (2018) 1–5.

[36] M. Bhatt, S. Bhatt, G. Vyas, I.H. Raval, S. Haldar, P. Paul, Water-dispersible fluorescent carbon dots as bioimaging agents and probes for Hg^{2+} and Cu^{2+} ions, ACS Appl. Nano Mater. 3 (2020) 7096–7104.

[37] G. S. Ghodake, S. K. Shinde, R. G. Saratale, A. A. Kadam, G. D. Saratale, A. Syed, F. Ameen, D. Y. Kim, Colorimetric detection of Cu^{2+} based on the formation of peptide-copper complexes on silver nanoparticle surfaces, Beilstein J. Nanotechnol. 9 (2018) 1414–1422.

Chapter 6

Investigation of un-doped and manganese ion-doped zinc selenide quantum dots at cryogenic temperature: Optical temperature sensor

6.1. Introduction

The fast increasing attention in the exploration of optical or photosensitive properties of low-dimensional structures, mainly zero-dimensional (0-D) systems, encouraging the improvement of upcoming generation solid-state devices in the areas of optoelectronics, photonics and microelectronics. More specifically, semiconductor quantum dots or 0-D materials are used in the development of various electronics technology. The luminescence and other physical properties of semiconductor QDs are highly dependent on altering the electron energy bands triggered by the size aspect [1-4]. However, excitons mechanisms of optical excitation and quantum confinement have also greatly affected the photoluminescence (PL) efficiency of QDs. According to the literature survey, the temperature dependence of PL in semiconductor QDs can considerably differ in nature and shape while using different excitation systems [5,6]. The temperature-dependent PL spectra of QDs are primarily displayed in the decreasing functions (like intensity) with the rising temperature and the PL spectra observed with a sharp maximum or an increase in PL intensity at low temperatures. These results are well-defined characteristics of direct PL excitation of confined excitons [7-11]. Generally, various spectral parameters of QDs are determined by geometric and sized factors and the shape of the temperature-dependent PL spectrum is also significantly

[*] *Content of this chapter has been published in* ***Materials Chemistry and Physics 276 (2022) 125349.***

changed. Thus, this gives information about confined excitons in QDs and can be analyzed by the temperature dependence of PL [12-13].

Compared with organic dyes/polymers, the fluorescence QDs based nanostructures including inorganic quantum dots (QDs), carbon dots (C-dots) and inorganic perovskite nanocrystals (NCs) have been utilized in many optoelectronic devices like photovoltaic devices, LEDs and displays because of their high quantum yield and stability [14-18]. Few of the classes of such inorganic QDs are the cadmium or lead-based cadmium selenide (CdSe), cadmium telluride (CdTe), lead selenide (PbSe), and mixed QDs, which can be developed using various organometallic and aqueous methods [19-21]. But due to their intrinsic toxicity, the practical practice of these QDs in various applications is hindered and unsafe. Therefore, there is a requirement to replace the cadmium or lead ions and develop less toxic nanomaterials for various applications. In this regard, zinc-based QDs gained remarkable attention as fluorescent QDs due to their excellent quantum efficiency, low intrinsic toxicity, and significant solubility in water. Therefore, zinc-based QDs are extensively used in numerous fields and applications. Among the numerous applications of QDs, optical temperature sensors for precise temperature measurement have a growing importance in physiological and biochemical processes [22-23]. Several promising approaches are being applied and studied for rapid temperature sensors, such as Raman spectroscopy, scanning probe microscopy and fluorescence-based techniques [24-25]. The fluorescence technique-based temperature sensors are fascinating due to their safety of remote handling, high spatial resolution and fast response [26-27]. The general working of these sensors is based on monitoring the change in lifetime or PL intensity triggered by temperature [28]. Moreover, the main drawbacks of early temperature sensors are

the high toxicity of the QDs, limited temperature response range and poor long-term stability [29-30].

In this report, the ZnSe and Mn@ZnSe QDs were prepared with a direct aqueous synthesis approach by taking the thiol ligand as a stabilizer. The prepared ZnSe and Mn@ZnSe QDs give strong emission of blue and orange colors, respectively. Compared with conventional semiconductor QDs, the synthesized ZnSe and Mn@ZnSe QDs may be favorable alternatives as temperature sensing probes because of their high stability and low intrinsic toxicity. The proposed temperature sensing probes also have minimized the above-listed drawbacks of early reported temperature sensors. Furthermore, the temperature-dependent steady-state PL and time-resolved PL studies show that the developed probes have excellent temperature-dependent PL properties with linearly temperature-dependent PL intensity.

6.2. Experimental details

6.2.1. Materials and Synthesis

All the precursors and ligands are used of AR spectroscopic grade. Zinc acetate dihydrate (98%), selenium powder (99.5%), sodium borohydride (95%), 3-mercaptopropionic acid (MPA, 99%), manganese (II) chloride (99%) and ethanol were purchased from well-known and reputed distributors of chemicals like CDH, Sigma-Aldrich, Alfa Aesar and Acros Organics. The ultrapure water was consumed in the synthesis as solvent (resistivity of 18.2 MΩ.cm).

Highly stable and water-dispersible ZnSe and Mn@ZnSe QDs were prepared with a direct aqueous synthesis approach by taking MPA as a stabilizing ligand. For achieving successful Mn^{2+} doping in the ZnSe host, the nucleation doping strategy was adopted. First, the synthesis processes were carried out in an N_2 gas (inert) atmosphere, and the pH of the reaction was preserved to be 10.3 using NaOH solution. Then, the

reaction of selenium powder (Se) and reducing agent sodium borohydride ($NaBH_4$) in water at room temperature was carried out to obtain the freshly prepared stock solution of NaHSe. The obtained stock solution was moved to a 250 mL three-neck flask with the help of a syringe, which already has zinc acetate (Zn^{2+}) at 70 ℃. In addition, for the synthesis of Mn@ZnSe QDs, 0.1 mM solution of manganese chloride (Mn^{2+}) was prepared and added only 0.5 mL of Mn^{2+} in the reaction i.e. 3% molar concentration. After some time, 1 mL of MPA was added to the reaction mixture as a capping agent to control the size and shape of QDs. Lastly, the solution was kept at the same temperature for the growth of QDs. Then, the prepared QDs were separated and purified through the repetitive centrifuge to remove excess MPA ligand, unreacted precursors and other impurities. After that, the obtained purified solid was dried in the oven at 60 ℃ for 1 hour.

6.2.2. Characterizations

X-ray diffraction (XRD) measurements were recorded using the Ultima IV (Rigaku), Cu (K_α), λ = 1.54 Å radiation and operating acceleration voltage was 40 kV. Field emission scanning electron microscopy (FESEM) and energy-dispersive X-ray spectroscopy (EDS) measurements were performed with Zeiss, Gemini SEM 500, and captured high-resolution images through secondary electron detection mode. High-resolution transmission electron microscopy (HRTEM) by TALOS was used to capture the images, with the operating acceleration voltage of 200 kV. Perkin-Elmer, dual-beam UV/VIS/NIR spectrometer Lambda-750 was used for the UV/Vis spectroscopic studies. For the low-temperature measurements, Janis, VNF-100 cryostat was used with a temperature controller Cryo, Con 22C loaded with 50 Ω cartridge heater and silicon diode thermometers. Temperature-dependent photoluminescence (PL) and time-resolved photoluminescence (TRPL) studies were performed with Horiba Jobin Yvon,

Flurolog-3 spectrofluorometer, equipped with 450 W xenon lamp and flash lamp, a photomultiplier tube (PMT) and cryostat attachments to vary the temperature.

6.3. Results and discussion

The XRD curves of synthesized un-doped and Mn^{2+}-doped ZnSe nanoparticles are shown in Fig. 6.1. All the peaks are well matched and can be indexed to the standard data for the cubic zinc blende structure of ZnSe without observing the extra peaks of other phases or impurities. The three characteristic peaks are observed at Bragg's angles (2θ) around 27.3°, 45.6° and 54.1°, corresponding to the (111), (220) and (311) planes, respectively. Trivial broadening of the peaks was also observed because of the small crystallite size of particles, i.e., from QDs.

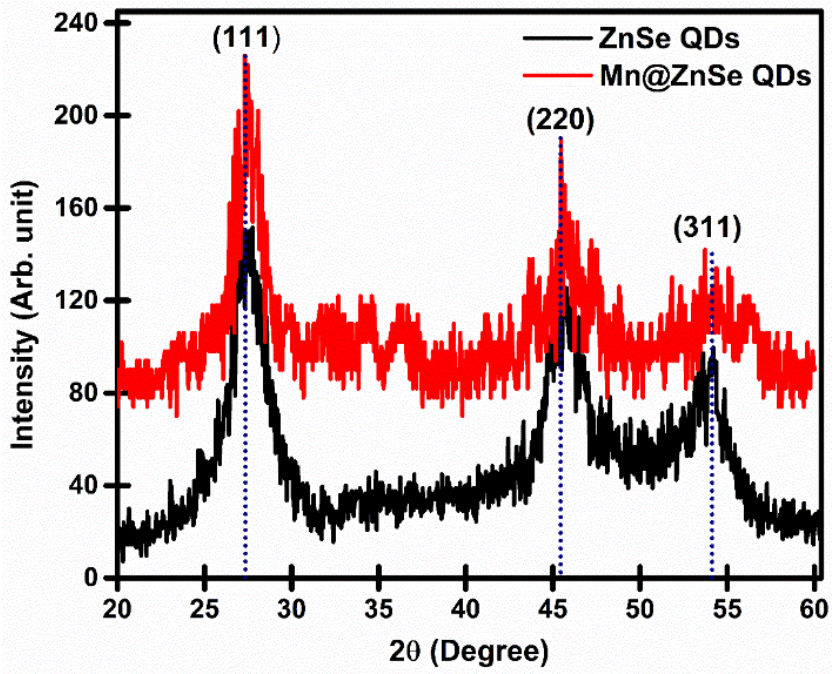

Figure 6.1. XRD patterns of synthesized ZnSe and Mn@ZnSe QDs at room temperature.

The crystallite size is calculated and comes out to be 4-5 nm by following Scherrer's equation (Eq. 6.1).

$$D = \frac{0.93\,\lambda}{\beta\,cos\,\theta} \qquad (6.1)$$

Where D denotes crystallite size, λ represents the used X-ray source wavelength, β is known as the full width at half maximum (FWHM) and θ is called the Bragg's angle. The XRD analysis reveals that with the Mn^{2+} ions doping, there is no change in the phase and crystallinity of ZnSe QDs and this signifies the deep nucleation doping of Mn^{2+} ions in the host.

The general surface morphological and elemental composition studies of as-prepared nanoparticles were performed using FESEM and EDS, as illustrated in Fig. 6.2. The SEM images reveal the monodisperse spherical structures with clear particle formation.

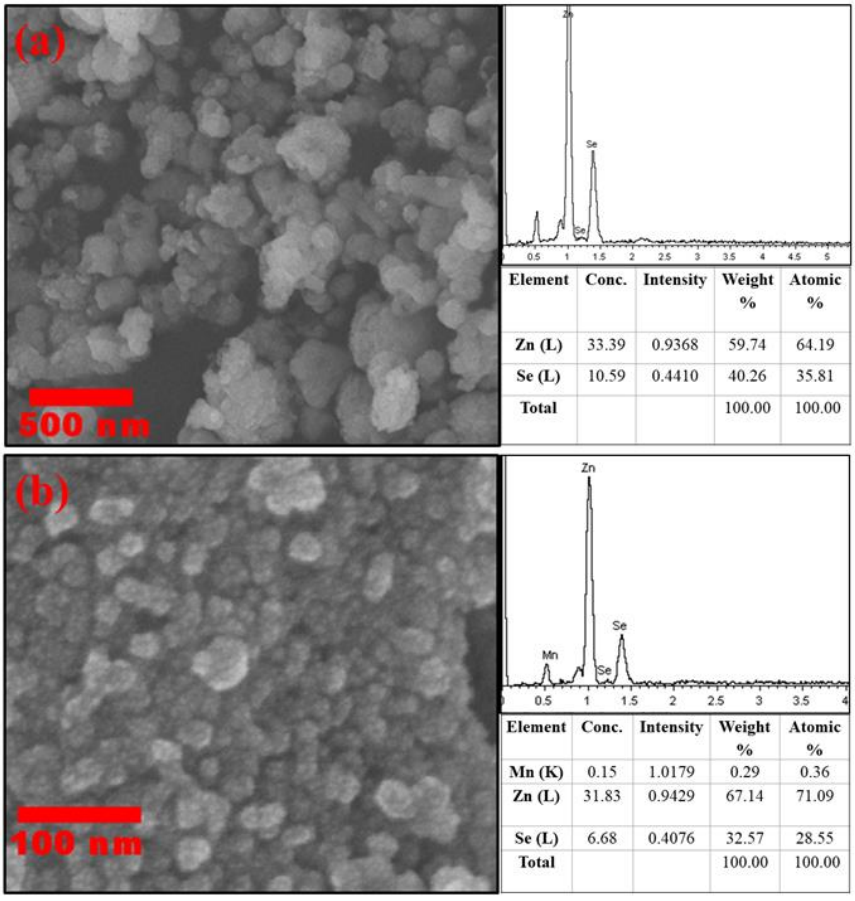

Element	Conc.	Intensity	Weight %	Atomic %
Zn (L)	33.39	0.9368	59.74	64.19
Se (L)	10.59	0.4410	40.26	35.81
Total			100.00	100.00

Element	Conc.	Intensity	Weight %	Atomic %
Mn (K)	0.15	1.0179	0.29	0.36
Zn (L)	31.83	0.9429	67.14	71.09
Se (L)	6.68	0.4076	32.57	28.55
Total			100.00	100.00

Figure 6.2. FE-SEM images of ZnSe and Mn@ZnSe QDs along with corresponding EDS spectra and elements composition.

The elemental composition of synthesized un-doped and Mn^{2+}-doped ZnSe nanoparticles was recorded by EDS linked to SEM, and the results are presented in Fig. 6.2 along with elements composition. The appearance of characteristic peaks of (Zn, Se, Mn) without any other foreign impurities in un-doped and Mn@ZnSe samples, conforming to the successful synthesis, purity and existence of appropriate doping in the doped samples.

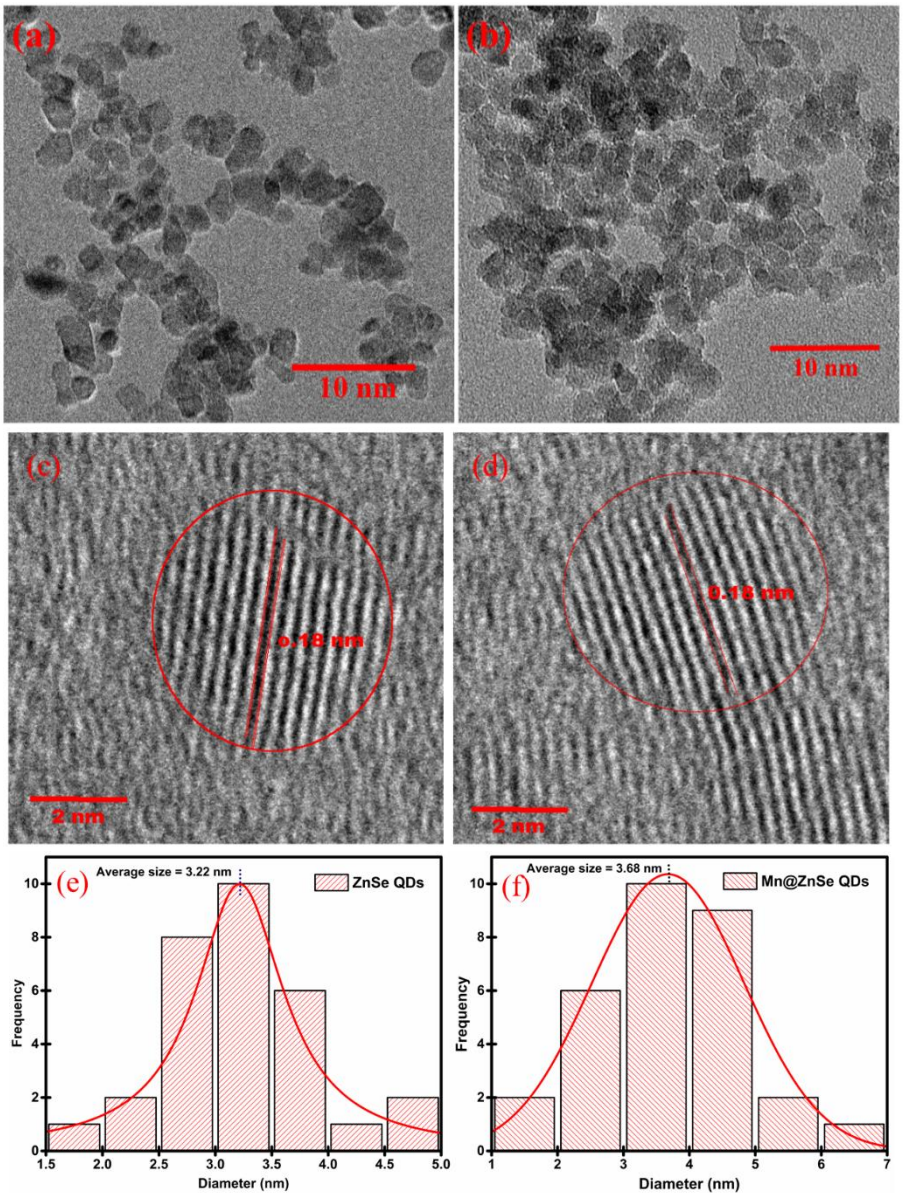

Figure 6.3. TEM images (a,b) and HRTEM images (c,d) of ZnSe and Mn@ZnSe QDs with corresponding size distribution histograms for ZnSe (e) and Mn@ZnSe QDs (f).

The extension of the morphological study was done by TEM imaging. The TEM images reveal more information about the size and morphology of synthesized ZnSe and Mn@ZnSe QDs, as illustrated in Fig. 6.3(a,b). The nanoparticles exhibited a nano-sphere-like shape with a uniformly dispersed distribution. The high-resolution TEM (HRTEM) images are represented in Figure 6.3(c,d). HRTEM images show the crystal lattice fringes with interplanar spacing 0.18 nm for both doped and undoped ZnSe QDs, which indicates that the Mn^{2+} ions doping doesn't affect the crystalline zinc blende structure of ZnSe. A slightly larger diameter was observed for Mn@ZnSe (3.7 nm) as compared to un-doped ZnSe QDs (3.2 nm), as shown with corresponding histograms of particle size distribution in Fig. 6.3(e,f).

The optical absorption and PL spectra of synthesized QDs were measured. The absorption spectra show the absorption bands in the visible region (320-440 nm), as represented in Fig. 6.4.

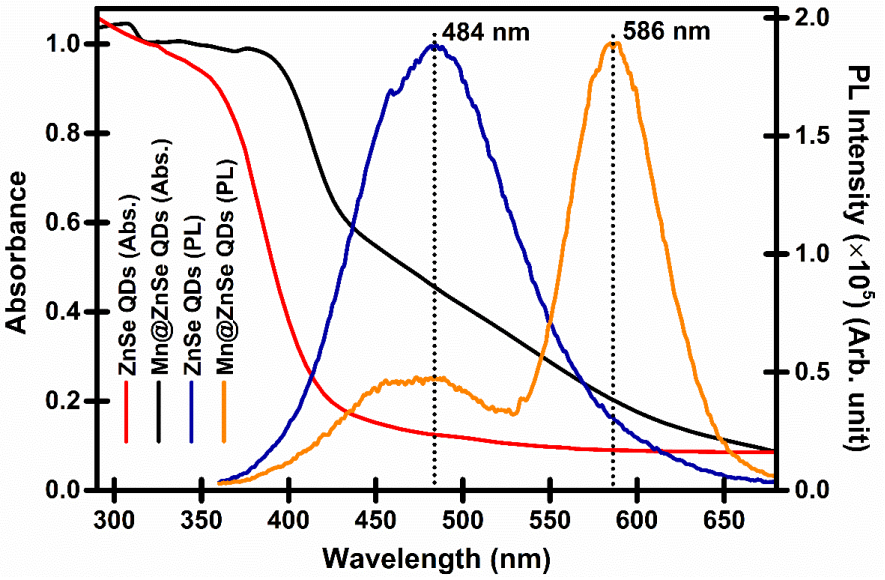

Figure 6.4. UV absorption and PL spectra of ZnSe (λ_{ex}, 350 nm) and Mn@ZnSe QDs (λ_{ex}, 370 nm) at room temperature.

The un-doped ZnSe QDs dispersed in DI water show band maximum at 360 nm, ascribed band to band transition of ZnSe. Mn@ZnSe QDs exhibit the absorption

maximum at 390 nm. If applied, the corresponding Tauc′s plots for direct transitions, are illustrated in Fig. 6.5.

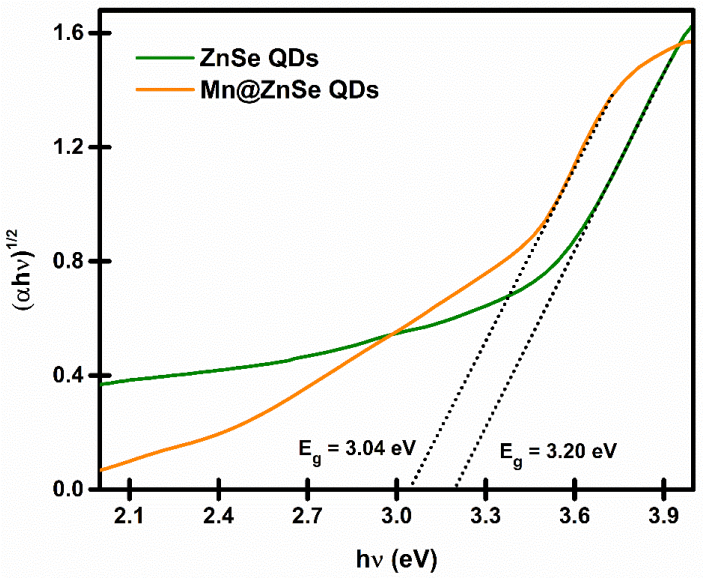

Figure 6.5. Tauc's plots for ZnSe and Mn@ZnSe QDs.

The optical bandgap (E_g) of prepared QDs has been roughly estimated from the Tauc′s Eq.,

$$\alpha h\nu = A\left(h\nu - E_g\right)^{\frac{1}{n}} \tag{6.2}$$

Here, A is the band tailing parameter, $h\nu$ is the energy of a photon, α is the absorption coefficient and n denotes the transition mode power factor, which depends upon the type of electronic transition, i.e., the value of n = 2 for direct transitions. The Tauc′s plot was plotted between $(\alpha h\nu)^2$ vs. $h\nu$ and the bandgap energy was calculated through extended the linear part of the curve. The estimated bandgaps are 3.04 and 3.20 eV for ZnSe and Mn@ZnSe QDs, respectively. However, the noted blue shift in the bandgap compared to the bulk ZnSe (2.73 eV) reflects the confinement effects in both un-doped and Mn^{2+}-doped ZnSe QDs. The PL spectra were measured with 350 and 370 nm excitation wavelengths for ZnSe and Mn@ZnSe QDs, respectively. Keeping the excitation energy higher than the forbidden gap of ZnSe. The PL spectrum of ZnSe

shows an intense blue emission at 484 nm corresponding to the existence of an extended amount of the surface traps states. The defects in ZnSe QDs are mainly the vacancy defects generated due to the lower Zn/Se ratio in preparation [31]. While the PL spectrum of Mn@ZnSe QDs consists of the dual-band at 480 and 586 nm corresponding to the ZnSe host and intense orange emission due to Mn^{2+} d-level $^4T_1$ to $^6A_1$ transitions, respectively [32-33]. The slight ZnSe trap states emission detected in PL of Mn@ZnSe QDs may be ascribed to the high doping of Mn^{2+} ions and the energy transfer from host to dopant, which suppressed the PL of ZnSe in Mn@ZnSe QDs. The observed Stokes shift is about 94 nm, which is too large for direct excitonic recombination. The large Stokes shift also points out the presence of unconventional in-gap states, i.e., the traps or defect-related states. The quantum yields of synthesized ZnSe and Mn@ZnSe QDs were also calculated at room temperature by using Quinine sulfate as a reference and comes out to be 16 ± 2 and 37 ± 4%, respectively.

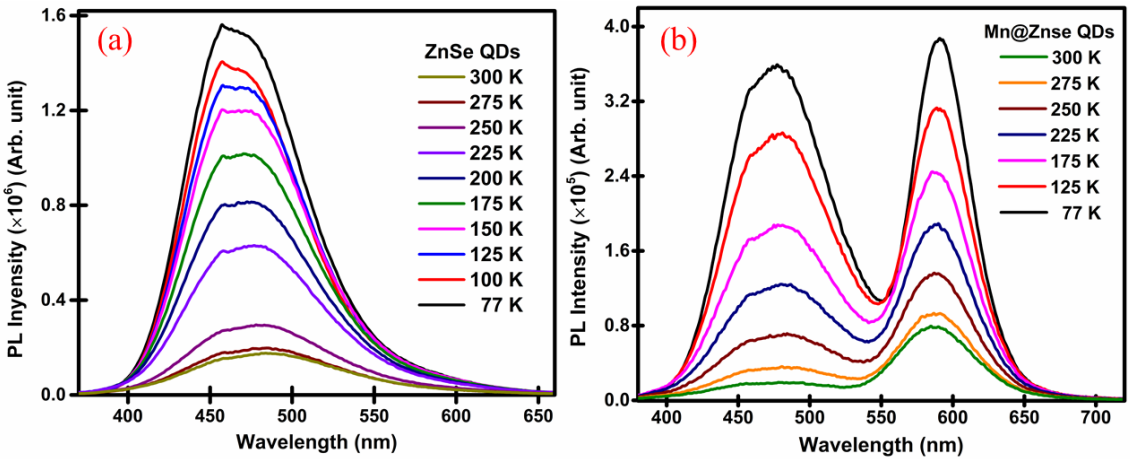

Figure 6.6. The temperature-dependent photoluminescence spectra of ZnSe (a) and Mn@ZnSe QDs (b) in the 300 - 77 K range. The excitation wavelengths were 350 nm and 370 nm for ZnSe and Mn@ZnSe QDs, respectively.

The temperature-dependent PL spectrum was analyzed to explore the non-radiative relaxation processes in the system. The immobilized solid powdered QDs were used in

a 1×10 mm dimensional quartz cuvette to record the temperature-dependent PL. To lower the temperature, liquid nitrogen-based cryostat was used in all the measurements. The cryostat temperature was accurately monitored between 300 to 77 K and achieved a strong fluorescence. Fig. 6.6(a,b) illustrates that the temperature-dependent PL spectra of ZnSe and Mn@ZnSe QDs with 350 and 370 nm excitations, which are strongly depend on the temperature. This indicates that the defect traps which are remarkably present on the surface of synthesized QDs becomes thermally activate and promotes the numerous relaxation paths with the rising temperature. With the increasing temperature, the radiative recombination of electrons with Se vacancies (*i.e.,* holes) in ZnSe QDs, i.e., the surface trap PL at 480 nm, decreases due to the thermal instability of these surfaces defects. While, in Mn@ZnSe QDs, both the Mn^{2+} and ZnSe host-related PL at 584 and 480 nm, respectively, shows quenching with temperature. This indicates that the surface defect states are efficiently active even after the doping because of the deep implantation of Mn^{2+} ions in host ZnSe in nucleation doping strategy, i.e., nucleation doping does′t affect the surface. "According to Fang et al., dopant emission is only observed when the dopant ions were incorporated into the lattice instead of being attached to the outer surface [34,35]. The occurrence of a new PL band and the enhancement of host ZnSe lattice emission shows the successful incorporation of Mn^{2+} in ZnSe lattice of Mn@ZnSe QDs." Also, no blue or red shift was observed in PL with decreasing temperature, suggesting that no lattice contraction occurred at a lower temperature in ZnSe and Mn@ZnSe QDs [36].

Change in PL intensity at peak maximum with varying temperature from 77 to 275 K of ZnSe and Mn@ZnSe QDs was plotted as shown in Fig. 6.7(a,b). The plots show the linearly dependent behavior of PL intensity with the temperature over the wide range.

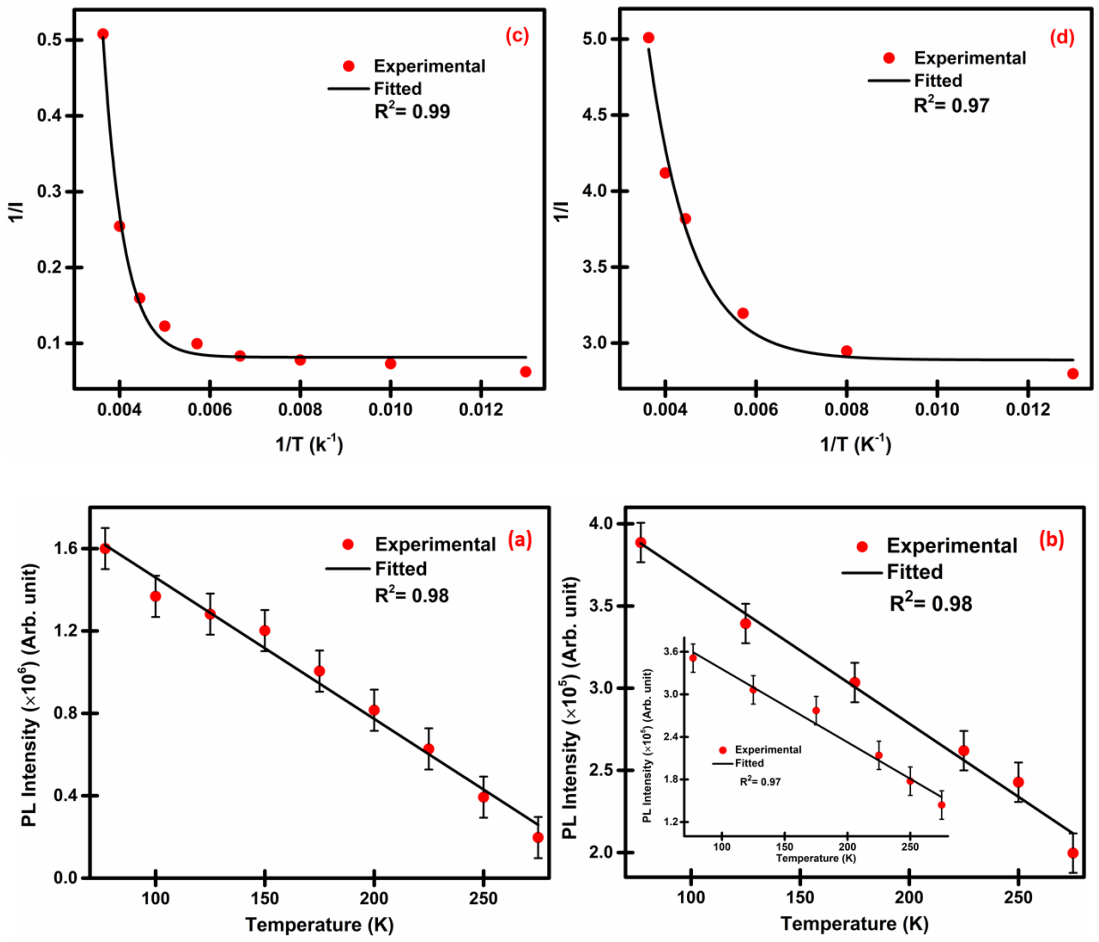

Figure 6.7. The photoluminescence intensity variation with temperature and Arrhenius plot of ZnSe (a,c) and Mn@ZnSe QDs (b,d). The inset of Fig. (b) shows PL intensity variation with temperature for the host-related band in Mn@ZnSe QDs.

The inset of Fig. 6.7(b) shows the PL intensity variation with temperature for host-related band (at 480 nm) in Mn@ZnSe QDs, which may be further used in designing a ratio-metric sensor for better sensitivity and reliability. The linearity over the wide temperature range suggests that developed samples could be utilized as temperature sensing probes.

In this direction, we further investigated our prepared samples to understand better temperatures effects and mechanism of decreasing PL intensity with increasing temperature. Fig. 6.7(c,d) shows the plots between 1/I and 1/T of ZnSe and Mn@Znse QDs, respectively, for the calculation of thermal activation energy (E_a), where red dots

represent the experimental data, and the solid line is the fitted curve using Arrhenius Eq. (3) [37-38].

$$I(T) = I_0 \left[1 + A\exp\left(-\frac{E_a}{k_B T}\right)\right]^{-1} \quad (6.3)$$

Here, I_0 and I(T) denoted the maximum PL intensity at temperatures 0 and T (K), respectively. A represents the radiative lifetime-dependent constraint. K_B is a well-known Boltzmann constant. The calculated activation energy values for ZnSe and Mn@ZnSe QDs come out to be 42.2 meV and 66.4 meV, respectively. The obtained moderate activation energy for both samples are favorable for casting temperature sensor.

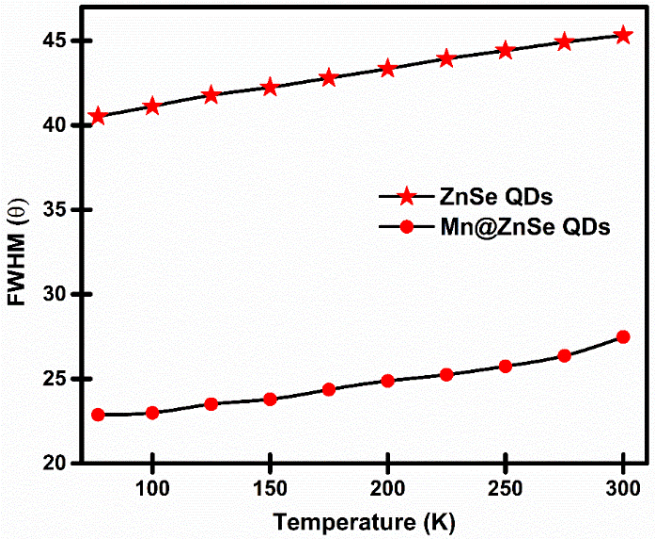

Figure 6.8. The variation of FWHM with increasing temperature of ZnSe and Mn@ZnSe QDs.

Furthermore, the slight change in the full-width half maxima (FWHM) and PL peak position of ZnSe and Mn@ZnSe QDs was observed with temperature, which shows that the FWHM is temperature independent for our ZnSe and Mn@ZnSe system, as shown in Fig. 6.8. The variation or broadening of FWHM of temperature-dependent PL can be explained by Eq. (4) [39].

$$\beta(T) = \beta_{inh} + \sigma T + \beta_{LO}\left[\exp\left(\frac{E_{LO}}{K_B T}\right) - 1\right]^{-1} \quad (6.4)$$

Here, the first term β_{inh} represents the inhomogeneous broadening which is a temperature-independent variable. β_{LO} denoted the extend of exciton-longitudinal optical (LO) phonon coupling while the E_{LO} represents the LO-phonon energy. σ signifies the electron-acoustic phonon coupling coefficient. According to Eq. (4), the negligible broadening or temperature-independent behavior of FHWM suggests that phonon coupling is weak, and the electron-electron scattering dominates in ZnSe and Mn@ZnSe QDs.

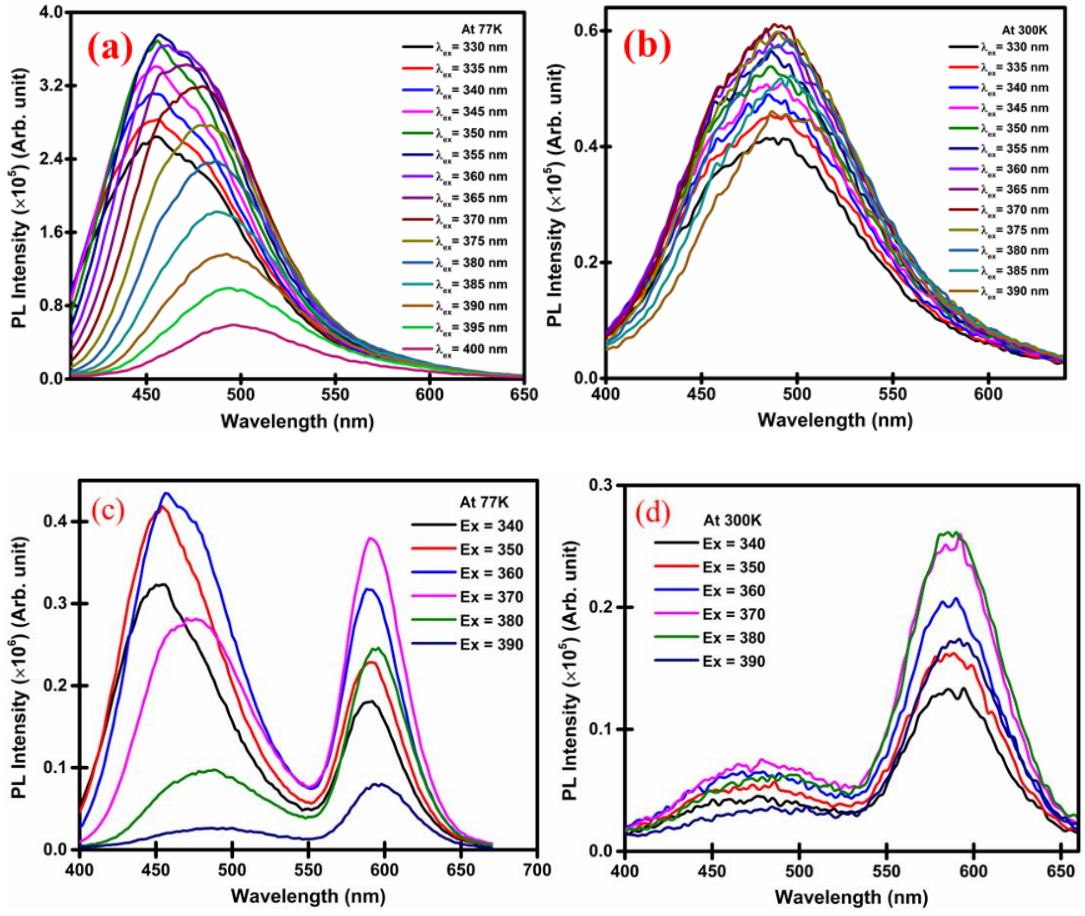

Figure 6.9. The PL spectra of ZnSe QDs at 77 K (a) and 300 K (b) and PL of Mn@ZnSe QDs at 77 K (c) and 300 K (d) with different $\lambda_{ex.}$

Furthermore, the PL of the ZnSe QDs shifts towards the longer wavelength extending from 450 to 500 nm with an increasing excitation wavelength as of 330 to

400 nm at a low temperature of 77 K, shown in Fig. 6.9(a). However, with the rise of measuring temperature from 77 to 250 K, shifting in PL decreases, and at room temperature (300 K), no shifting was observed, as shown in Fig. 6.9(b).

The excitation-dependent PL behavior mainly triggers functional groups (-SH, -OH) on the surface of QDs, which affects the trapping states and results in multiple emission centers [40]. These additional emitting states are highly dependent on temperature, as defined in Eq. 4. Therefore, shifting in PL is different at different temperatures. In Mn@ZnSe QDs, the ZnSe host-related peak shows a similar behavior as shown in Fig. 6.9(c,d), but no such shifting was observed in the Mn^{2+} dopant-related PL band. Because the Mn^{2+} transition is originated following energy transfer from ZnSe to Mn^{2+} ion centers and is an independent excitation phenomenon.

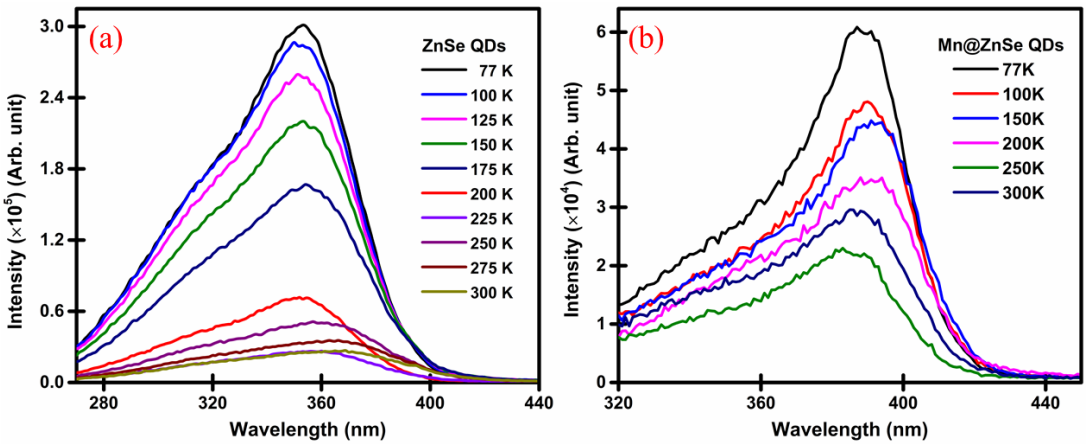

Figure 6.10. The PL excitation spectra of ZnSe QDs (a) and Mn@ZnSe QDs (b) at different temperatures.

The PLE spectra of ZnSe and Mn@ZnSe QDs at different temperatures are illustrated in Fig. 6.10. The PLE spectra of ZnSe and Mn@ZnSe QDs do not show any shifting with varying temperatures. Furthermore, the PLE spectra of ZnSe and Mn@ZnSe QDs show the shifting with the variation of PL wavelength (Fig. 6.11). The PLE spectra of Mn@ZnSe QDs obtained at λ_{em}= 470 and 590 nm were reproduced with (G_{A1}, G_{A2}) and (G_{B1}, G_{B2}) Gaussian bands. The PLE spectra of Mn@ZnSe QDs

show two excitation wavelengths at 350 and 370 nm related to the ZnSe host and Mn^{2+} dopant, respectively, as represented in Fig. 6.11(b). The PL wavelength-dependent PLE spectra also confirm multiple emission centers due to the surface functional or ligand groups.

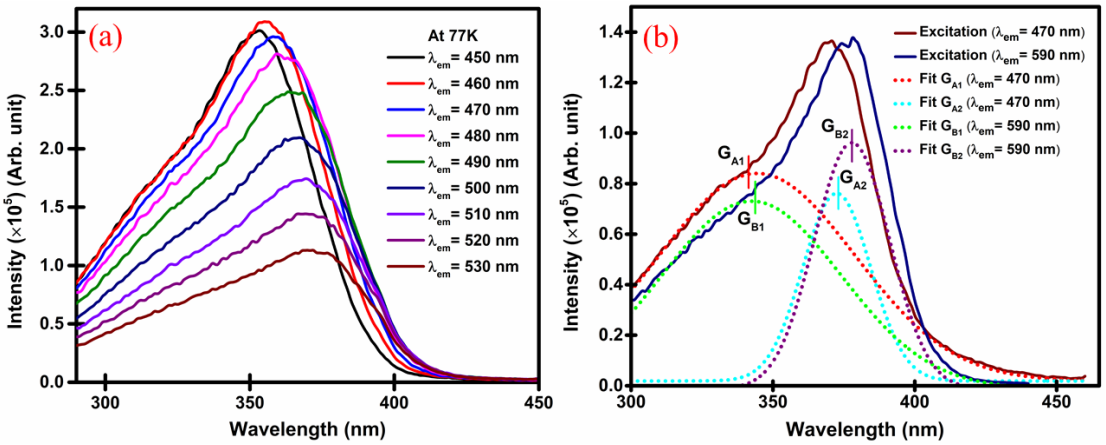

Figure 6.11. The PLE spectra of ZnSe QDs at different λ_{em} (a) and PLE spectra of Mn@ZnSe QDs at λ_{em}= 470 and 590 nm (b) corresponding to ZnSe host and Mn-dopant related bands, respectively, at a fixed temperature of 77 K. The PLE spectra at λ_{em}= 470 and 590 nm were reproduced with G_{A1}, G_{A2}, G_{B1} and G_{B2} Gaussian bands.

The PL lifetime of ZnSe QDs was recorded at room temperature and PL and excitation wavelengths were 480 nm and 340 nm, respectively. The lifetime curve is represented in Figure 9(a). The average lifetime of ZnSe QDs comes out to be 87.45 ns. While the temperature-dependent PL lifetime curves of Mn@ZnSe QDs were recorded in the temperature range from 300 to 77 K and are illustrated in Fig. 6.12. The acquired decay curves are well fitted with the bi-exponential decay function. The bi-exponential function used in the simulation of the decay curve is given by the following equation [41-42].

$$f(t) = \sum_i A_i \exp\left(-\frac{t}{\tau_i}\right), \quad (1)$$

where A_i, τ_i are represent the pre-exponential factors and lifetime components, respectively. The average lifetime (τ_{av}) is calculated from the following equation [43,44],

$$\tau_{av} = \sum_i \frac{A_i \tau_i^2}{A_i \tau_i}, \quad (2)$$

The extracted lifetimes and calculated average lifetimes are summarized in Table 6.1. The average lifetime becomes longer, increases from 0.455 to 0.637 ms, by lowering the temperature from 300 to 77 K.

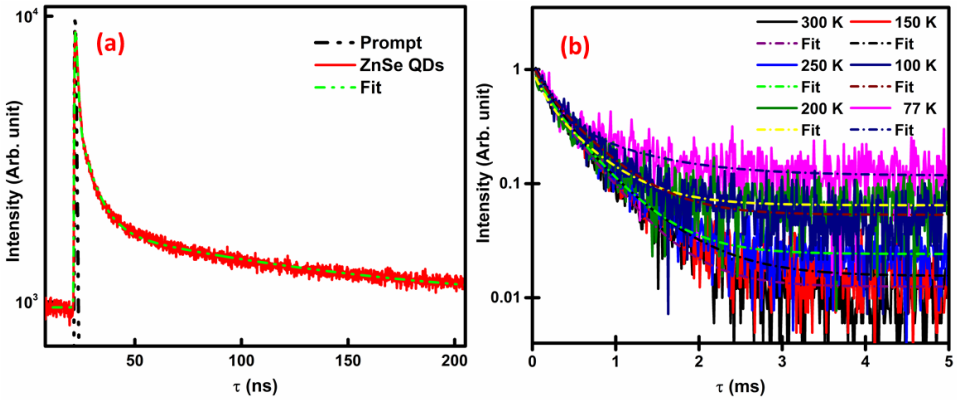

Figure 6.12. The fitted decay curves of ZnSe (a) at room temperature and Mn@ZnSe QDs (b) at different temperatures (300 to 77 K).

In the bi-exponential fit, the longer lifetime component might be assigned to the deep trap states, which are lower in energy. While the short lifetime component may assign to the shallow traps, which lie above the deep traps, thus having higher energy. This can also be understood by concerning the thermal energy effect; with varying temperatures, the thermal population of energy states significantly varies from the normal population instantly after excitation because of the decreased thermal relaxation rates in QDs. In this manner, at lower temperatures, the states will experience a higher population and increase recombination rates, thus the lifetime [45]. Furthermore, the variation and increases in the lifetimes at a lower temperature are due to different emitting centers that exhibit excitation-dependent PL and PL-dependent PLE.

Table 6.1. The lifetimes and pre-exponential factors of Mn@ZnSe QDs at low temperatures. PL and excitation wavelengths were 580 nm and 370 nm, respectively.

Temperature (K)	τ_1 (ms)	τ_2 (ms)	α_1	α_2	τ_{av} (ms)
300	0.093 ± 0.011	0.455 ± 0.010	0.33	0.67	0.455
250	0.106 ± 0.013	0.475 ± 0.013	0.34	0.66	0.475
200	0.138 ± 0.040	0.504 ± 0.046	0.39	0.61	0.504
150	0.218 ± 0.019	0.587 ± 0.045	0.57	0.43	0.521
100	0.114 ± 0.039	0.510 ± 0.028	0.27	0.73	0.550
77	0.207 ± 0.036	0.867 ± 0.218	0.71	0.29	0.637

For a better temperature sensor, a wide range of temperatures and high sensitivity are required. The synthesized samples show a wide range of temperatures (77 - 275 K). Further, the absolute sensitivity (S) and the relative sensitivity (S_R) for temperature sensing are estimated using Eqs. 5 and 6.

$$S = \frac{d[I(T)/I_0]}{dT} \tag{6.5}$$

$$S_R = S\frac{I_0}{I(T)} \tag{6.6}$$

The variation in S and S_R for ZnSe and Mn@ZnSe QDs with increasing temperature in the range 77 to 250 K are shown in Fig. 6.13. Here, the sensitivity represents the percentage change in PL intensity with a unit change in temperature. The maximum value of sensitivity calculated comes out to be 0.58 % K^{-1} at 225 K and 0.44 % K^{-1} at 250 K for ZnSe and Mn@ZnSe QDs, respectively. The relative sensitivity shows the maximum values 1.99 % K^{-1} and 0.71 % K^{-1} at 250 K for ZnSe and Mn@ZnSe QDs, respectively. Calculating relative sensitivity over absolute sensitivity is essential

because it reduces unwanted variations due to the excitation radiation and fluctuations in the measurement circumstances or environment.

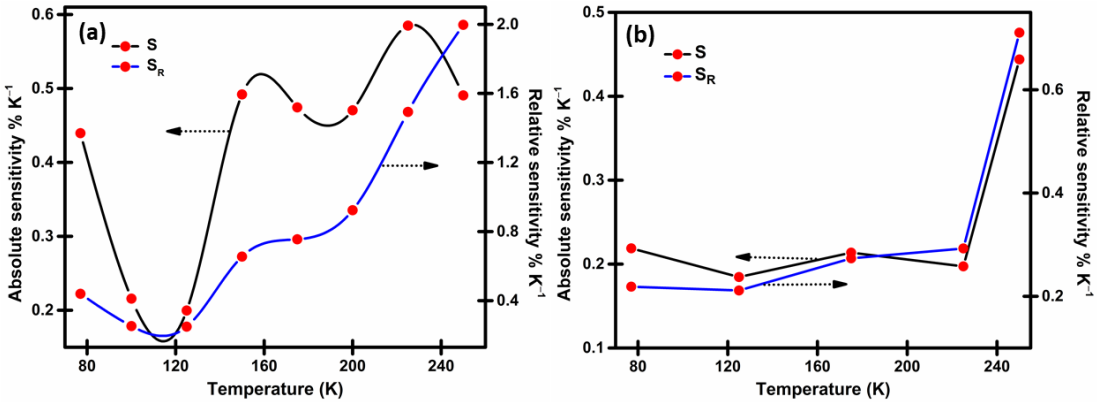

Figure 6.13. The absolute and relative sensitivity (percentage) as a function of temperature for ZnSe (a) and Mn@ZnSe (b) QDs.

Table 6.2. Comparison of synthesized ZnSe and Mn@ZnSe QDs as a temperature sensor with other reported QDs.

QDs	Size (nm)	λ_{em} (nm)	T range (K)	S (% k^{-1})	Reference
ZnSe, Mn@ZnSe	3.2, 3.6	484, 586	77-275	0.58, 0.44	This work
ZnS:Mn^{2+}	10	589	303-423	0.5	37
(CdSe)ZnS	5-5.5	540-660	278-313	1.3	38
CdSe	1.8	462, 565	82-280	0.69	39
CDs	2.6	471	288-363	-	24
CdTe	2.3	571, 652	80-360	0.70	40
PbS/CdS/CdSe	5.4	670, 910	180-300	1.22	41

The above results and findings suggest that the prepared ZnSe and Mn@ZnSe QDs are favorable for utilized as PL-intensity-based wide range (77 to 275 K) optical temperature sensors with good sensitivity as compared to other reported thermal sensors [46-48]. The comparison with other reported QDs is given in Table 6.2.

In terms of sensitivity, ZnSe QDs shows better results, but this can be overcome in Mn@ZnSe QDs by considering the ratio-metric sensing using relative PL intensity of both emission peaks. The schematic representation of testing the sensor and record the temperature sensing measurements is shown in Fig. 6.14.

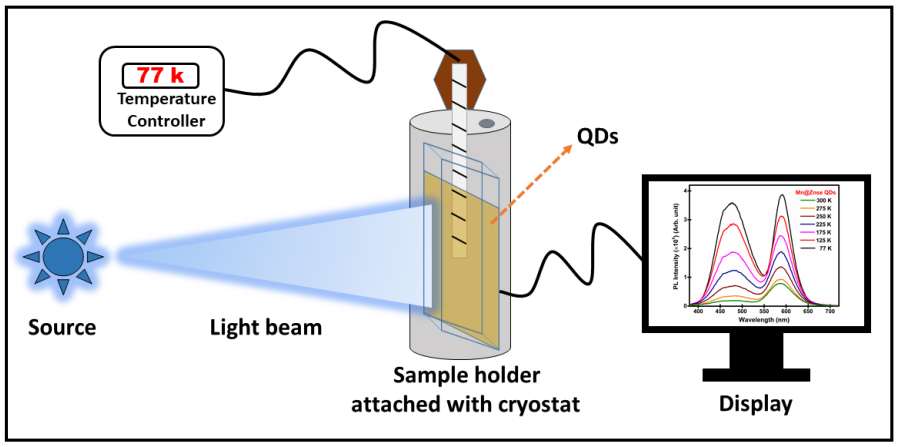

Figure 6.14. Schematic representation of testing and recording of the sensing measurements of the proposed optical temperature sensor.

6.4. Conclusions

We report a parallel low-temperature investigation of ZnSe and Mn@ZnSe QDs using temperature-dependent PL and PLE studies at different excitation and emission wavelengths. The PL intensity with increasing temperature shows linearity over 77 to 275 K and is well fitted using the Arrhenius equation. The estimated activation energy values are 42.2 meV and 66.4 meV for ZnSe and Mn@ZnSe QDs, respectively. The activation energy in the 40-70 meV range provides better temperature effects and is suitable for casting as an optical temperature sensor. The proposed sensing probes offer good sensitivity over the full range of temperature. The maximum absolute sensitivity is 0.58 % K^{-1} at 225 K and 0.44 % K^{-1} at 250 K for ZnSe and Mn@ZnSe QDs, respectively. Furthermore, our findings and study offer beneficial understandings of the optical properties of ZnSe and Mn@ZnSe QDs, which may be promoting their future applications in optoelectronic devices.

References

[1] J.Z. Zhang, Optical properties and spectroscopy of nanomaterials, World Scientific Publishing Co Pte Ltd, (2009) 383.

[2] Y. Pei, X.C. Zeng, Investigating the structural evolution of thiolate protected gold clusters from first-principles, Nanoscale. 4 (2012) 4054–4072.

[3] Y. Nandan, M.S. Mehata, Wavefunction engineering of type-I/type-II excitons of CdSe/CdS core-shell quantum dots, Sci. Rep. 9 (2019) 2.

[4] P. Sharma, M.S. Mehata, Colloidal MoS_2 quantum dots based optical sensor for detection of 2,4,6-TNP explosive in an aqueous medium, Opt. Mater. 100 (2020) 2–6.

[5] Z. Pan, Photoluminescence of Er-doped ZnO nanoparticle films via direct and indirect excitation, J. Nanophotonics. 6 (2012) 063508.

[6] A.F. Zatsepin, D.Y. Biryukov, The temperature behavior and mechanism of exciton luminescence in quantum dots, Phys. Chem. Chem. Phys. 19 (2017) 18721–18730.

[7] M.N. Nordin, J. Li, S.K. Clowes, R.J. Curry, Temperature dependent optical properties of PbS nanocrystals, Nanotechnology. 23 (2012).

[8] D.Y. Biryukov, A.F. Zatsepin, Analytical temperature dependence of the photoluminescence of semiconductor quantum dots, Phys. Solid State. 56 (2014) 635–638.

[9] A.N. Reznitsky, A.A. Klochikhin, S.A. Permogorov, Temperature dependence of photoluminescence intensity of self-assembled CdTe quantum dots in the ZnTe matrix under different excitation conditions, Phys. Solid State. 54 (2012) 123–133.

[10] M. Kapoor, G. Johri, V.A. Singh, Origin of the anomalous temperature

dependence of luminescence in semiconductor nanocrystallites, Phys. Rev. B - Condens. Matter Mater. Phys. 61 (2000) 1941–1945.

[11] Y.D. Glinka, S.H. Lin, L.P. Hwang, N.H. Tolk, Size effect in self-trapped exciton photoluminescence from SiO2-based nanoscale materials, Phys. Rev. B - Condens. Matter Mater. Phys. 64 (2001) 854211–8542111.

[12] Y.D. Glinka, S.H. Lin, Y.T. Chen, Time-resolved photoluminescence study of silica nanoparticles as compared to bulk type-III fused silica, Phys. Rev. B - Condens. Matter Mater. Phys. 66 (2002) 354041–3540410.

[13] C. de Mello Donegá, Synthesis and properties of colloidal heteronanocrystals, Chem. Soc. Rev. 40 (2011) 1512–1546.

[14] H. Zhao, R. Sun, Z. Wang, K. Fu, X. Hu, Y. Zhang, Zero-dimensional perovskite nanocrystals for efficient luminescent solar concentrators, Adv. Funct. Mater. 29 (2019) 1902262.

[15] H. Zhaoa, D. Benettib, X. Tongb, H. Zhangb, Y. Zhoub, G. Liua, D. Mab, S. Sunb, Z. M. Wangc, Y. Wanga, F. Rosei, Efficient and stable tandem luminescent solar concentrators based on carbon dots and perovskite quantum dots, Nano Energy 50 (2018) 756–765.

[16] V. Wood, M.J. Panzer, J. Chen, M.S. Bradley, J.E. Halpert, M.C. Bawendi, V. Bulović, Inkjet-printed quantum dot-polymer composites for full-color AC-driven displays, Adv. Mater. 21 (2009) 2151–2155.

[17] M.S. Mehata, R.K. Ratnesh, Luminescence properties and exciton dynamics of core-multi-shell semiconductor quantum dots leading to QLEDs, Dalt. Trans. 48 (2019) 7619–7631.

[18] P. Sharma, M.S. Mehata, Rapid sensing of lead metal ions in an aqueous medium by MoS_2 quantum dots fluorescence turn-off, Mater. Res. Bull. 131 (2020)

110978.

[19] X. Peng, L. Manna, W. Yang, J. Wickham, E. Scher, A. Kadavanich, A.P. Alivisatos, Shape control of CdSe nanocrystals, nature. 404 (2000) 59–61.

[20] R.K. Ratnesh, M.S. Mehata, Investigation of biocompatible and protein sensitive highly luminescent quantum dots/nanocrystals of CdSe, CdSe/ZnS and CdSe/CdS, Spectrochim. Acta - Part A Mol. Biomol. Spectrosc. 179 (2017) 201–210.

[21] M.S. Mehata, Enhancement of charge transfer and quenching of photoluminescence of capped CdS quantum dots, Sci. Rep. 5 (2015) 12056.

[22] S. Balabhadra, M.L. Debasu, C.D. Brites, L.A. Nunes, O.L. Malta, J. Rocha, M. Bettinelli, L.D. Carlos, Boosting the sensitivity of Nd3+-based luminescent nanothermometers, Nanoscale, 7 (2015) 17261-17267.

[23] J. Rocha, C.D.S Brites, L.D. Carlos. Lanthanide organic framework luminescent thermometers. Chem. Eur. J., 22 (2016) 14782-14795.

[24] G. Kucsko, P.C. Maurer, N.Y. Yao, M. Kubo, H.J. Noh, P.K. Lo, H. Park, M.D. Lukin, Nanometre-scale thermometry in a living cell, nature, 500 (2013) 54-58.

[25] Y. Yue, X. Wang, Nanoscale thermal probing, Nano Rev. 3 (2012).

[26] C. Wang, Z. Xu, H. Cheng, H. Lin, M.G. Humphrey, C. Zhang, A hydrothermal route to water-stable luminescent carbon dots as nanosensors for pH and temperature, Carbon, 82 (2015) 87-95.

[27] X.D. Wang, O.S. Wolfbeis, R.J. Meier, Luminescent probes and sensors for temperature, Chem. Soc. Rev, 42 (2013) 7834-7869.

[28] C.D. Brites, P.P. Lima, N.J. Silva, A. Millan, V.S. Amaral, F. Palacio, L.D. Carlos, Thermometry at the nanoscale, Nanoscale, 4 (2012) 4799-4829.

[29] R. Liang, R. Tian, W. Shi, Z. Liu, D. Yan, M. Wei, D.G. Evans, X. Duan, A

temperature sensor based on CdTe quantum dots-layered double hydroxide ultrathin films via layer-by-layer assembly, Chem. Commun. 49 (2013) 969-971.

[30] V. Biju, Y. Makita, A. Sonoda, H. Yokoyama, Y. Baba, M. Ishikawa, Temperature-sensitive photoluminescence of CdSe quantum dot clusters, J. Phys. Chem. B, 109 (2005) 13899-13905.

[31] D. Denzler, M. Olschewski, K. Sattler, Luminescence studies of localized gap states in colloidal ZnS nanocrystals, J. Appl. Phys. 84 (1998) 2841–2845.

[32] S. Acharya, D.D. Sarma, N.R. Jana, N. Pradhan, An alternate route to high-quality ZnSe and Mn-doped ZnSe nanocrystals, J. Phys. Chem. Lett. 1 (2010) 485–488.

[33] C. Wang, X. Gao, Q. Ma, X. Su, Aqueous synthesis of mercaptopropionic acid capped Mn^{2+}-doped ZnSe quantum dots, J. Mater. Chem. 19 (2009) 7016–7022.

[34] N. Pradhan, D.M. Battaglia, Y. Liu, X. Peng, Efficient, stable, small, and water-soluble doped ZnSe nanocrystal emitters as non-cadmium biomedical labels, Nano Lett. 7 (2007) 312–317.

[35] Z. Fang, P. Wu, X. Zhong, Y.-J. Yang, Synthesis of highly luminescent Mn:ZnSe/ZnS nanocrystals in aqueous media, Nanotechnology. 21 (2010) 305604-305612.

[36] S. Mahamuni, A.D. Lad, S. Patole, Photoluminescence properties of manganese-doped zinc selenide quantum dots, J. Phys. Chem. C 112 (2008) 2271−2277.

[37] Q. Li, Y. Zheng, X. Hou, T. Yang, T. Liang, J. Zheng, A wide range photoluminescence intensity-based temperature sensor developed with BN quantum dots and the photoluminescence mechanism, Sens. Actuators B Chem. 304 (2020) 127353.

[38] D. Das, S. L. Shinde, K. K. Nanda, Temperature-dependent photoluminescence

of g-C3N4: implication for temperature sensing, ACS Appl. Mater. Interfaces. 8 (2016) 2181-2186.

[39] C. Ji, Y. Zhang, T. Zhang, W. Liu, X. Zhang, H. Shen, Y. Wang, W. Gao, Y. Wang, J. Zhao, W.W. Yu, Temperature-dependent photoluminescence of Ag_2Se quantum dots, J. Phys. Chem. C, 119 (2015) 13841-13846.

[40] S. Kim, B.K. Yoo, Y. Choi, B.S. Kim, O.H. Kwon, Time-resolved spectroscopy of the ensembled photoluminescence of Nitrogen- and Boron/Nitrogen-doped carbon dots, Phys. Chem. Chem. Phys., 20 (2018) 11673-11681.

[41] M.K. Singh, M.S. Mehata, Enhanced photoinduced catalytic activity of transition metal ions incorporated TiO_2 nanoparticles for degradation of organic dye: Absorption and photoluminescence spectroscopy, Opt. Mater. 109 (2020) 110309.

[42] M.K. Singh, M.S. Mehata, Temperature-dependent photoluminescence and decay times of different phases of grown TiO_2 nanoparticles: Carrier dynamics and trap states, Ceram. Int. 47 (2021) 32534-32544.

[43] V. Sharma, M.S. Mehata, Synthesis of photoactivated highly fluorescent Mn^{2+}-doped ZnSe quantum dots as effective lead sensor in drinking water, Mater. Res. Bull. 134 (2021) 111121.

[44] V. Sharma, M.S. Mehata, Rapid optical sensor for recognition of explosive 2,4,6-TNP traces in water through fluorescent ZnSe quantum dots, Spectrochim. Acta-Part A Mol. Biomol. Spectrosc. 260 (2021) 119937.

[45] J. Eilers, J. Hest, A. Meijerink, C. Donega, Unravelling the size and temperature dependence of exciton lifetimes in colloidal ZnSe quantum dots. J. Phys. Chem. C. 118 (2014) 23313-23319.

[46] H. Zhang, J. Liu, C. Wang, G. S. Selopal, D. Barba, Z. M. Wang, S. Sun, H.

Zhao, F. Rosei, Near-infrared colloidal manganese-doped quantum dots: Photoluminescence mechanism and temperature response, ACS Photonics 2019, 6, 2421−2431.

[47] J. Liu, H. Zhang, G. S. Selopal, S. Sun, H. Zhao, F. Rosei, Visible and near-infrared, multiparametric, ultrasensitive nanothermometer based on dual-emission colloidal quantum dots, ACS Photonics 2019, 6, 2479−2486.

[48] R. Wang, X. Tong, A. I. Channa, Q. Zeng, J. Sun, C. Liu, X. Li, J. Xu, F. Lin, G. S. Selopal, F. Rosei, Y. Zhang, J. Wu, H. Zhao, A. Vomiero, X. Sun, Z. M. Wang, Environment-friendly Mn-alloyed core/shell quantum dots for high-efficiency photoelectrochemical cells, J. Mater. Chem. A, 2020,8, 10736-10741.

[49] S. Wang, S. Westcott, W. Chen, Nanoparticle luminescence thermometry, J. Phys. Chem. B, 106 (2002) 11203-11209.

[50] G.W. Walker, V.C. Sundar, C.M. Rudzinski, A.W. Wun, M.G. Bawendi, D.G. Nocera, Quantum-dot optical temperature probes, Appl. Phys. Lett. 83 (2003) 3555–3557.

[51] L. Jethi, M.M. Krause, P. Kambhampati, Toward ratiometric nanothermometry via intrinsic dual emission from semiconductor nanocrystals, J. Phys. Chem. Lett. 6 (2015) 718–721.

[52] S. Kalytchuk, O. Zhovtiuk, S. V. Kershaw, R. Zbořil, A.L. Rogach, Temperature-dependent exciton and trap-related photoluminescence of CdTe quantum dots embedded in a NaCl matrix: Implication in thermometry, Small. 12 (2016) 466–476.

[53] J. Liu, H. Zhang, G.S. Selopal, S. Sun, H. Zhao, F. Rosei, Visible and near-infrared, multiparametric, ultrasensitive nanothermometer based on dual-emission colloidal quantum dots, ACS Photonics. 6 (2019) 2479–2486.

Chapter 7

Exciton Dynamics of Light-Emitting Metal Incorporated Zinc-Selenide (ZnSe) Quantum Dots for Possible White QLEDs

7.1. Introduction

In the past few decades, generation of white light from low dimensional semiconductor nanomaterials or quantum dots (QDs) attracts researchers, especially in substituting the traditional light sources to achieve reduced energy loss and cost by lowering vitality costs and diminish overall utilization of lighting [1-5]. The old methods of generating the white light are based on solid-state white light emitters, which are neither designed by applying a coating or thin film on yellow phosphor or by making a combination of green and red phosphors based on the blue light-emitting diode. These configurations have drawbacks like self-absorption due to small bandgap, scattering at the phosphor layer's boundaries or edges, and unwanted non-radiative energy transfer (ET) between the emitters. Thus, semiconductor quantum dots (QDs) have received significant consideration because of their unique size adjustable characteristics as a result of quantum confinement and several possible applications like in light-emitting diodes (LEDs), laser technology, biological science, sensors, solar cells, etc. [6-10]. As from the II-VI NPs, cadmium (Cd) based compounds such as CdS, CdSe, CdTe, or core/shell structures CdSe/ZnS are toxic and harmful to human health. Therefore, zinc (Zn) compounds like ZnSe, ZnTe and ZnS, etc., as an alternative to Cd compounds, have received tremendous attention in many applications. Zinc-selenide (ZnSe) is a light-yellow solid intrinsic semiconductor, which emits light in the UV-Vis spectral region

[*] *Content of this chapter is communicated for publication.*

with a direct wide-bandgap of about 2.70 eV [11-16] shows less toxicity, lower absorption coefficient, and higher luminescence efficiency. Due to these properties, ZnSe becomes a favorable alternative in particular for light-generating applications and biological purposes.

The optical properties of ZnSe QDs could be modified by incorporating the metal ions impurities in the host. The photoluminescence (PL) spectra of ZnSe QDs lies between 390-440 nm. The emission peak of ZnSe could be adequately tuned typically through the addition of Cu^{2+} ions impurities. The doping of Cu^{2+} ions promoted by continuous reflux shows the red-shifted emission from 435 to 465 nm depending upon Cu ions and the traps states concentrations. On the other hand, Mn-doped ZnSe shows dual-band PL [17-18]. A predominant orange-yellow emission existed near 580 nm in an Mn-doped ZnSe framework, which came out due to the $^4T_1$–$^6A_1$ transitions of the Mn impurities and produced by the energy transfer process from the lattice of the host particle [19-22]. Pure and metal ions incorporated QDs can be synthesized by adopting various synthesis methods such as organic high-temperature synthesis, chemical precipitation, hot injection, solid-state reaction and solvothermal techniques. Still, these methods involve high synthesis temperature (above 150°C) and highly toxic solvents or ligands such as TOPO, TBP, etc., phosphine-based compounds.

Compared to these methods, the adopted aqueous route synthesis has several advantages: water-soluble products, lower synthesis temperature (below 100°C), high reproducibility, and low toxic chemicals [23]. The decoupling doping method with two distinct approaches, growth-doping and nucleation-doping, was used for co-doping of transition metals (Cu and Mn) into host ZnSe QDs. The nucleation doping strategy is the most successful doping approach for Mn dopant, while growth doping is favorable for Cu dopant in the host ZnSe QDs [24-33]. Therefore, to achieve successful co-doping

Mn and Cu ions are introduced at two different reaction times, such that the transition metals hold their distinctive emission properties.

As an alternative component of white light generating phosphors, the QDs should have large stokes shift to reduce the re-absorption between the various QDs and minimize the light scattering effect. Many attractive alternatives are proposed in recent years having a single component white light-emitting fluorophore which consists of lanthanides (Ln) complex with green and blue-emitting organic ligands [34] and other similar systems having specific emission wavelength with 4f-4f transitions of trivalent Ln ions, e.g., Sm, Gd, Eu, Tb, Pr and Dy [35-37]. Inorganic luminescent materials were also reported as a good alternative with better thermal stability, such as QDs but developing white light-emitting, good quality and high quantum yield QDs via direct aqueous route challenging task. The main difficulty in obtained white emission was controlling the defect levels emission, but other techniques like high-temperature synthesis provide only limited control over the defects related emissions. Considering this difficulty, we studied the QDs emissions at different periods. The results show that the emission levels of different defect states may be controlled by varying the reaction time. Therefore, this route provides synthesis versatility and helps achieve the white light from a single component.

Herein a facile and controlled aqueous route synthesis of less toxic, highly stable and luminescent ZnSe, Cu@ZnSe, Mn@ZnSe QDs together with the exciton dynamics using time-correlated single-photon counting system and femtosecond pump-probe techniques were presented. The co-doping of Cu and Mn transition metal ions in the host ZnSe generates the emission bands that remarkably correspond to the two primary colors, i.e., green and red, which mostly occupy the wide visible spectral range. The doping combination of Cu and Mn in the host ZnSe QDs produces the white light as

shown with the CIE color coordinates plot. Therefore, the synthesized Cu&Mn@ZnSe QDs will be used as a promising single component white light emitter material to produce white-QLEDs.

7.2. Materials and Method

7.2.1. Chemicals

All chemicals used in this work were of scientific grade and were used without further purification. Zinc acetate dehydrate ($Zn(CH_3COO)_2.H_2O$, 98%) and 3-mercaptopropionic acid (MPA) ($C_3H_6O_2S$, 99%) were purchased from ACROS Organics. Sodium borohydride ($NaBH_4$, 95%) and manganese (II) chloride tetrahydrate ($MnCl_2.4H_2O$, 99%) were purchased from Central Drug House. Selenium powder (Se, 99.5%) and copper (II) nitrate trihydrate ($Cu(NO_3)_2.3H_2O$, 99.5%) were purchased from Sigma Aldrich, Potassium hydroxide (KOH, 85%) was purchased from RANKEM. HPLC grade ethanol (CH_3CH_2OH, 99.9%) and ultra-pure water were used as solvents.

7.2.2. Synthesis of ZnSe QDs

All reactions were operated in a three-neck flask. The left neck was associated with a temperature controller, i.e., a thermometer, the middle neck connected to nitrogen gas flow and the right neck attached to a syringe through which the solution was injected or ejected. ZnSe QDs synthesis was implemented in an aqueous medium at around 75 °C. The precursor solution was prepared in three-neck flasks. A mixture of 0.083 g of $Zn(CH_3COO)_2$ and 1 ml of MPA (acts as a capping agent in the process) was mixed in 20 ml of ultra-pure water, and the pH of the solution was maintained at about 10.3 by adding 2 mM KOH dropwise. This solution was stirred under a nitrogen atmosphere for about 15 minutes at around 75 °C. NaHSe as Se stock solution was prepared by mixing 0.052 g of selenium powder and 0.068 g of $NaBH_4$ in 4 ml ultra-pure water. At

the time of mixing, the colour of the solution (Se and $NaBH_4$) was black, but after 10-15 min, it becomes transparent. Then, the mixture solution was transferred to a syringe. The arranged NaHSe solution was added dropwise into the Zn precursor solution at the prefixed temperature of 75 °C. After adding Se stock solution into Zn precursor, the color of the solution transforms from transparent to first light yellow and then pale yellow as time passes. A certain amount of solution was taken out from the solution mixture with the help of a syringe at 10 minute intervals (i.e., 10, 20 min, *etc.*). The synthesized ZnSe QDs were precipitated by adding ethanol to the mixture and then centrifuged for 10 minutes. After that, the precipitated QDs were collected and washed with ethanol. This process was repeated 2 to 3 times. After excluding ligands from ZnSe solution, the purified solution was dried in a hot air oven. Finally, the prepared powder was permitted to cool off slowly to room temperature and the synthesized ZnSe QDs were utilized precisely without further treatment.

7.2.3. Synthesis of Cu-doped and Mn-doped ZnSe QDs

Copper-doped and manganese-doped ZnSe QDs were synthesized in an aqueous medium at around 65 °C. The preparation method of Zn precursor and Se stock solution was the same as in the case of ZnSe QDs' synthesis. After that, in case of Cu doping 0.3 ml of Cu stock solution (prepared by dissolving 0.0071 g of $Cu(NO_3)_2$ in 5 ml ultra-pure water) and in case of Mn doping, 0.6 ml of Mn stock solution (prepared by dissolving 0.0062 g of $MnCl_2$ in 5 ml ultra-pure water) was added dropwise to the Zn precursor along with Se stock solution with a separate syringe at the prefixed temperature of 65 °C and the reaction was allowed to continue for 45 and 75 minutes to get the Cu doped and Mn-doped ZnSe respectively. While adding Cu solution to the reaction mixture (Se and Zn precursor), the colour of the solution transformed from light yellow to blackish yellow and finally to dark yellow. For Mn solution, the colour

of the solution transformed from light yellow to milky yellow and finally to yellow. A certain amount of solution was taken out from the solution mixture with the help of a syringe at 15-minute intervals (i.e., 15 min, 30 min. etc.). The synthesized Cu and Mn-doped ZnSe QDs were precipitated by adding ethanol into the mixture and then centrifuged for 10 minutes. After that, the precipitated QDs were collected and washed with ethanol. This process was repeated 2 to 3 times. After excluding ligands from Cu@ZnSe and Mn@ZnSe solution, the purified solution was dried in a hot air oven. Finally, the prepared powder was permitted to cool off slowly to room temperature and the synthesized Cu@ZnSe and Mn@ZnSe QDs were utilized specifically without further treatment.

7.2.4 Synthesis of Mn and Cu co-doped ZnSe QDs

Manganese and copper co-doped ZnSe QDs were synthesized in an aqueous medium at around 65 °C. The Zn precursor and Se stock solution's preparation method was the same as ZnSe QDs synthesis. After that, 0.6 ml of Mn stock solution was added dropwise to the Zn precursor and Se stock solution with a separate syringe at the prefixed temperature of 65 °C and the reaction was allowed to continue for 35 minutes. After that, 0.8ml of Cu stock solution was also injected dropwise through a syringe into the reaction mixture. While adding a Cu solution to the reaction mixture (Mn@ZnSe), the colour of the solution transformed from milky yellow to dark yellow. A certain amount of solution was taken out from the solution mixture with the help of a syringe at 10-min intervals (i.e., 10 min, 20 min., 30 min., etc.). The reaction setup was kept in the same conditions for another 40 minutes to get the Mn and Cu co-doped ZnSe. The synthesized Mn and Cu co-doped ZnSe QDs were precipitated by adding ethanol into the mixture and then centrifuged for 10 minutes. After that, the precipitated QDs were collected and washed with ethanol. This process was repeated 2 to 3 times. After

excluding ligands from Cu&Mn@ZnSe solution, the purified solution was dried in a hot air oven. Finally, the prepared powder was permitted to cool off slowly to room temperature and the synthesized Cu&Mn@ZnSe QDs were explicitly utilized without further treatment.

7.2.5. Spectroscopic Techniques

The detail of the steady-state and time-resolved spectroscopic techniques are already discussed in previous chapters. A Delta diode of 375 nm was used to measure decay times in ns regions, which has a typical FWHM 200 ps and pulse repetition rate of about 2 MHz as an excitation source. Similarly, the detail of XRD and TEM system are also discussed in previous chapters.

The broadband femtosecond pump measured transient absorption (TA) spectra to probe technique. Details of the setup are presented elsewhere [8,38]. The pump pulse of 30 fs centered at 360 nm was used to excite the QDs. The diameter of the pump spot was 300 μm. The diameter of the probe pulse was 120 μm. The pump-pulse operation frequency was 60 Hz. The sample in 300 μm cell was refreshed between incident laser pulses by a pump. The transient absorption data were obtained with pump-probe polarization at a magic angle of 54.7^{o}. The experiments were carried out at 293 K. The measured spectra were corrected to account for the group delay dispersion of the supercontinuum by the procedure described in below:

The regenerative amplifier system (Spitfire, Spectra-Physics, USA) intensifies the Ti: sapphire oscillator (800 nm, 80 MHz, 80 fs, Tsunami, Spectra-Physics, Santa Clara, CA, USA). The femtosecond gauss pump pulse of 200 nJ, 30 fs centered at 360 nm was used to excite the ZnSe QDs and Cu&Mn@ZnSe QDs dispersed in water. The pump pulse operation frequency was 60 Hz. The

sample in a 300 μm cell was refreshed between incident laser pulses by a pump. The probe pulse was light of supercontinuum generated in H_2O cell by focused 800 nm femtosecond pulses. Transient spectra of absorbance change ΔA (t, λ) were recorded over the range of 380–800 nm. The pump and probe light spots had diameters of 300 and 120 μm, respectively. The relative polarization of pump and probe pulses was oriented at 54.7°, parallel or perpendicular. The experiments were carried out at 278 K. The measured spectra were corrected for group delay dispersion of the supercontinuum using the procedure described in (Shelaev et al. 2008; Nadtochenko et al. 2017) [50-51]. The time window of the "coherence spike" seen during the pump-probe overlap was neglected.

7.3. Results and Discussion

7.3.1. Size and surface ligands of water-dispersed ZnSe, Cu@ZnSe, Mn@ZnSe, and Cu&Mn@ZnSe QDs.

The structural and morphological studies were carried out using XRD and TEM spectroscopies. The XRD patterns of the prepared transition metal-doped ZnSe QDs resemble the cubic zinc blende crystal structure (shown in the previous chapter). The XRD pattern is widened and shows the nanocrystalline nature of the samples with three central peaks at 27.5°, 45.8° and 53.9°, corresponding to the (111), (220) and (311) planes. The doping of Mn and Cu into ZnSe does not change its crystal structure. This further confirms the formation of Cu&Mn@ZnSe solid solution instead of Mn and Cu precipitation [39]. The size and morphology of MPA-capped ZnSe and Cu&Mn@ZnSe QDs were additionally affirmed by utilizing TEM. Even though slight aggregation of QDs appeared in the TEM images, most QDs appeared as quasi-spherical particles. For the ZnSe, Cu@ZnSe, Mn@ZnSe and Cu&Mn@ZnSe QDs, the particle diameter was between 3.2 and 5.4 nm. For the ZnSe QDs, the bulk Bohr exciton radius reported by

Chin *et al.* [41] is 3.8 nm. Hence, the produced NCs show a significant quantum confinement impact.

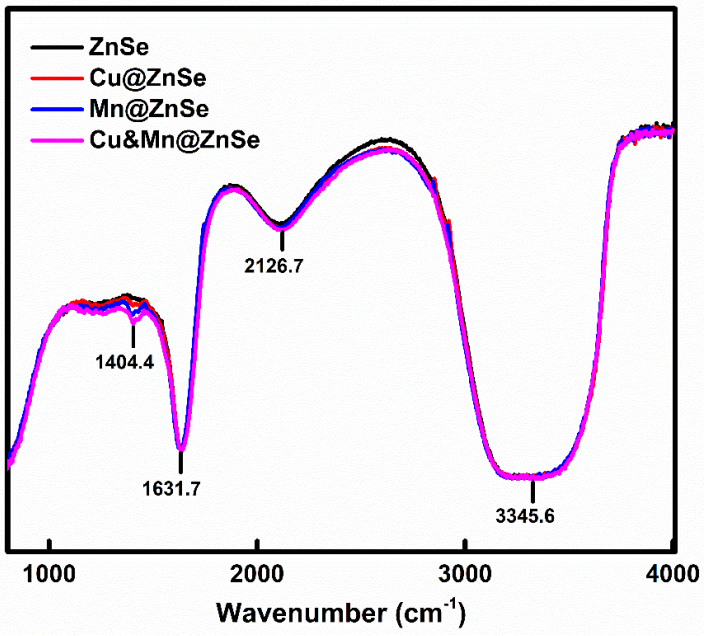

Figure 7.1. FTIR spectra of MPA-capped ZnSe and metal incorporated ZnSe QDs

Recently, strategies are devised to cap the surface of NPs with a capping reagent to activate the surface of NPs and make NPs resistant to aggregation. While producing the ZnSe and transition metal doped ZnSe QDs, mercaptopropionic acid (MPA) was used as the capping reagent and stabilizer to regulate the development of the NPs throughout the synthesis process. The FT-IR spectra of MPA-capped ZnSe, Cu@ZnSe, Mn@ZnSe and Cu&Mn@ZnSe NPs are shown in Fig. 7.1. FT-IR spectra exhibit various characteristic spectral bands. The band around 3345 cm^{-1} corresponds to the O–H stretching vibration, the peak at 2126 cm^{-1} because of C ≡ C stretching and the band about 1632 cm^{-1} arising from the C=O stretching [42]. Moreover, the amplitude of S–H stretching vibration determined within the 2600–2550 cm^{-1} region is negligibly small, suggesting the sulfhydryl (−SH) from MPA is adsorbed onto the surface of the particles in the form of a closed packed monolayer that stabilizes QDs in solution. Thus, MPA molecules capped the prepared NPs.

7.3.2. Absorption and photoluminescence characteristics of water-dispersed ZnSe, Cu@ZnSe, Mn@ZnSe, and Cu&Mn@ZnSe QDs.

Fig. 7.2 shows absorption and PL-excitation spectra of ZnSe, Mn-doped ZnSe and Cu co-doped Mn@ZnSe QDs dispersed in water. The absorption shows a band maximum between 390-410 nm, which might be assigned to the $1S^{e}$ - $1S^{h}_{3/2}$ and $1P^{e}$-$1P^{h}$ transitions, as shown in the second derivative of the absorption, representing two bands maxima and overlapped PL-excitation spectra as shown in Fig. 7.2.

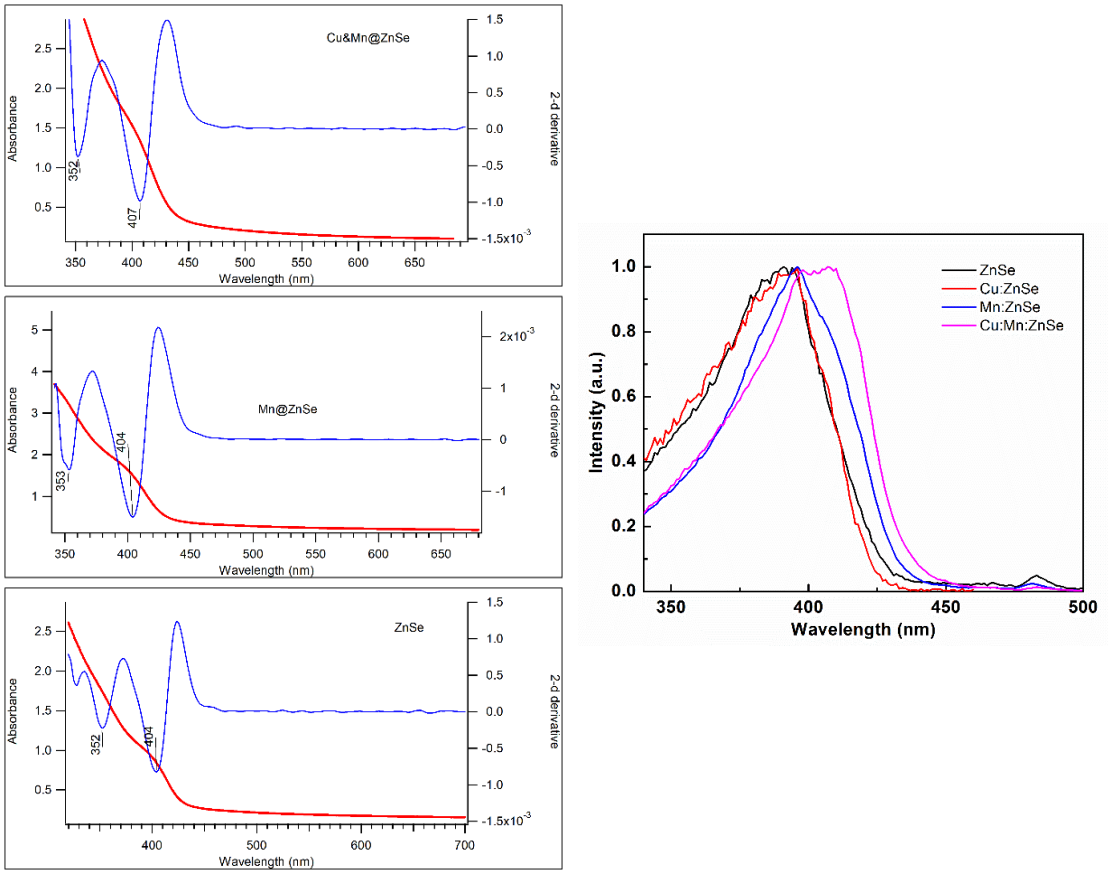

Figure 7.2. Absorption spectra and the second derivative of the absorption spectra of ZnSe and transition metal doped ZnSe dispersed in water (left) and overlapped excitation spectra (right) of ZnSe and transition metal doped ZnSe dispersed in water at the 430 and 580 emission wavelengths.

Fig. 7.3 demonstrates the PL spectra of ZnSe, Mn@ZnSe and Cu,Mn@ZnSe QDs formed at different synthesis times. To reveal the spectral components in the wide

PL bands, spectra are shown in the form of derivatives. Spectra in the form of derivatives manifest that PL band is inhomogeneous. The peaks close to 420-430 nm can be tentatively attributed to the band-edge exciton PL. This suggestion is confirmed by observing the bleach band in a similar spectral range in the femtosecond pump-probe experiments (see Fig. 7.9 and 7.10). Several peaks between 440-540 nm can be attributed to the trap states luminescence.

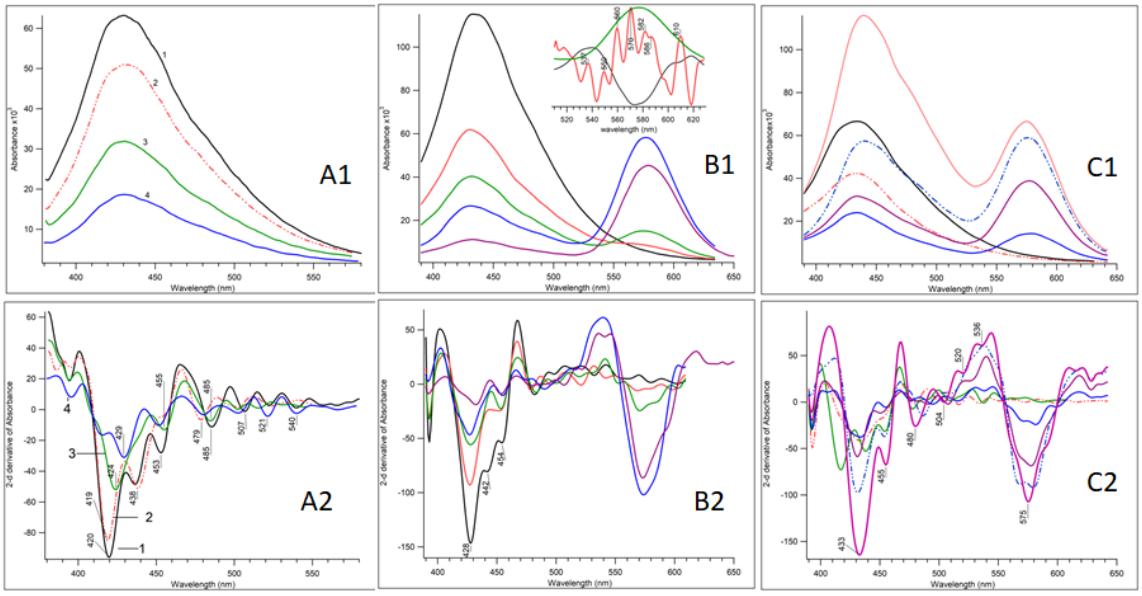

Figure 7.3. Photoluminescence spectra, along with the derivative spectra of ZnSe (A1 and A2) and Mn@ZnSe (B1 and B2) and Cu&Mn@ZnSe (C1 and C2). Insert of B1 demonstrates the Mn^{2+} luminescence band in a 2^{nd} (black line) and 4^{th} derivatives (red line).

The general motif of the luminescence band shape is similar for samples at different time formations. At the same time Fig. 7.3 (A2) shows that the exact position of the spectral components is varied, which means the changes of traps composition. Figs. 7.3 (B1, B2 and C1, C2) reveal meaningful PL band changes during the synthesis of metal-doped QDs. The band-edge exciton luminescence decreases, whereas the long-wavelength band corresponding to Mn2+ increases as synthesis time grows. The luminescence spectra ($^4T_1 \rightarrow {}^6A_1$ transition of Mn^{2+}) in the form of second and forth

derivatives demonstrate the variety of sites of Mn^{2+} localization and changes of Mn^{2+} PL peaks distribution with reaction time. The PL band appeared as a wideband centered close to 431 nm (Fig. 7.3 (A1). This band suggests the emission from trap states. It contrasts to the expected narrow peak with a small Stokes shift due to the band edge emission of ZnSe QDs synthesized by high-temperature technique. The photoluminescence excitation (PLE) corresponding to 431 nm PL band is close to the band edge exciton state, as shown in Fig. 7.2. This suggests that PL trap is excited due to the non-radiative transition from band edge exciton.

The PL spectrum of Mn-doped ZnSe QDs shows two prominent peaks at 431 nm and 577 nm, as shown in Fig. 7.3 (B1). The strong yellow-orange color at 577 nm comes from the $^4T_1$–$^6A_1$ transition of the Mn^{2+} impurity due to excited energy transfer from the host ZnSe [18-22]. From manganese-doped semiconductors (like Mn-doped ZnS, Mn-doped CdSe), the most frequently acquired emission wavelengths vary from 570 to 590 nm (yellow-orange color). The peak at 431 nm is assigned to the direct band gap emission of ZnSe QDs, which was observed because of the low Mn^{2+} dopant concentration present in the solution mixture [45]. As the reaction time interval increases, the PL intensity observed at 431 nm decreases gradually, whereas the PL intensity at 577 nm increases (Fig. 7.3 (B1)), which might be due to increased Mn^{2+} concentration or may be an increase of the energy transfer rate. Changing the proportion of transition metal in the solution shows that the emission wavelength or intensity changes slightly [46]. Upon increasing the proportion of Mn^{2+} concentration in Mn-doped ZnSe NCs, an intense Mn-related PL peak is observed. Alternatively, this may also produce slightly blue-shifted PL due to creating Zn or Se ion vacancies in the nanocrystal [24].

In PL of the co-doped ZnSe framework, in addition to the 431 nm, two more bands are observed and cover a broad range of visible light (Fig. 7.3 (C1). However, during reactions, it was determined that Cu ions were adsorbed by the previously developed Mn-doped ZnSe QDs and accordingly populated these surface states, making them favorable for white light generation QLEDs (Fig. 7.4).

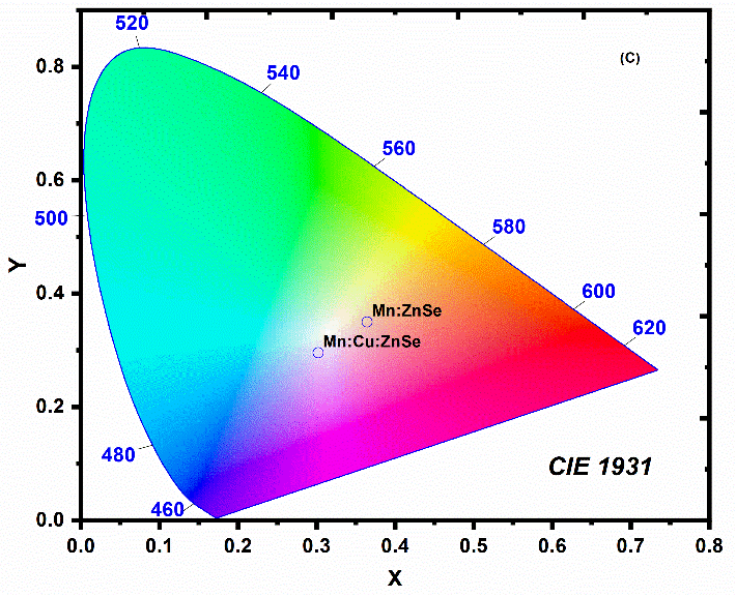

Figure 7.4. CIE-1931 chromaticity diagram of Mn@ZnSe and Cu&Mn@ZnSe QDs.

The PL intensity of the 431 nm band decreases while the intensity of 577 nm band increases. After injecting the Cu^{2+} ions into the solution, the PL intensity of the 431 nm band starts gradually growing and shows a slight redshift with time. Together with this band, the intensity of the 577 nm band increases. The intensity of both the bands increases as the reflux time increases (Fig. 7.3 (C1)). The strong PL comes from the transition of Cu^{2+} impurity due to excited energy transfer from the host ZnSe to the Cu^{2+} ions. This peak may be allotted to the recombination of an energized electron in the conduction band/defect states of the ZnSe nanocrystal with the d-orbital hole of a Cu ion [24,47,48]. The PL quantum yield (QY) calculate using absorption and blue PL bands are about 1% for pure ZnSe and 3 % for metal-doped ZnSe QDs.

7.3.3. Photoluminescence decay characteristics of water-dispersed ZnSe, Cu@ZnSe, Mn@ZnSe and Cu&Mn@ZnSe QDs.

The PL lifetimes of ZnSe, Cu@ZnSe, Mn@ZnSe and co-doped Cu&Mn@ZnSe were measured to understand the excited state dynamics, and the obtained results are summarized in Tables 7.1 and 7.2.

Table 7.1. The photoluminescence lifetimes of ZnSe, Cu@ZnSe, Mn@ZnSe and Cu&Mn@ZnSe QDs dispersed in water. The excitation and emission wavelengths were 375 and 430 nm, respectively.

QDs	τ_1 (ns)	α_1	τ_2 (ns)	α_2	τ_3 (ns)	α_3	τ_{av} (ns)	χ^2
ZnSe	0.84 ± 0.02	0.10	6.96 ± 0.07	0.04	0.10 ± 0.002	0.87	4.31	1.11
Cu@ZnSe	0.57 ± 0.01	0.03	7.67 ± 0.05	0.01	0.03 ± 0.004	0.96	5.03	1.10
Mn@ZnSe	0.73 ± 0.03	0.03	7.24 ± 0.20	0.01	0.08 ± 0.001	0.96	3.13	1.06
Cu&Mn@ZnSe	0.55 ± 0.02	0.45	7.94 ± 0.03	0.19	0.20 ± 0.020	0.35	6.65	1.11

The decay profiles of ZnSe dispersed in water could not fit well with a single and bi-exponential function. However, it fits well with tri-exponential functions defined by $I(t) = \alpha_1 \exp\left(-t/\tau_1\right) + \alpha_2 \exp\left(-t/\tau_2\right) + \alpha_3 \exp\left(-t/\tau_3\right)$,

where τ_1, τ_2 and τ_3 represent the lifetimes and α_1, α_2 and α_3 are the corresponding pre-exponential factors, respectively. The fitting of the decay curves was judged with χ^2 value and residual. The fitted decay curves are shown in Fig. 7.5.

Table 7.2. The photoluminescence lifetimes of Mn@ZnSe and Cu&Mn@ZnSe QDs dispersed in water. The excitation and emission wavelengths were 330 nm and 580 nm, respectively.

Sample (QDs)	τ_1 (μs)	A_1	τ_2 (μs)	A_2	τ_{av} (μs)
Mn@ZnSe	601	49.22	101	50.78	347.23
Cu&Mn@ZnSe	866	43.62	290	56.38	541.17

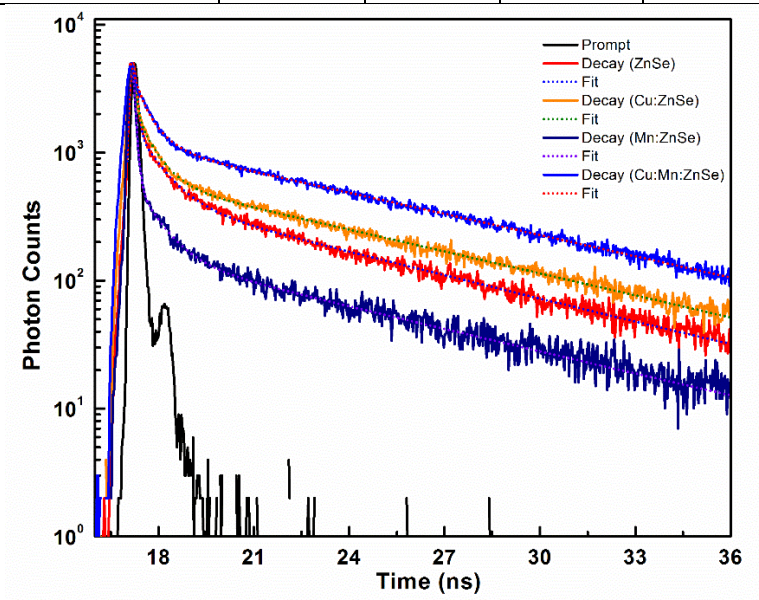

Figure 7.5. Fitted photoluminescence (PL) decay curves of ZnSe, Cu@ZnSe, Mn@ZnSe and Cu&Mn@ZnSe co-doped QDs. Excitation and emission wavelengths were 375 nm and 430 nm, respectively.

The observed multiple lifetime components are originated from different emission centers of metal-doped ZnSe QDs. Out of the three lifetimes, the shortest component, which has a lifetime of ~0.1 ns, has the highest amplitude value to the PL and is assigned to the direct band gap emission. The remaining two lifetimes of 0.84 ns and 6.96 ns, might be assigned to the defect states, which emit nearly in the same wavelength regions. The average lifetime defined as $\tau_{av} = \Sigma_i \alpha_i \tau_i^2 / \Sigma_i \alpha_i \tau_i$, is also calculated and comes out to be 4.3 ns (Table 7.1). In Cu doped ZnSe (Cu@ZnSe), the decay curves fitted well with tri-exponential functions with slightly different lifetimes

and pre-exponential factors. The shortest lifetime component with a lifetime of 0.03 ns has the maximum contribution to the overall decay profile. The contribution of the longest lifetime components in overall decay is small. In Mn-doped ZnSe (Mn@ZnSe), a new and large Stokes shifted PL band arises at around 577 nm. The decays collected at 580 nm are well fitted with bi-exponential functions with an adjustment R^2=0.99 (Fig. 7.6).

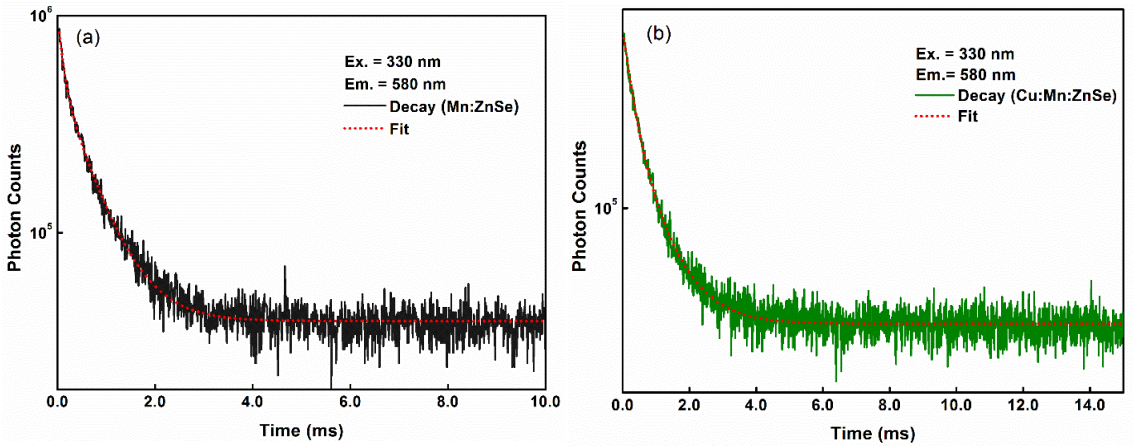

Figure 7.6. Fitted photoluminescence (PL) decay curves of Mn@ZnSe (a) and Cu&Mn@ZnSe (b) QDs. Excitation and emission wavelengths were 330 nm and 580 nm, respectively.

The fitted lifetimes are 101 μs and 601 μs. A_1 and A_2 denote the corresponding amplitudes. Both the lifetime components have nearly the same contribution (Table 7.2). The long-lived component of 601 μs might represent the $^4T_1$–$^6A_1$ state of Mn ions [22]. However, the 101 μs component, which has a nearly equal contribution, might be the second transition of metal ions, occurring approximately within the same wavelength region as demonstrated in Fig. 7.6 or the distribution of lifetimes. Furthermore, the lifetime of Cu co-doped Mn-ZnSe was measured in similar experimental conditions as for Mn-ZnSe. The observed decay curves are again fitted well with bi-exponential functions. It is important to note that both the lifetime

components increase largely in co-doped QDs and are supported to the steady-state PL. The smaller component increases nearly three folds, whereas the longer one becomes 866 μs. The increase in the lifetimes is assigned to the decrease of non-radiative rates or increase of the radiative rates. Panda *et al.* [10] observed a single exponential decay for 585 nm with a lifetime of 264 μs and 324 μs for Mn@ZnSe and Cu&Mn@ZnSe QDs, respectively prepared at high temperatures (>100˚C). The observed excited-state lifetime of 866 μs is a new record of the longest for the Cu doped Mn@ZnSe QDs, almost threefold longer than the longest reported previously [10]. In the present study, the decay is non-exponential and fitted well with the bi-exponential functions with two long lifetime components, which have nearly the same contribution and might be assigned to the two different transitions populated from two different routes of energy transfer (i) from ZnSe lattices to the Mn ions and (ii) from shallow trap state of ZnSe to the Mn ions. In co-doped ZnSe, both components become longer, indicating that the non-radiative transitions decrease. Thus, co-doping further supports enhancing the PL of the 577 nm band (Fig. 7.3). This is due to the increase of excitation energy transfer from ZnSe to metal ions due to an increase of overlapped areas between absorption of metal ions and emission of ZnSe.

The steady-state and time-resolved experiments have demonstrated that there are three emitting states in co-doped ZnSe QDs, which cover the visible range. The excited electrons may relax from LUMO-HOMO in ZnSe, via d level of Cu ion in Cu doped and via *d-d* level in Mn-doped ZnSe QDs [28]. The shortest lifetime component represents the band edge PL. The intermediate one corresponds to the emitting state produced through the energy transfer of ZnSe to Cu ions. The longest component represents the emitting state produced by large distance energy transfer ZnSe lattice to the Mn ions. The present results, both the short and long-lived lifetime components, are

quite convincing [28]. However, the unusual long decay component, which becomes more efficient in the presence of the co-doped ZnSe, is assigned to the PL of $^4T_1$–$^6A_1$ state activated following the energy transferred from ZnSe lattices to the Mn ions.

As mentioned, both the decay components increase in co-doped ZnSe, which demonstrates that the radiative rates of these component increases. Thus, the long-lived state covering the long-wavelength range is essential for single component white-light engines for solid-state lighting. Also, water-dispersible and relatively less toxic QDs are important for biological applications.

7.3.4. Transient absorption spectra and transient kinetics of ZnSe and metal-doped ZnSe QDs.

To explore an ultrafast dynamic of pure ZnSe and metal-doped ZnSe QDs, transient absorption (TA) spectra and TA kinetics were measured with a pump pulse of 30 fs centered at 360 nm to excite the QDs. The pump energy was varied from 0.25 to 3.5 μJ to clarify the effect of the bi- and multiexciton states on transient spectra. The TA spectra and kinetics were obtained at different delay times, probe wavelengths and energy. 3D images of transient absorption spectra of ZnSe, Mn-doped ZnSe and Cu co-doped Mn@ZnSe colloid QDs dispersed in water with the pump wavelength 360 nm illustrates in Figs. 7.9-7.11.

Transient absorption spectra of pure ZnSe, Mn@ZnSe and Cu&Mn@ZnSe obtained at short time delays show two specific spectral features: (i) a strong bleaching band close to 405 nm and (ii) a broad absorption band in the spectral range of ~440 nm to 670 nm (Fig. 7.7). The pump energy effect on the transient absorption spectra in the range of 0.25 μJ and 3.4 μJ (0.35 mJ/cm^2 and 4.8 mJ/cm^2) is small and nonlinear effects of QDs excitation on the transient is not considered in the present work.

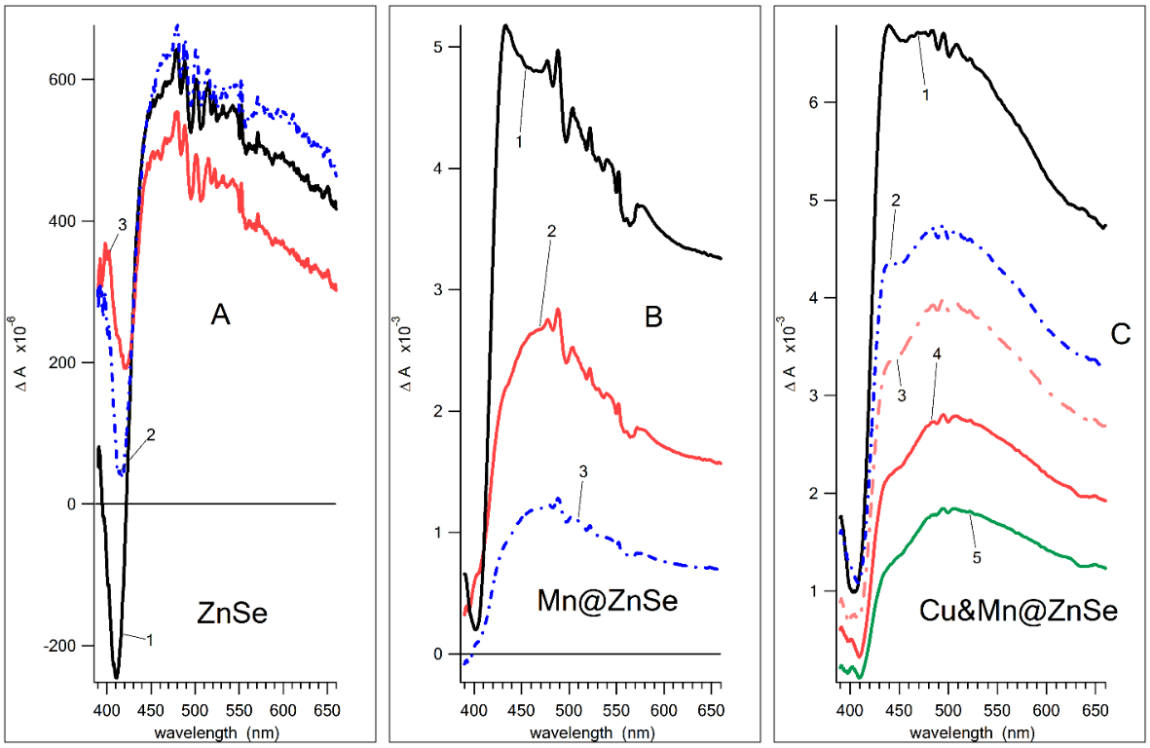

Figure 7.7. Transient spectra of pure ZnSe, Mn@ZnSe, Cu&Mn@ZnSe QDs colloid at long time delays. A, time delays are: 1, 2.5 ps; 2, 50 ps; 3, 350 ps. B, time delays are: 1, 6 ps; 2, 100 ps; 3, 450 ps. C, time delays are: 1, 2 ps; 2, 15 ps; 3, 30 ps; 4, 105 ps; 5, 435 ps. The pump energy was 3.4 μJ.

Fig. 7.7 shows transient absorption spectra at a long time delay and reveals a decay in the long-time delay window. The observed bleaching band near 405 nm associates with

the lowest exciton (see absorption spectra Fig. 7.2). The appearance of the bleaching band may explain the exciton state filling and the Stark band shift effect [49]. On the other hand, the excited state absorption (ESA) of TA spectra can be attributed to the trap states absorption and probably the biexciton absorption band close to 480 nm at the short time delays. The bleaching band at 405 nm appears at the time delay shorter than 100 fs, whereas the pump wavelength was 360 nm that corresponds to the excitation of the higher excitonic state (Fig. 7.2). Fig. 7.7 shows that no meaningful increase of the bleaching band amplitude is detected at the time delay close to 100 fs.

It suggests that the relaxation from the higher excitonic state to the lowest excitonic state occurs in the time window shorter ~100 femtoseconds. Fig. 7.7 depicts that the bleaching band amplitude decays in the time range shorter than ~1-2 ps. It assumes that the electronic population of the exciton state is depleted due to the transition to trap states. The fast non-radiative energy transfer from the exciton state to trap states is a reason of the low intensity of the band edge exciton PL. Fig. 7.8 also exhibits the rise of the ESA band amplitude that is in accord with the observation of the bleaching band decay. The ESA bands alter the shape during time delay, suggesting population changes of different traps (Fig. 7.8 and 7.10).

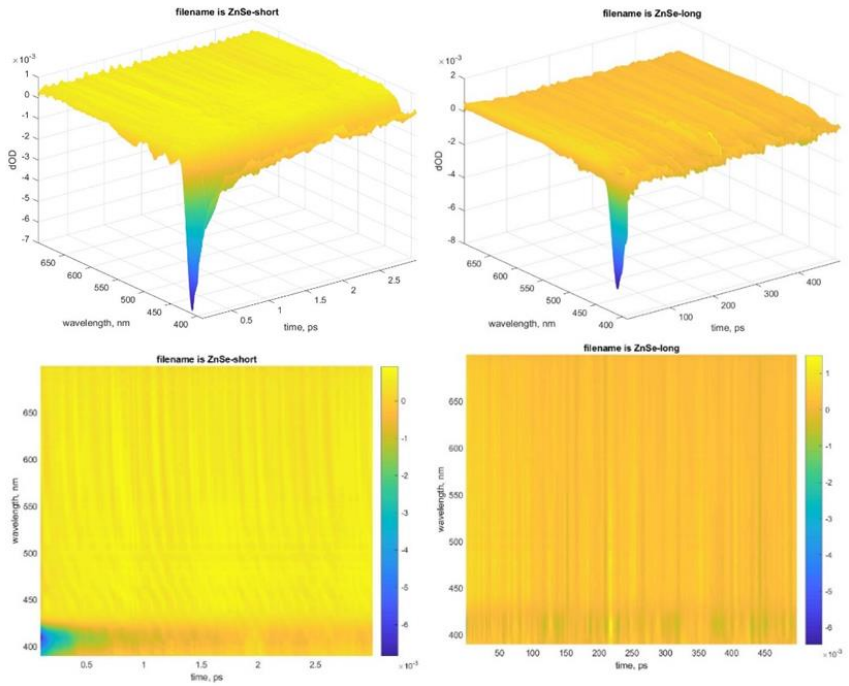

Figure 7.8. 3D images of transient absorption spectra of ZnSe colloid QDs dispersed in water. Pump wavelength was 360 nm @ 2.4 μJ.

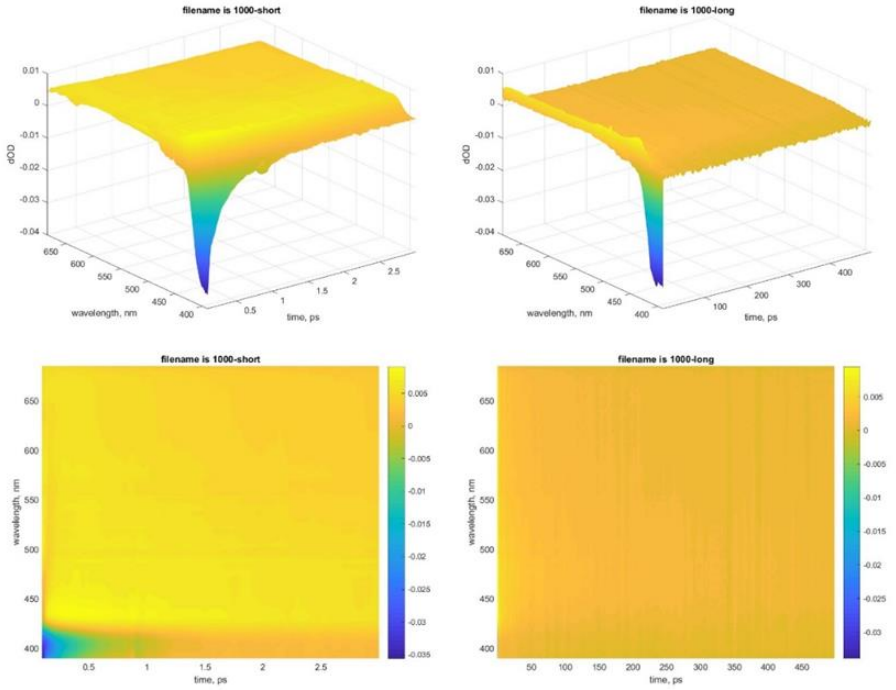

Figure 7.9. 3D images of transient absorption spectra of Mn@ZnSe colloid QDs dispersed in water. The pump wavelength was 360 nm.

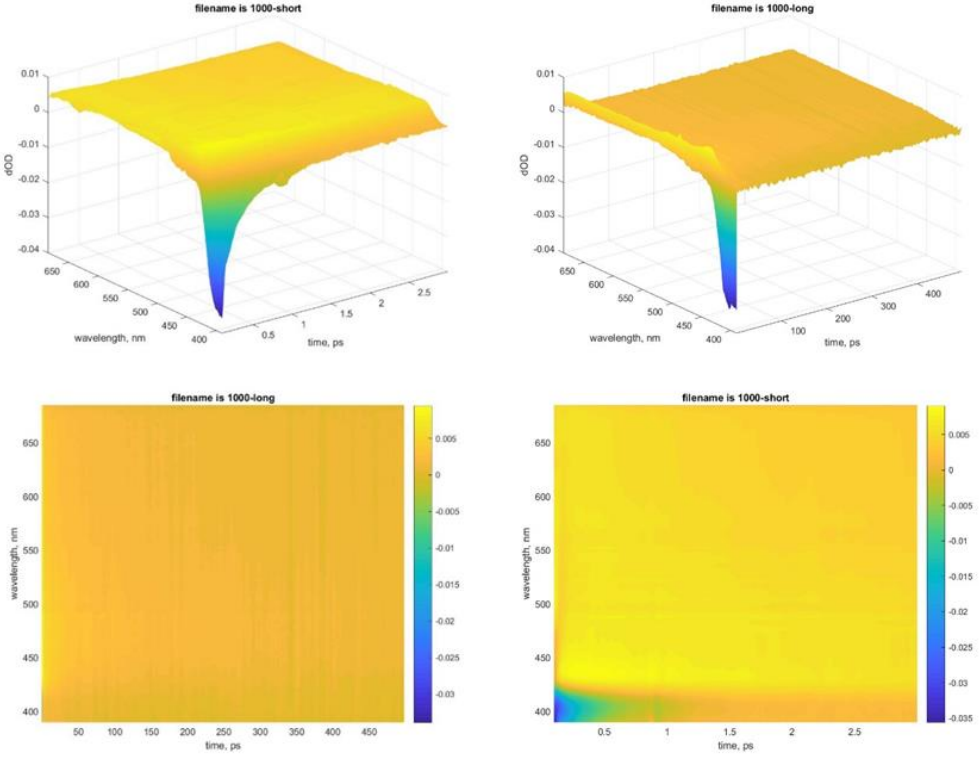

Figure 7.10. 3D images of transient absorption spectra of Cu co-doped Mn@ZnSe colloid QDs dispersed in water. The pump wavelength was 360 nm.

The transient curves of pure ZnSe, Mn@ZnSe and Cu&Mn@ZnSe QDs are shown at selected probe wavelengths (Figs 7.8-7.10). The transient kinetics at a probe wavelength of 405 nm are related to the bleaching band, and at a probe wavelength of 450 nm corresponding to the absorption band (ESA band). The transient kinetics of the bleaching band decay are fitted well with the bi-exponential function. The decay time and the relative amplitude of the decay components are summarized in Table 7.3.

Table 7.3. Fitted parameters of transient kinetics at 405 nm.

Sample (QDs)	**τ_1 (ps)**	**A_1**	**τ_2 (ps)**	**A_2**
ZnSe	2.01 ± 0.13	12.2%	0.19 ± 0.006	88%
Mn@ZnSe	0.500 ± 0.01	45.3%	0.130 ± 0.006	54.7%
Cu&Mn@ZnSe	0.59 ± 0.023	30.0%	0.130 ± 0.02	70%

The relative amplitude of fast decay components is higher than 55% for all samples. For pure ZnSe samples, the decay time is equal to 190 fs, whereas for Cu and Mn-doped samples, it is shorter and equals 130 fs. The decay time of the slower component is 2 ps for pure ZnSe, whereas, for doped samples, the decay time is close to 500 fs, 600 fs. Presumably, the increase of the bleach decay rate in the metal-doped samples is not only to the energy transfer from the excitonic state to metal centers but due to the changes in traps distribution in QDs and, as a result, the enhancement of the acceptance of the exciton energy by traps. The assumption about the changes in traps distribution in QDs due to the Mn and Cu doping agrees with the observation of the increase of the ESA amplitude relative to the bleaching band amplitude shown in Fig. 7.10. The slow time constant of ESA band decay is present in Table 7.4. Biexponential fitting of transient kinetics of 450 nm for Mn@ZnSe and Cu&Mn@ZnSe samples reveals the decay with a time constant close to 2-3 ps with the relative amplitude close to ~50%

and with the time constant of 81 ps for Mn@ZnSe and the time constant of 49 ps for Cu&Mn@ZnSe.

Table 7.4. Decay times of transient kinetics at 450 nm.

Sample (QDs)	τ_1 (ps)	A_1	τ_2	A_2
ZnSe	100 ± 12	------	---	---
Mn@ZnSe	81 ± 2.1	50%	3.5 ± 0.064	50%
Cu& Mn@ZnSe	49 ± 1.2	43%	2.14 ± 0.04 ps	57%

The ESA decay for pure ZnSe is monoexponential with a time constant of 100 ps. The slow ESA decay may be attributed to the trapping of the charge carrier by deeper traps and by the recombination of charge carriers in QDs. The acceleration of the ESA transient decay suggests that metal centers can modify trap states. As a result, they can accept excitation energy from excited traps or promote the recombination of charges.

7.4. Conclusions

Metal-doped and co-doped water-dispersed ZnSe, Cu@ZnSe, Mn@ZnSe, and Cu&Mn@ZnSe QDs were successfully synthesized via an aqueous route using MPA as a capping agent at a lower temperature than the boiling point of water. The lower temperature aqueous-based synthesis was found simple, economical, efficient and environmentally friendly compared to other synthesis techniques. The reaction time and temperature are crucial factors for successfully synthesizing ZnSe and transition metal doped ZnSe QDs. The produced QDs demonstrated a face-centered crystal arrangement and quasi-spherical shapes, and the diameter of QDs lies between 3-5 nm. The band gap of ZnSe NCs and transition metal doped ZnSe NCs was obtained between 3.0 - 3.2 eV and the PL of ZnSe QDs is tuned by doping the metal ions. The metal-doped brilliant emitter with multiple emitting states populated by direct excitation of ZnSe QDs and by the energy transfer from shallow trap state and lattices of ZnSe to metal ions covers

nearly the entire visible region, which may encourage solid-state lighting device implementation that is single source QLEDs. The microseconds to femtoseconds dynamics observed in transient absorption predicted the state filling effect and trapping of electrons in shallow and deep trap states. Doping of ZnSe QDs by Mn and Cu centers suggests a modification of traps revealed in the transient spectra and kinetic parameters of transient decay. A specific feature of the synthesized QDs is the fast energy transfer from the band edge exciton to luminescent trap states and effective energy transfer to luminescent states of Cu & Mn metal ions.

References

[1] M.J. Bowers, J.R. McBride, S.J. Rosenthal, White-light emission from magic-sized cadmium selenide nanocrystals, Journal of the American Chemical Society. 127 (2005) 15378–15379.

[2] S. Sapra, S. Mayilo, T.A. Klar, A.L. Rogach, J. Feldmann, Bright white-light emission from semiconductor nanocrystals: By chance and by design, Advanced Materials. 19 (2007) 569–572.

[3] C.C. Shen, W.L. Tseng, One-step synthesis of white-light-emitting quantum dots at low temperature, Inorganic Chemistry. 48 (2009) 8689–8694.

[4] R.K. Ratnesh, M.S. Mehata, Investigation of biocompatible and protein sensitive highly luminescent quantum dots/nanocrystals of CdSe, CdSe/ZnS and CdSe/CdS, Spectrochimica Acta - Part A: Molecular and Biomolecular Spectroscopy. 179 (2017) 201–210.

[5] M.S. Mehata, Enhancement of charge transfer and quenching of photoluminescence of capped CdS quantum dots, Scientific Reports. 5 (2015) 12056.

[6] S. Jain, M.S. Mehata, Medicinal plant leaf extract and pure flavonoid mediated green synthesis of silver nanoparticles and their enhanced antibacterial property, Scientific Reports. 7 (2017) 15867.

[7] Y. Nandan, M.S. Mehata, Wavefunction engineering of type-I/type-II excitons of CdSe/CdS core-shell quantum dots, Scientific Reports 9 (2019) 2.

[8] D.A. Cherepanov, F.E. Gostev, I.V. Shelaev, N.N. Denisov, V.A. Nadtochenko, Monitoring the electric field in CdSe quantum dots under ultrafast interfacial electron transfer via coherent phonon dynamics, Nanoscale, 10 (2018) 22409-22419.

[9] N. Gaponik, D. V. Talapin, A.L. Rogach, K. Hoppe, E. V. Shevchenko, A. Kornowski, A. Eychmüller, H. Weller, Thiol-capping of CDTe nanocrystals: An alternative to

organometallic synthetic routes, Journal of Physical Chemistry B. 106 (2002) 7177–7185.

[10] S.K. Panda, S.G. Hickey, H.V. Demir, A. Eychmüller, Bright white-light emitting manganese and copper co-doped ZnSe quantum dots, Angewandte Chemie - International Edition. 50 (2011) 4432–4436.

[11] T.D. Thompson, A blue emitting ZnSe LED operating by impact ionization, Semiconductor Science and Technology. 6 (1991) 1015–1019.

[12] P. Reiss, G. Quemard, S. Carayon, J. Bleuse, F. Chandezon, A. Pron, Luminescent ZnSe nanocrystals of high color purity, Materials Chemistry and Physics. 84 (2004) 10–13.

[13] G. Xue, W. Chao, N. Lu, S. Xingguang, Aqueous synthesis of Cu-doped ZnSe quantum dots, Journal of Luminescence. 131 (2011) 1300–1304.

[14] A. Aboulaich, L. Balan, J. Ghanbaja, G. Medjahdi, C. Merlin, R. Schneider, Aqueous route to biocompatible ZnSe:Mn/ZnO core/shell quantum dots using 1-thioglycerol as stabilizer, Chemistry of Materials. 23 (2011) 3706–3713.

[15] P. Kumar, J. Singh, K. Ramam, A.C. Pandey, ZnSe / ZnSe : Ag Nanoparticles : Synthesis, Characterizations, Optical and Raman Studies, Journal of Nanoscience and Nanotechnology. 12 (2012) 1–7.

[16] B.T. Huy, M.H. Seo, A.P. Kumar, H. Jeong, Y.I. Lee, Synthesis and photoluminescence of Cr-, Ni-, Co-, and Ti-doped ZnSe nanoparticles, Journal of Alloys and Compounds. 588 (2014) 127–132.

[17] Z. Fang, P. Wu, X. Zhong, Y.-J. Yang, synthesis of highly luminescent Mn@ZnSe/ZnS nanocrystals in aqueous media, Nanotechnology. 21 (2010) 305604.

[18] P. Shao, H. Wang, Q. Zhang, Y. Li, White light emission from Mn-doped ZnSe d-dots synthesized continuously in microfluidic reactors, Journal of Materials Chemistry. 21 (2011) 17972.

[19] D.J. Norris, N. Yao, F.T. Charnock, T.A. Kennedy, High-Quality Manganese-Doped ZnSe Nanocrystals, Nano Letters. 1 (2001) 3–7.

[20] C. Graf, A. Hofmann, T. Ackermann, C. Boeglin, R. Viswanatha, X. Peng, A.F. Rodríguez, F. Nolting, E. Rühl, Magnetic and Structural Investigation of ZnSe Semiconductor Nanoparticles Doped With Isolated and Core-Concentrated Mn^{2+} Ions, Advanced Functional Materials. 19 (2009) 2501–2510.

[21] J. Xue, Y. Ye, F. Medina, L. Martinez, S. Lopez-Rivera, W. Giriat, Temperature evolution of the 2.1eV band in the Zn1−xMnxSe system for low concentration, Journal of Luminescence. 78 (1998) 173–178.

[22] S.E. Irvine, T. Staudt, E. Rittweger, J. Engelhardt, S.W. Hell, Direct light-driven modulation of luminescence from Mn-doped ZnSe quantum dots, Angewandte Chemie - International Edition. 47 (2008) 2685–2688.

[23] V. Lesnyak, N. Gaponik, A. Eychmüller, Colloidal semiconductor nanocrystals: the aqueous approach, Chem. Soc. Rev. 42 (2013) 2905–2929.

[24] N. Pradhan, D. Goorskey, J. Thessing, X. Peng, An alternative of CdSe nanocrystal emitters: Pure and tunable impurity emissions in ZnSe nanocrystals, Journal of the American Chemical Society. 127 (2005) 17586–17587.

[25] H. Shen, H. Wang, X. Li, J.Z. Niu, H. Wang, X. Chen, L.S. Li, Phosphine-free synthesis of high quality ZnSe, ZnSe/ZnS, and Cu-, Mn-doped ZnSe nanocrystals, Dalton Transactions. (2009) 10534.

[26] N. Pradhan, X. Peng, Efficient and color-tunable Mn-doped ZnSe nanocrystal emitters: Control of optical performance via greener synthetic chemistry, Journal of the American Chemical Society. 129 (2007) 3339–3347.

[27] R. Zeng, M. Rutherford, R. Xie, B. Zou, X. Peng, Synthesis of highly emissive Mn-Doped ZnSe nanocrystals without pyrophoric reagents, Chemistry of Materials. 22

(2010) 2107–2113.

[28] V.K. Sharma, B. Guzelturk, T. Erdem, Y. Kelestemur, H.V. Demir, Tunable white-light-emitting Mn-doped ZnSe nanocrystals, ACS Applied Materials and Interfaces. 6 (2014) 3654–3660.

[29] C. Rajesh, C. Phadnis, K.G. Sonawane, S. Mahamuni, Generation of white light from co-doped (Cu and Mn) ZnSe QDs, Journal of Experimental Nanoscience. 10 (2015) 1082–1092.

[30] S. Jana, B.B. Srivastava, S. Acharya, P.K. Santra, N.R. Jana, D.D. Sarma, N. Pradhan, Prevention of photooxidation in blue–green emitting Cu doped ZnSe nanocrystals, Chemical Communications. 46 (2010) 2853.

[31] Z. Zhuang, Q. Peng, Y. Li, Controlled synthesis of semiconductor nanostructures in the liquid phase, Chemical Society Reviews. 40 (2011) 5492.

[32] N. Murase, M. Gao, Preparation and photoluminescence of water-dispersible ZnSe nanocrystals, Materials Letters. 58 (2004) 3898–3902.

[33] Z. Fang, P. Wu, X. Zhong, Y.-J. Yang, synthesis of highly luminescent Mn@ZnSe/ZnS nanocrystals in aqueous media, Nanotechnology. 21 (2010) 305604.

[34] G. He, D. Guo, C. He, X. Zhang, X. Zhao and C. Duan, A color-tunable europium complex emitting three primary colors and white light, Angew. Chem., Int. Ed. 48 (2009) 6132.

[35] Y. Hasegawa, Y. Wada and S. Yanagida, Strategies for the design of luminescent lanthanide (III) complexes and their photonic applications, J. Photochem. Photobiol., C. 5 (2004) 183.

[36] L. D. Carlos, R. A. S. Ferreira, V. d. Z. Bermudez and S. J. L. Ribeiro, Lanthanide-containing light-emitting organic–inorganic hybrids: A bet on the future, Adv. Mater. 21 (2009) 509.

[37] C. Piguet, J.-C. G. Bu1nzli, G. Bernardinelli, G. Hopfgartner, S. Petoud and O. Schaad, Lanthanide podates with predetermined structural and photophysical properties: Strongly luminescent self-assembled heterodinuclear d-f complexes with a segmental ligand containing heterocyclic imines and carboxamide binding units, J. Am. Chem. Soc. 118 (1996) 6681.

[38] I. V. Shelaev, F. E. Gostev, V. A. Nadtochenko, A. Y. Shkuropatov, A. A. Zabelin, M. D. Mamedov, A. Y. Semenov, O. M. Sarkisov and V. A. Shuvalov. Primary light-energy conversion in tetrameric chlorophyll structure of photosystem II and bacterial reaction centers: II. Femto- and picosecond charge separation in PSII D1/D2/Cyt b559 complex. *Photosynth. Res.*, 98 (2008) 95–103.

[39] O.S. Oluwafemi, N. Revaprasadu, O.O. Adeyemi, A new synthesis of hexadecylamine-capped Mn-doped wurtzite CdSe nanoparticles, Materials Letters. 64 (2010) 1513–1516.

[40] W.E. Mahmoud, H.M. El-Mallah, Synthesis and characterization of PVP-capped CdSe nanoparticles embedded in PVA matrix for photovoltaic application, Journal of Physics D: Applied Physics. 42 (2009) 035502.

[41] P.T.K. Chin, J.W. Stouwdam, R.A.J. Janssen, Highly luminescent ultranarrow Mn doped ZnSe nanowires, Nano Letters. 9 (2009) 745–750.

[42] J. Archana, M. Navaneethan, Y. Hayakawa, S. Ponnusamy, C. Muthamizhchelvan, Effects of multiple organic ligands on size uniformity and optical properties of ZnSe quantum dots, Materials Research Bulletin. 47 (2012) 1892–1897.

[43] J. Han, H. Zhang, Y. Tang, Y. Li, X. Yao, B. Yang, Role of redox reaction and electrostatics In transition-metal impurity-promoted photoluminescence evolution of water-soluble ZnSe nanocrystals, Journal of Physical Chemistry C. 113 (2009) 7503–7510.

[44] J. Zhuang, X. Zhang, G. Wang, D. Li, W. Yang, T. Li, Synthesis of water-soluble ZnS : Mn^{2+} nanocrystals by using mercaptopropionic acid as stabilizer, Journal of Materials Chemistry. 13 (2003) 1853.

[45] Z. Quan, D. Yang, C. Li, D. Kong, P. Yang, Z. Cheng, J. Lin, Multicolor tuning of manganese-doped ZnS colloidal nanocrystals, Langmuir. 25 (2009) 10259–10262.

[46] W. Chen, R. Sammynaiken, Y. Huang, J.O. Malm, R. Wallenberg, J.O. Bovin, V. Zwiller, N.A. Kotov, Crystal field, phonon coupling and emission shift of Mn^{2+} in ZnS:Mn nanoparticles, Journal of Applied Physics. 89 (2001) 1120–1129.

[47] J.F. Suyver, T. Van Der Beek, S.F. Wuister, J.J. Kelly, A. Meijerink, Luminescence of nanocrystalline ZnSe:Cu, Applied Physics Letters. 79 (2001) 4222–4224.

[48] G.B. Stringfellow, R.H. Bube, Radiative pair transitions in p-type ZnSe: Cu crystals, Journal of Applied Physics. 39 (1968) 3657.

[49] V. I. Klimov, Optical Nonlinearities and Ultrafast Carrier Dynamics in Semiconductor Nanocrystals. J. Phys. Chem. B, 104 (2000) 6112–6123.

[50] Shelaev, I.V., Gostev, F.E., Nadtochenko, V.A., Shkuropatov, A.Y., Zabelin, A.A., Mamedov, M.D., Semenov, A.Y., Sarkisov, O.M. and Shuvalov, V.A., 2008. Primary light-energy conversion in tetrameric chlorophyll structure of photosystem II and bacterial reaction centers: II. Femto-and picosecond charge separation in PSII D1/D2/Cyt b559 complex. Photosynthesis Research, 98 (1-3) 95.

[51] Nadtochenko, V., Denisov, N., Aybush, A., Gostev, F., Shelaev, I., Titov, A., Umanskiy, S., Ultrafast spectroscopy of fano-like resonance between optical phonon and excitons in CdSe quantum dots: Dependence of coherent vibrational wave-packet dynamics on pump fluence. Nanomaterials, 7 (2017) 371.

Chapter 8

Summary and future Prospects

The research topic of the present thesis entitled "*Growth and investigation of group II-VI semiconductor nanoparticles for luminescence based applications*" disclosed the structural, morphological, compositional and optical properties of ZnSe and Mn@ZnSe QDs and discussed their utility for sensing applications. In the present thesis, pure and doped ZnSe QDs have been synthesized by adopting the direct aqueous synthesis method, and successful doping is achieved with a nucleation doping strategy. Earlier, organic dyes, fluorescent proteins, or lanthanide chelates were mainly used as a staining agent for sensing applications, but they included several limitations such as broad-spectrum, poor photochemical stability less fluorescence intensity. On the other hand, QDs based sensors have several features like high sensitivity, unique tunable wide range optical properties, longer photoluminescence (PL) lifetime and are also useful for bio-sensing and bio-imaging. The QDs PL spectra mainly depend on the particle size and their surface charge or ligands attached to QDs surfaces. The structural and optical properties of ZnSe and Mn@ZnSe QDs are extensively studied using X-ray diffraction, absorption, photoluminescence and time-resolved photoluminescence spectroscopy along with sensing applications. **Based on the extensive study, the outcome of the research work has been organized into eight chapters and the chapter wise summary of the same is as follows:**

Chapter 1 consists of a brief introduction on nanoparticles, motivation for the research work on quantum dots, synthesis of quantum dots and their applications. Afterward, the types of nanomaterials and important characteristics of nanomaterials have been deliberated in detail. This chapter is mainly focused on the motivation of current

research work. Furthermore, the importance of QDs, especially group II-VI zinc-based semiconductor QDs has been discussed in detail. Subsequently, the chapter focuses on the luminescence-based sensing applications of un-doped and doped ZnSe QDs. The motivation to carry out the present research work, the objectives and the outline of the current research work are stated at the end of the chapter.

Chapter 2 deals with the experimental tools and techniques, mainly methodology, to accomplish the proposed objectives of the thesis. For the structural and surface morphology analysis, essential tools such as X-ray diffraction (XRD) and scanning electron microscopy (SEM) as well as transmission electron microscopy (TEM) were used for investigation. Energy-dispersive X-ray analysis (EDX) measurement has been carried out for elemental identification present in prepared QDs. The other main characterization techniques used are Fourier transform infrared (FTIR) spectroscopy, Ultrafast transient absorption, UV-visible & photoluminescence (PL) spectroscopy and time-resolved photoluminescence (TRPL) spectroscopy. The PL and TRPL studies were also carried out at a low temperature of 77 K.

Chapter 3 presents the synthesis of manganese doped zinc selenide (Mn@ZnSe) quantum dots (QDs) directly through an aqueous route. The X-ray diffraction pattern reveals the confined (4-5 nm) and crystalline cubic zinc blende structure of QDs. With Mn^{2+} doping, a new high-intensity orange photoluminescence (PL) band centered at around 580 nm was obtained owing to $^4T_1 \rightarrow {}^6A_1$ of Mn^{2+} ion transitions (for orange QLEDs). The freshly prepared water-dispersible QDs were treated under UV radiation for the photoactivation process, which enhanced the PL quantum efficiency from 5 to 17%. The response of QDs towards different metals was recorded in terms of absorption, PL and PL-lifetime. Among the numerous metals, Pb^{2+} shows strong PL quenching and the corresponding Stern-Volmer plot showed linearity with the detection

limits of 29.8×10^{-6} M in ultrapure water. The developed Mn@ZnSe QDs could act as a non-toxic sensor to sense hazardous lead in drinking water. The part of the work has been published in ***Materials Research Bulletin 134 (2021) 111121.***

Chapter 4 deals with blue fluorescent zinc selenide quantum dots (ZnSe QDs) synthesis using 3-mercaptopropionic acid through a direct aqueous route at a lower temperature of 70 ℃. The photoluminescence (PL) characteristics of ZnSe QDs has been employed to recognize nitroaromatic compounds, i.e., traces of 2,4,6-TNP (picric acid) in water. The sensing of nitroaromatic compounds was performed via fluorescence techniques. The PL band of ZnSe QDs observed at 490 nm is selectively quenched with an increasing concentration of picric acid in DI water and river water. For the proposed sensing probe, the Stern-Volmer (S-V) plot shows linearity over the range of 2.0 μM - 0.25 mM with the detection limit of 12.4×10^{-6} M without any interference effect of other nitroaromatic compounds. The plausible mechanism of PL quenching is considered as the inner filter effect, based on absorption, PL and PL lifetimes. Part of the work has been published in ***Spectrochimica Acta Part A: Molecular and Biomolecular Spectroscopy 260 (2021) 119937.***

Chapter 5 deals with water-dispersible, stable and fluorescent Mn^{2+} doped zinc selenide (ZnSe) quantum dots (QDs) which were applied for sensing highly toxic and hazardous mercury (Hg^{2+}) and lead (Pb^{2+}) ions in water. The synthesized QDs were protected with 3-marcaptoproponic acid (MPA) ligand. The MPA ligand was selected as a high acceptor for metals due to the strong interaction between the metal ions and the thiol group (-SH). The photoluminescence (PL) intensity of MPA-protected Mn^{2+} doped ZnSe QDs was strongly quenched with Hg^{2+} and Pb^{2+} and unaffected with other metals. The corresponding Stern-Volmer plots of as-synthesized QDs showed linearity over a wide range (0-100 μL). The average PL lifetime of Mn^{2+}@ZnSe was shortened

with Hg^{2+} concentration whereas increased with Pb^{2+} concentration. The proposed system provided a new possibility for dual response ions detection in real samples due to its simplicity, low cost, high stability and sensitivity. A filter paper-based sensor was also prepared and successfully tested for sensing via colorimetric and fluorometric detection methods. Part of the research work is under review in ***Chemical Physics Letters 787 (2022) 139270.***

Chapter 6 deals with un-doped and Mn^{2+} doped zinc selenide (ZnSe) quantum dots (QDs), which were investigated through photoluminescence (PL) and photoluminescence excitation (PLE) spectroscopy in the temperature range from 300 to 77 K. Strong blue and orange PL were observed for ZnSe and Mn@ZnSe QDs, respectively. The intensity of PL spectra is found to be exceedingly dependent on temperature, observed the highest PL intensity at 77 K. To understand the origin and mechanism of the temperature-dependent shift in PL, the PL spectra with different excitations and PLE spectra at different PL wavelengths were recorded at decreasing temperature (300 - 77 K) and vis-a-vis. The calculated activation energy values come out to be 42.2 meV and 66.4 meV for ZnSe and Mn@ZnSe QDs, respectively. The lifetimes of Mn@ZnSe QDs were discussed at different temperatures. The absolute sensitivity (S) for the temperature sensor is calculated and the maximum S values come out to be 0.58% at 225 K and 0.44% K^{-1} at 250 K for ZnSe and Mn@ZnSe QDs, respectively. The wide range of linearly temperature-dependent PL suggests that the prepared QDs can be cast for a PL-intensity-based optical temperature sensor. Part of the research work has been published in, ***Materials Chemistry and Physics 276 (2022) 125349***.

Chapter 7 contains a wide range of light-emitting water-dispersible metal-doped (Mn@ZnSe and Cu@ZnSe) and co-doped (Cu&Mn@ZnSe) zinc-selenide

(ZnSe) quantum dots (QDs) that were produced below 75° C in an aqueous medium. XRD manifests a cubic crystal structure of quantum dots despite the low temperature of the synthesis. A distinctive feature of the obtained quantum dots is the high concentration of trap states. There are three leading emissions in the wavelength range of 300 - 700 nm, produced from distinct emitting states assigned to ZnSe, Cu^{2+}, Mn^{2+} and trap transitions. The lower energy states, which emit between 500-700 nm with long lifetimes, are populated following excitation energy transfer from ZnSe exciton state to traps and metal ions. The surface and deep trap states of ZnSe are contributing to the overall PL, investigated using time-resolved fluorescence and femtosecond (fs) pump-probe techniques. The fs-picoseconds dynamics of the exciton bleaching band predicted that excitation energy transfer could occur from trap states and the exciton state. The excited-state absorption appeared in transient absorption spectra attributed to the trap states absorption and probably the bi-exciton absorption. Thus, the produced water-dispersible QDs can act as single component white-light-emitting devices, e.g., quantum dots light-emitting devices (QLEDs), as for biological applications. The part of the research work is communicated for publication.

Chapter 8 consists of the summary and the major findings of the thesis obtained in the present research work. This chapter also includes an outline of the future scope of this investigation.

Considering the above facts, the following points may be explored in the future:

- The environmental friendly QDs may be produced using green synthesis routes.
- To increase the QY and decrease the FWHM of QDs for commercial uses.
- From results of the optical and structural studies reported in the present thesis, it is clear that the II-VI QDs have interesting optical and electronics properties therefore it

requires further research to understand the mechanism of II-VI CdSe QDs. Further, the shifting of fluorescence peak can be used in photonic applications for tuning purposes.

- Hot injection synthesized QDs has better optical and electronics properties, good stability, highly monodispersiblity and bio compatibility hence can be used in future for imagine and biosensor.
- The concept of using various nanomaterials and their nanocomposites can be used for the development of highly sensitive devices for early diagnosis and point-of-care applications.
- The QDs based bio sensor and biomarker has fascinating future because of their high sensitivity and suitable particle size.